

Quantum mechanically guided design of mechanical properties and topology of metallic glasses

Von der Fakultät für Georessourcen und Materialtechnik der
Rheinisch-Westfälischen Technischen Hochschule Aachen

zur Erlangung des akademischen Grades eines

Doktors der Ingenieurwissenschaften

genehmigte Dissertation

vorgelegt von

Herrn Simon Evertz, M.Sc. RWTH

aus Stolberg (Rheinl.)

Berichter: Herr Univ.-Prof. Jochen M. Schneider, Ph. D.
Herr Prof. Dr. Gerhard Dehm

Tag der mündlichen Prüfung: 25.11.2020

Diese Dissertation ist auf den Internetseiten der Universitätsbibliothek verfügbar.

Abstract

Metallic glasses are promising structural materials due to their unique property combinations such as high fracture toughness and high strength. For structural applications and processing, the coefficient of thermal expansion is an important design parameter. Here, it is demonstrated that predictions of the coefficient of thermal expansion for metallic glasses by density functional theory based *ab initio* calculations are efficient both with respect to time and resources. The coefficient of thermal expansion is predicted by an *ab initio* based method utilising the Debye-Grüneisen model for a Pd-based metallic glass, which exhibits a pronounced medium range order. The predicted coefficient of thermal expansion of $3.4 \cdot 10^{-5} \text{ K}^{-1}$ at room temperature is critically appraised by *in situ* synchrotron X-ray diffraction and excellent agreement is observed. Through this combined theoretical and experimental research strategy, the feasibility to predict the coefficient of thermal expansion from the ground state structure of a metallic glass until the onset of structural changes is shown. This strategy provides a method to efficiently probe a potentially vast number of metallic glass alloying combinations regarding thermal expansion.

For the application of metallic glasses as structural materials, high fracture toughness is crucial to avoid catastrophic failure of the material in a brittle manner. One fingerprint for fracture toughness in metallic glasses is the fraction of hybridized bonds, which is affected by alloying $\text{Pd}_{57.4}\text{Al}_{23.5}\text{Y}_{7.8}\text{M}_{11.3}$ with $\text{M} = \text{Fe}, \text{Ni}, \text{Co}, \text{Cu}, \text{Os}, \text{Ir}, \text{Pt}, \text{and Au}$. It is shown that experimental fracture toughness data is correlated to the fraction of hybridized bonds which scale with the localized bonds at the Fermi level. Thus, the localized bonds at the Fermi level are utilized quantitatively as a measure for fracture toughness. Based on *ab initio* calculations, the minimum fraction of hybridized bonds was identified for $\text{Pd}_{57.4}\text{Al}_{23.5}\text{Y}_{7.8}\text{Ni}_{11.3}$. According to the ansatz that the crystal orbital overlap population at the Fermi level scales with fracture toughness, for $\text{Pd}_{57.4}\text{Al}_{23.5}\text{Y}_{7.8}\text{Ni}_{11.3}$ a value of around $95 \pm 20 \text{ MPa} \cdot \text{m}^{0.5}$ is predicted quantitatively for the first time. Consistent with this prediction, in micro-mechanical beam bending experiments $\text{Pd}_{57.4}\text{Al}_{23.5}\text{Y}_{7.8}\text{Ni}_{11.3}$ thin films show pronounced plasticity and absence of crack growth.

As the properties of metallic glasses depend on the electronic structure, which in turn is defined by chemical composition, the influence of metalloids such as B on glass transition, topology, magnetism, and bonding is investigated systematically for B concentrations $x = 2$ to 92 at.% in the $(\text{Co}_{6.8 \pm 3.9}\text{Ta})_{100-x}\text{B}_x$ system. From an electronic structure and coordination point of view, the B concentration range is divided into three regions: Below 39 ± 5 at.% B, the material is a metallic glass due to the dominance of metallic bonds. Above 69 ± 6 at.%, the presence of an icosahedra-like B network is observed. As the B concentration is increased above 39 ± 5 at.%, the B network evolves while the metallic coordination of the material decreases until the B concentration of 69 ± 9 at.% is reached. Hence, a composite is formed. It is evident that, based on the B concentration, the ratio of metallic bonding to icosahedral bonding in the composite can be controlled. It is proposed that, by tuning the coordination in the composite region, glassy materials with defined plasticity and processability can be designed.

While it is accepted that the plastic behaviour of metallic glasses is affected by their free volume content, the effect thereof on chemical bonding has not been investigated systematically. According to electronic structure analysis, the overall bond strength is not significantly affected by the free volume content. However, with increasing free volume content, the average coordination number decreases. Furthermore, the volume fraction of regions containing atoms with lower coordination number increases. As the local bonding character changes from bonding to anti-bonding with decreasing coordination number, bonding is weakened in the volume fraction of lower coordination number. During deformation, the number of strong, short-distance bonds decreases more for free volume containing samples than for samples without free volume, resulting in additional bond weakening. Thus, it is shown that the introduction of free volume causes the formation of volume fractions of lower coordination number resulting in weaker bonding and proposed that this is the electronic structure origin of the enhanced plastic behaviour reported for glasses containing free volume.

Zusammenfassung

Metallische Gläser besitzen vielversprechende mechanische Eigenschaftskombinationen für Strukturanwendungen, wie die Kombination von hoher Bruchzähigkeit und Festigkeit. Der thermische Ausdehnungskoeffizient ist dabei ein wichtiger Design-Parameter für Strukturanwendungen sowie die Verarbeitung metallischer Gläser. In dieser Arbeit wird gezeigt, dass die Vorhersage des thermischen Ausdehnungskoeffizienten durch auf der Dichte-Funktionaltheorie beruhender *ab initio* Berechnung effizient in Bezug auf Zeit und Ressourcen ist. Der thermische Ausdehnungskoeffizient wird für ein Pd-basiertes metallisches Glas mit einer *ab initio* Methodik unter Anwendung des Debye-Grüneisenmodells vorhergesagt. Dieses Pd-basierte metallische Glas besitzt eine ausgeprägte mittelreichweitige Ordnung. Der vorhergesagte thermische Ausdehnungskoeffizient von $3.4 \cdot 10^{-5} \text{ K}^{-1}$ bei Raumtemperatur wird durch *in situ* Röntgenbeugungsversuche mit Synchrotronstrahlung kritisch hinterfragt. Dabei wird eine exzellente Übereinstimmung der theoretischen und experimentellen Werte beobachtet. Diese kombinierte theoretische und experimentelle Forschungsstrategie zeigt die Möglichkeit der Vorhersage des thermischen Ausdehnungskoeffizienten ausgehend von einem Topologiemodell im Grundzustand, sofern topologische Änderungen während des Aufheizens ausbleiben. Mit dieser Methodik kann die große Zahl an möglichen Legierungskombinationen metallischer Gläser effizient in Bezug auf den thermischen Ausdehnungskoeffizienten getestet werden.

Für Strukturanwendungen metallischer Gläser ist die Bruchzähigkeit von besonderer Bedeutung, um katastrophales Versagen durch Sprödbruch zu verhindern. Die Anzahl der hybridisierten Bindungen in einem metallischen Glas ist ein Fingerabdruck für die Bruchzähigkeit, der durch das Legieren von $\text{Pd}_{57.4}\text{Al}_{23.5}\text{Y}_{7.8}\text{M}_{11.3}$ mit $\text{M} = \text{Fe}, \text{Ni}, \text{Co}, \text{Cu}, \text{Os}, \text{Ir}, \text{Pt}, \text{and Au}$ beeinflusst wird. Es wird gezeigt, dass experimentelle Bruchzähigkeiten mit dem Anteil der hybridisierten Bindungen korrelieren. Der Anteil hybridisierter Bindungen skaliert dabei mit den lokalisierten Bindungen am Fermi-Niveau. Diese lokalisierten Bindungen am Fermi-Niveau werden daher als quantitatives Maß für die Bruchzähigkeit genutzt. Basierend auf *ab initio* Berechnungen wird für $\text{Pd}_{57.4}\text{Al}_{23.5}\text{Y}_{7.8}\text{Ni}_{11.3}$ ein

minimaler Anteil hybridisierter Bindungen festgestellt. Gemäß dem Ansatz, dass die Bruchzähigkeit mit der Kristallorbital-Überlappungspopulation am Fermi-Niveau skaliert, wird eine Bruchzähigkeit in Höhe von $95 \pm 20 \text{ MPa} \cdot \text{m}^{0.5}$ für $\text{Pd}_{57.4}\text{Al}_{23.5}\text{Y}_{7.8}\text{Ni}_{11.3}$ vorhergesagt. Mikromechanische Bruchversuche am Biegebalken sind konsistent mit dieser Vorhersage, da in den Biegebalken ausgeprägte plastische Verformung und kein Risswachstum sichtbar wird.

Da die Eigenschaften metallischer Gläser von der Elektronenstruktur abhängen, die wiederum von der chemischen Zusammensetzung definiert wird, wird hier der Einfluss von Halbmetallen wie Bor auf den Glasübergang, Topologie, Magnetismus und Bindungen systematisch für Borkonzentrationen $x = 2$ bis 92 at.% im $(\text{Co}_{6.8 \pm 3.9}\text{Ta})_{100-x}\text{B}_x$ -System untersucht. Vom Standpunkt der Elektronenstruktur und Koordination lässt sich der Borkonzentrationsbereich in drei Regionen aufteilen: Unterhalb von 39 ± 5 at.% Bor ist das Material ein metallisches Glas auf Grund der dominierenden metallischen Bindungen. Oberhalb von 69 ± 6 at.% wird ein ikosaeder-ähnliches Bornetzwerk beobachtet. Wenn die Borkonzentration über 39 ± 5 at.% Bor erhöht wird, entwickelt sich ein Bor-Netzwerk, während die metallische Koordination im Material bis zu einer Borkonzentration von 67 ± 5 at.% abnimmt. Daher wird in diesem mittleren Borkonzentrationsbereich ein Komposit gebildet. Es ist erwiesen, dass durch die Borkonzentration das Verhältnis von metallischen zu ikosaedrischen Bindungen kontrolliert werden kann. Es wird daher vermutet, dass durch Einstellung der Koordination in der Kompositregion Gläser mit definierter Plastizität und Verarbeitbarkeit designt werden können.

Es ist in der Literatur bekannt, dass die plastische Verformung metallischer Gläser vom Gehalt des freien Volumens beeinflusst wird. Allerdings wurde der Effekt des freien Volumens auf die chemischen Bindungen bis jetzt nicht systematisch untersucht. Mit Hilfe einer Analyse der Elektronenstruktur wird gezeigt, dass die globale Bindungsstärke nicht signifikant beeinflusst wird. Allerdings sinkt die durchschnittliche Koordinationszahl mit steigendem Gehalt des freien Volumens. Der lokale Bindungscharakter ändert sich dabei von bindend zu anti-bindend mit abnehmender Koordinationszahl. Während plastischer Verformung sinkt die Anzahl der starken, bindenden Bindungen stärker für Gläser mit freiem Volumen als für Gläser ohne freies

Volumen. Dadurch werden die Bindungen weiter geschwächt. Es wird gezeigt, dass das Einbringen von freiem Volumen zur Bildung von Volumenanteilen mit niedrigerer Koordinationszahl führt. Dies resultiert in schwächeren Bindungen und wird als elektronenstruktur-basierter Grund für die verbesserte plastische Verformbarkeit von Gläsern, die freies Volumen enthalten, vorgeschlagen.

Preface

Financial support for this work by Deutsche Forschungsgemeinschaft within the SPP 1594 “Quantum mechanically guided design of ultra strong glasses” is gratefully acknowledged. *Ab initio* calculations were performed on the JARA-HPC partition part of the supercomputer CLAIX at RWTH Aachen University within project JARA0131. Parts of this research were carried out at beamline P02.1 of the light source PETRA III at DESY, a member of the Helmholtz Association (HGF).

This thesis includes the following papers:

Paper I

Thermal expansion of Pd-based metallic glasses by *ab initio* methods and high energy X-ray diffraction

S. Evertz, D. Music, V. Schnabel, J. Bednarcik and J. M. Schneider
Scientific Reports **7**, 15744 (2017), doi:10.1038/s41598-017-16117-7

Paper II

Electronic structure based design of thin film metallic glasses with superior fracture toughness

S. Evertz, I. Kirchlechner, R. Soler, C. Kirchlechner, P. Kontis, J. Bednarcik, B. Gault, G. Dehm, D. Raabe and J. M. Schneider

Materials and Design **186**, 108327 (2020), doi: 10.1016/j.matdes.2019.108327

Paper III

Boron concentration induced Co-Ta-B composite formation observed in the transition from metallic to covalent glasses

S. Evertz, S. Prünke, L. Patterer, A. Marshal, D. M. Holzapfel, A. Schökel, M. Hans, D. Primetzhofer and J. M. Schneider

Condensed Matter **5(1)**, 18 (2020), doi: 10.3390/condmat5010018

Paper IV

Effect of the free volume on the electronic structure of Cu₇₀Zr₃₀ metallic glasses

S. Evertz and J. M. Schneider

Materials **13(21)**, 4911 (2020), doi: 10.3390/ma13214911

Publications related to the topic of this thesis:

Paper V

Review on quantum mechanically guided design of ultra-strong metallic glasses

S. Evertz, V. Schnabel, M. Köhler, I. Kirchlechner, P. Kontis, Y.-T. Chen, R. Soler, B. N.

Jaya, C. Kirchlechner, D. Music, B. Gault, J. M. Schneider, D. Raabe and G. Dehm

Frontiers in Materials **7** (2020), 89

Paper VI

Nano-laminated thin film metallic glass design for outstanding mechanical properties

P. Kontis, M. Köhler, **S. Evertz**, Y.-T. Chen, V. Schnabel, R. Soler, J. Bednarcik, C.

Kirchlechner, G. Dehm, D. Raabe, J. M. Schneider and B. Gault

Scripta Materialia **155**, 73-77 (2018)

Other publications:

Paper VII

Effect of synthesis temperature on the phase formation of NiTiAlFeCr compositionally complex alloy thin films

A. Marshal, P. Singh, D. Music, S. Wolff-Goodrich, **S. Evertz**, A. Schökel, D.D. Johnson,

G. Dehm, C.H. Liebscher and J.M. Schneider

Journal of Alloys and Compounds **835**, 155178 (2020)

Paper VIII

Spinodal decomposition of reactively sputtered $(V_{0.64}Al_{0.36})_{0.49}N_{0.51}$ VAIN thin films

M. Hans, H. Rueß, Z. Czigány, J. Krause, P. Ondračka, D. Music, **S. Evertz**, D. M. Holzapfel,

D. Primetzhofer and J. M. Schneider

Surface & Coatings Technology **389**, 125641 (2020)

Paper IX

Stress-Dependent Elasticity of TiAlN Coatings

M. Hans, L. Patterer, D. Music, D. M. Holzapfel, **S. Evertz**, V. Schnabel, B. Stelzer,

D. Primetzhofer, B. Völker, B. Widrig, A. O. Eriksson, J. Ramm, M. Arndt, H. Rudigier and

J. M. Schneider

Coatings **9(1)**, 24 (2019)

Paper X

Unprecedented thermal stability of inherently metastable titanium aluminium nitride by point defect engineering

M. to Baben, M. Hans, D. Primetzhofer, **S. Evertz**, H. Rueß and J. M. Schneider

Materials Research Letters **5(3)**, 158-169 (2017)

Paper XI

Revealing the relationships between chemistry, topology and stiffness of ultrastrong Co-based metallic glass thin films: A combinatorial approach

V. Schnabel, M. Köhler, **S. Evertz**, J. Gamcova, J. Bednarcik, D. Music, D. Raabe and

J. M. Schneider

Acta Materialia **107**, 213-219 (2016)

Paper XII

Stiffness and toughness prediction of Co-Fe-Ta-B metallic glasses, alloyed with Y, Zr, Nb, Mo, Hf, W, C, N and O by *ab initio* molecular dynamics

V. Schnabel, **S. Evertz**, H. Rueß, D. Music and J. M. Schneider

Journal of Physics: Condensed Matter **27**, 105502 (2015)

Contributions to the papers:

The research questions as well as the theoretical and experimental research strategies were conceived with JMS. All first drafts of the manuscripts were iterated with JMS. All co-authors contributed to evaluation and discussion of the results and revised the manuscripts.

Paper I: The *ab initio* calculations were carried out and analysed by SE with support of DM. SE synthesised the samples. The high energy X-ray scattering experiments were carried out by SE with support of VS and JB. SE analysed the experimental data.

Paper II: SE performed and analysed the *ab initio* measurements. Samples were synthesised by SE. The high energy X-ray scattering experiments were conducted and analysed by SE with support of JB. Micro-mechanical bending experiments were performed by IK, RS, CK and GD. Atom probe tomography was conducted by PK, BG and DR.

Paper III: SE carried out the *ab initio* calculations and analysed the data. The samples were synthesised by SE. High energy X-ray scattering experiments were performed by SE with support of LP, DMH and AS. SE analysed the scattering data. XPS data was collected by SP and LP and analysed by SE with support of SP and LP. Magnetometry measurements were carried out by AM. ERDA measurements were conducted by MH and DP.

Paper IV: SE performed the *ab initio* calculations and analysed the data.

Acknowledgements

First, I want to thank Prof. Jochen M. Schneider for the opportunity to work on my PhD thesis at Materials Chemistry. Your open-minded, honest, collaborative and supportive discussion culture I appreciated very much – already in my time as a student assistant at MCh. I am grateful for the freedom and support I experienced while diving into the world of metallic glasses and hitting the frontiers of both theoretical and experimental methods.

Large parts of this work were only possible due to the great working atmosphere at MCh, caused by the openness and support of all colleagues. To be not send away in case of spontaneous problems as well as the practical and mental support in times where the road seems blocked helped me to accept the challenges and to discover the positive side of the blocked road. I enjoyed also the collaboration with the non-scientific staff in the administration and the workshops for clearing the road of bureaucratic hurdles and giving technical (emergency) assistance that used to be better than the original idea I had in my mind. Being one team is the secret of the special working atmosphere at MCh.

Keeping the work-life-balance in mind, I want to thank my friends who were always there for activities completely unrelated to materials to get a proper distance to science after working hours, enabling to start the next day with a fresh view on the challenges ahead.

Not to forget, I thank my family, Ferdinand and Gerlinde and my brother Andreas for their love, time and ears at any time and their endeavour to understand why materials are so interesting. Having someone who is supportive and listening in any situation is invaluable to keep confidence and vitality.

Table of contents

Abstract.....	I
Zusammenfassung.....	III
Preface.....	VI
Acknowledgements	X
Table of contents.....	XI
1. Introduction	- 1 -
1.1. Metallic glasses: The glassy state	- 1 -
1.2. Mechanical properties of metallic glasses	- 4 -
1.2.1. Plastic deformation of metallic glasses.....	- 5 -
1.2.2. Toughness of metallic glasses	- 8 -
1.3. Quantum mechanical prediction of metallic glass properties	- 11 -
1.4. Nano-structured glasses	- 14 -
1.5. Research questions.....	- 16 -
2. Methods	- 18 -
2.1. <i>Ab initio</i> calculations.....	- 18 -
2.2. Bonding analysis	- 22 -
2.3. Magnetron sputtering	- 24 -
2.4. Energy dispersive X-ray spectroscopy.....	- 28 -
2.5. High energy X-ray scattering	- 30 -
2.6. X-ray photoelectron spectroscopy	- 31 -
2.7. Micromechanical beam bending tests.....	- 32 -
2.8. Magnetometry	- 35 -
2.9. Atom probe tomography.....	- 35 -

3. Summary of publications	- 36 -
4. Contribution to the field.....	- 38 -
5. Future work	- 39 -
References.....	- 42 -
Paper I	- 59 -
Paper II	- 70 -
Paper III	- 80 -
Paper IV	- 94 -

1. Introduction

On 3rd September 1960, “an amorphous structure [...] in a 25 atomic per cent silicon-gold alloy which was quenched from ~1,300°C to room temperature” [1] was reported in Nature by W. Klement jun., R. H. Willens and P. Duwez from the Californian Institute of Technology. This $\text{Au}_{75}\text{Si}_{25}$ alloy, though crystallising into metastable crystalline phases within 24 hours [1], is since known as the first metallic glass.

During the past 60 years of research on metallic glasses, amorphous alloys have been reported to be promising in terms of anti-microbial [2–9], tribological [9–11], catalytic [12–16] and mechanical [17–30] properties. Despite the wide range of interesting functional applications, the focus of this work will be on the quantum mechanically guided design of mechanical properties and topology of metallic glasses due to the property combination of high fracture toughness and yield strength [31], which is promising for structural applications. To approach the world of metallic glasses, the following sections give an overview on the characteristics of metallic glasses, on their mechanical properties, on the current state of quantum mechanical property predictions and on nano-structured metallic glasses to reach the research questions addressed in this work.

1.1. Metallic glasses: The glassy state

Metallic glasses are amorphous alloys [17]. According to traditional metallurgy, they are defined by the glass production route of rapid quenching below the glass transition temperature T_g (Fig. 1), where kinetic limitations prevent crystallization [18,20,32]. Short: “A [metallic] glass is a solid obtained by freezing a liquid without crystallization” [33]. This definition excludes glasses obtained by other synthesis routes such as magnetron sputtering, which are included in the definition based on topology: “Glass is a non-crystalline solid” [33]. While this definition also includes non-crystalline solids that are not glasses, the definition of metallic glass used in this work is: “A metallic glass is a non-crystalline solid exhibiting the phenomenon of glass transition” [33].

To form a metallic glass, the liquid-like structure of a material needs to be stabilized, i.e. crystallization must be prevented. Inoue formulated hence three empirical glass forming rules for bulk metallic glasses: Typically, a metallic glass contains more than three constituents; the difference of atomic radii is larger than 12 %; and the heats of mixing between the constituents are negative [34]. Nowadays, minor alloying with elements that have a positive heat of mixing with at least one constituent of the metallic glass – violating Inoue’s 3rd rule – has been shown to improve glass-forming ability and plasticity of metallic glasses [35]. On the other side, a positive heat of mixing between two constituents can also result in phase separation [36]. Synthesis methods that enable metastable phase formation such as physical vapour deposition exhibit cooling rates up to the factor 10^5 to 10^{11} larger than metallurgical synthesis routes [37]. Therefore, the composition space fraction of thin film metallic glasses is significantly expanded compared to bulk metallic glasses [37]. This expansion cannot be predicted based on Inoue’s glass-forming rules. Hence, guidance to identify compositions with promising properties in this composition space fraction would be extremely valuable. This work concentrates on the quantum mechanical design of mechanical properties and topology as both are based on the inherent chemical bonding of the material.

The glass transition – mentioned in the definition of a metallic glass above – is not a thermodynamic phase transition [22,33]. Hence, no heat of solidification is removed from the material when solidifying into a glass (Fig. 1) [38]. The atomic motion becomes impeded, resulting in a sudden increase in relaxation time necessary to reach an equilibrium configuration [33]. This is macroscopically observed as reaching a viscosity of 10^{13} dPa·s [33]. Thereby, the glass configuration occupies a local minimum of the potential energy landscape in the configuration space, exhibiting higher energy than their crystalline counterparts and is hence metastable [33,39,40]. The glass transition temperature T_g depends on the cooling rate of the metallic glass (Fig. 1), whereby a higher cooling rate yields a higher T_g [33,38]. T_g is not only affected by the cooling rate and hence the synthesis conditions, but also by the thermal history of the glass, i.e. heat treatments, as well as by the chemical composition of the glass. Hence, T_g can be considered as a measure for the internal energy of the glass [38].

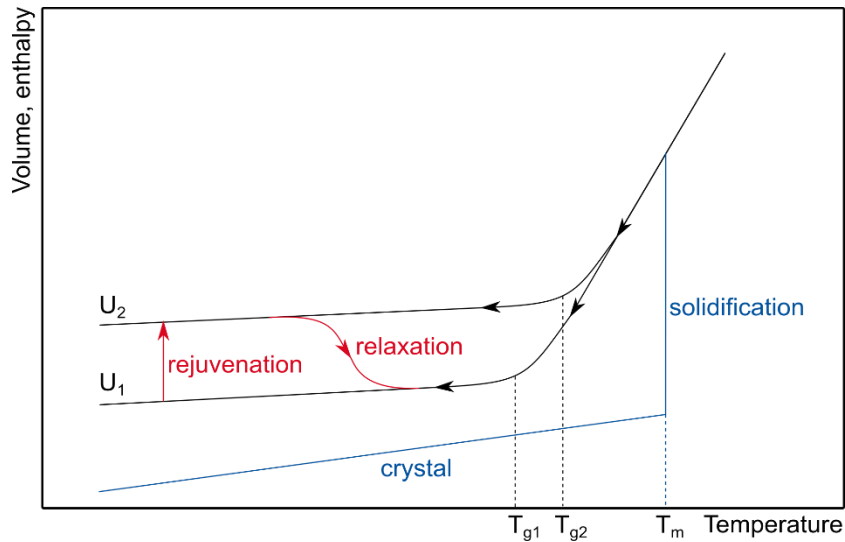


Fig. 1: Volume and enthalpy change during formation of a glass. T_m is the melting temperature, T_{g1} and T_{g2} are the glass transition temperatures of the glasses produced with cooling rates U_1 and U_2 ($U_1 < U_2$). As reference, the blue curve shows a crystalline material.

The figure is based on references [33,41–43].

The excess entropy of the glassy state compared to the crystalline state is commonly called the “configurational entropy S_c ” of a glass [44]. This entropy, designated as S_c in the following, quantifies the number of accessible (metastable) configurations of the glass [44] and is thus dependent on the cooling rate: quickly cooled glasses have less time to sample the potential energy space and exhibit hence a higher S_c than slowly cooled glasses [33]. Thus, when comparing two glasses, S_c is inversely correlated to T_g [45]. S_c of the glassy state remains at a constant value that is close to the S_c observed at T_g . Thus, the entropy of a glass is hence not equal to zero at 0 K [33].

As all amorphous materials, monolithic metallic glasses lack long-range order and microstructural features such as grain boundaries [17]. However, metallic glasses have a strong short-range order, because stable local atomic configurations with strong chemical affinity achieve a high packing density [46]. The short-range order configurations, while locally not identical everywhere in the glass, are characteristic for a certain metallic glass [46] and determine its properties. Both short-range order and properties are caused by the chemical

bonding in the glass. Within the zoo of coordination polyhedra, icosahedra are the most prominent polyhedra as they stabilize the amorphous structure by impeding crystallization [46].

Since they are metastable materials, metallic glasses tend to change their state to one with lower energy when heated to sufficient temperatures below T_g (Fig. 1), approaching a configuration of lower energy without crystallization [33]. This is known as structural relaxation [41] and is an irreversible process [42]. Sufficient temperatures for structural relaxation can be as low as room temperature [1], but are typically annealing temperatures below T_g [42]. On the atomic scale, structural relaxation is the annihilation of free volume [42,47], resulting eventually in a densified metallic glass state. Structural relaxation affects the mechanical properties for a given glass state [41–43] and leads to embrittlement [42,48]. The opposite of structural relaxation is structural rejuvenation [43]. By annealing above T_g or mechanical treatments the free volume content and energy stored in the metallic glass is increased (Fig. 1) and therewith, the effects of structural relaxation on the properties of the glass are reversed [48]. This has been reported to allow a specific amount of work hardening in metallic glasses [43,49]. Due to structural relaxation, the service temperature of metallic glasses is limited to temperatures well below T_g [48].

1.2. Mechanical properties of metallic glasses

The mechanical properties of metallic glasses such as high hardness, yield strength, and toughness are often promising for structural applications [17]. Metallic glasses can exhibit high resilience together with low damping [17], allowing the efficient storage and release of elastic energy. In addition, metallic glasses cover a wide range of fracture toughness together with a high yield strength [17,31]. In contrast to crystalline materials, metallic glasses do not exhibit microstructure-based work-hardening and are therefore prone to plastic instabilities and early failure [50]. However, similar to crystalline materials, mechanical properties depend on the chemistry but also on sample dimensions and processing history [18,50] since the processing history influences the atomic configuration and especially the free volume content of the glass

[24,46,51]. For example, the fracture toughness, which is a crucial material parameter for any load-bearing structural material, is enhanced as the free volume content is increased [24].

This subchapter gives an overview on the mechanical properties of metallic glasses with a focus on plastic deformation and toughness since the underlying mechanisms for both are crucial to understand for the design of metallic glasses. In contrast to crystalline materials, where plastic deformation is sustained mainly by the rather well understood movement of dislocations [52], a single model for plastic deformation of metallic glasses does not yet exist. Thus, in this overview the two prevailing models for plastic deformation in metallic glasses – free volume and shear banding – will be summarized. In order to deeply understand the topological origins of free volume and shear banding, the reader is referred to the cited literature, as the focus of research in this work is the electronic structure origin of toughness and plastic deformation.

1.2.1. Plastic deformation of metallic glasses

Plasticity contributes to some extent to the toughness of metallic glasses (Fig. 2). Hence, the mechanisms that govern plasticity of metallic glasses, namely plastic deformation via regions of free volume as well as shear banding, will be shortly introduced. Free volume in metallic glasses are regions with locally lower coordination [53] and hence a locally larger atomic volume that can be understood as density fluctuations [24]. In these regions of lower coordination, the atoms can move in their nearest neighbour cage without energy change [54]. Thus, free volume provides a higher mobility of atoms and lowers the energy barrier for shear transformations [22,53] and promotes plastic deformation [51].

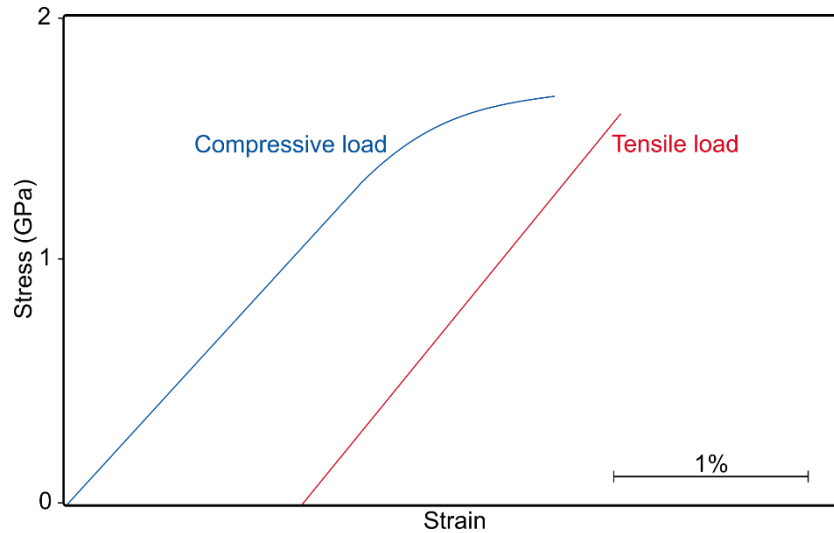


Fig. 2: Stress-strain curve of $Zr_{59}Cu_{20}Al_{10}Ni_8Ti_3$ metallic glasses under compressive and tensile load. Data from [55].

On the atomic scale, plastic deformation is borne by cooperative atomic motions which can be described as flow [56]. During plastic flow, on the one hand, free volume is annihilated within less than 10 atomic jumps [54,56,57], lowering the energy of the system [54]. On the other hand, by forcing atoms under shear stress into free volume sites smaller than their atomic volume, relaxation of the neighbouring atoms creates free volume and results in shear softening [54]. The equilibrium of annihilation and creation of free volume under shear stress results in steady state flow, called homogeneous deformation. Homogeneous deformation is observed at low stresses or high temperatures [54,58]. Pure homogeneous deformation can be observed in nanometre-scaled samples [58,59] that deform until failure by necking as reported by Guo and co-workers [58].

Deviation from the steady state flow will cause either free volume creation with time until a critical free volume content of 2.4 % [60] is reached, where yielding begins [60] or free volume localization, which eventually leads to the formation of shear bands and is accompanied by a drop in stress [22,53].

Shear bands concentrate the plastic deformation in thin bands [54] with 10 to 100 nm thickness [50,61] and contain groups of atoms with much larger atomic strain than the surrounding matrix [50]. This localisation of strain is autocatalytic if a critical shear band size is reached [50,61].

Deformation via shear bands is the normal mode of plastic deformation at room temperature, due to the mostly low homologous temperature and typically large stresses [50].

Shear bands nucleate from shear transformation zones (STZ), i.e. stress concentrations at local free volume sites of the size of 3 [62] to 250 atoms [61,63,64], and are able to propagate when reaching a critical size [50]. Homogeneous nucleation of shear bands out of structural fluctuations requires more energy than heterogeneous nucleation of a shear band at stress concentrators such as precipitates or surface defects [50,53,65]. Therefore, the strength of metallic glasses containing stress concentrators is determined by the flow stress [22] and lower than the strength of a perfect glass containing only the inherent structural heterogeneities of a glass [66]. The propagating shear band is not shearing continuously, but exhibits stick-slip behaviour and moves stepwise [61,67].

The propagation of one critical shear band can lead to failure of the material, which is mostly the case in tension due to work softening [50,68]. Therefore, metallic glasses show zero ductility despite exhibiting a large fracture toughness [22,50,67,69]. Thus, for structural applications, the propagation of single shear bands is undesired, and the formation of multiple, sub-critical shear bands is desired. One possibility to stop shear band propagation and promote multiple shear band formation is the stress state. These multiple shear bands can interact and enter a self-organized critical state that dissipates the shear offset over all participating shear bands and allows stable plastic deformation [70]. Multiple shear band formation is promoted by multiaxial or complex stress states [50], where secondary shear bands nucleate from primary shear bands in stable deformation geometries such as bending [67,71]. Multiple shear band formation is amplified by geometric constraints [72]. Shear bands can be arrested for example by the neutral axis under bending load [50,73]. Due to this plastic deformation via shear bands, metallic glasses appear brittle in tension and ductile in compression (Fig. 2) [55].

Plastic deformation of metallic glasses depends on the sample size, as for samples smaller than ~100 nm, shear band formation can be eventually entirely prevented as the volume

available for shear band nucleation sites [64] is too small for the shear bands to develop [50]. While the volume for shear band nucleation might be sufficient, it might still be insufficient for the shear bands to mature and therewith to shear catastrophically [58]. Small sample sizes promote the formation of multiple closely spaced not-mature shear bands, while thick samples tend to form few widely spaced shear bands with large shear offset in bending [74]. Hence, metallic glasses perform best in nano-scale applications under bending or compressive load [50,59,74,75].

1.2.2. Toughness of metallic glasses

As plastic deformation is not stable due to the absence of work hardening [22], metallic glasses are not ductile. On the other hand, metallic glasses are not entirely brittle materials as they are capable of local plastic deformation [27] even when failing apparently brittle [68]. When comparing the fracture surfaces of tough and brittle metallic glasses, macroscopically brittle samples exhibit local plasticity [27], because cracks evolve preferably in shear bands [27,76]. Fracture, however, is not equal to the runaway of a single shear band as it requires the formation of cavities and new surfaces [65,69]. Under uniaxial tensile load, brittle failure is mostly observed, while under uniaxial compressive or multiaxial load, plastic deformation due to the formation of multiple shear bands can be observed prior to failure [27]. Due to their common dependence on shear band formation and propagation, fracture strength and yield strength are related [27].

Despite their limited plasticity, metallic glasses can be highly tough materials [31]. In tough metallic glasses, such as Pt- [77] or Pd-based [31] metallic glasses, the plastic zone shields the crack tip and enables crack tip blunting by formation of multiple shear bands in front of the crack tip. Therewith energy is dissipated and crack extension hindered [77,78], leading ideally to an increase in toughness as the crack extends [31]. While the fracture toughness is generally an intrinsic material parameter [27], fracture toughness in metallic glasses is strongly affected by extrinsic parameters such as thermal history, residual stress and precision in sample preparation [79] as well as by intrinsic parameters such as the ability of shear band extension

and multiplication. As shear band extension and multiplication is dependent on the sample geometry due to the confinement of shear bands, the fracture toughness of metallic glasses is also geometry dependent [27,80]. This can be rationalized with the increasing number of shear bands below a critical sample size. The formation of new shear bands is – at least for Pd-based glasses – energetically more favourable in small than in large samples [81]. Extensive shear banding bifurcates the growing crack while promoting a mixed mode failure, enhancing fracture toughness [82].

The fracture toughness values of large samples scatter more strongly than those of small samples [24,81,83]. To be able to compare valid fracture toughness values, the samples need to be significantly larger than the ligament width and bending radius [81,84,85]. These conditions are typically satisfied when following standards like ASTM E399. However, the minimum samples sizes according to ASTM E399 need to be taken cautiously for metallic glasses, as they are close to the sample-size-dependence threshold of metallic glasses [84]. The required large sample sizes are difficult to produce with many metallic glasses, hence a low number of valid fracture toughness values can be found in literature [27]. Therefore, most toughness values in literature describe the conditional fracture toughness that cannot be directly compared to each other due to geometry differences [24,27,82]. Even when following standards, fracture toughness is dependent on the geometry, since fracture toughness depends on the fracture mode as well as on the notch root radius [27]. The most investigated fracture mode is crack opening (mode I, Fig. 3a). However, toughness under in-plane shear (mode II, Fig. 3b) conditions can be larger [27,82] while showing less scattering values [76].

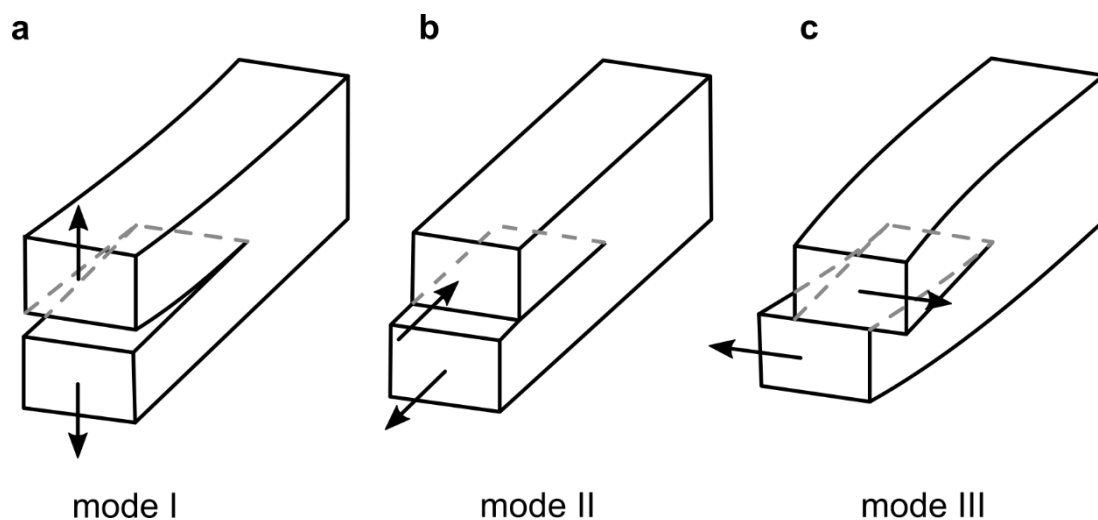


Fig. 3: Schematic of the three different fracture modes. Adopted from [86].

The principal parameter that influences the fracture toughness is the composition, which determines structure and bonding of the metallic glass [27,87]. Especially the energy barrier for cavity formation is crucial for fracture toughness [88], since cavities are the first stage of a crack. The higher the energy for cavitation formation in the metallic glass, the more mechanical energy is required to create a cavity and thereby the nucleus of a crack. The chemical heterogeneity in metallic glasses enhances the energy barrier for cavity formation, as atoms may need to diffuse to create a surface with the energy available [88]. Changing the bonding by microalloying is one route to toughen metallic glasses intrinsically [27]. Impurities from the production process such as oxygen can be detrimental to fracture toughness due to the potential formation of inclusions [27,89]. Maybe the most prominent design guideline for tough metallic glasses is based on Poisson's ratio and was introduced by Lewandowski *et al.* [90]. As Poisson's ratio combines the elastic constants of resistance against size change (bulk modulus) and shape change (shear modulus) [78,91], Lewandowski *et al.* proposed a brittle-to-tough transition at a Poisson's ratio of 0.31-0.32 [90,92]. Being an indicator for covalent bonding [91], a low Poisson's ratio would require atoms to disturb the bonding with neighbouring atoms to move, making atomic rearrangements and thus plastic deformation more energy expensive than in glasses with large Poisson's ratio [75]. Yet the universality of the Poisson's ratio criterion has been contested [50,93–98], as metallic glasses with different deformation behaviour but equal Poisson's ratio have been reported [93]. The Poisson's ratio-

based brittle-to-tough transition is instead proposed to be alloy specific [95] and dependent on the experimental setup [82].

Next to approaches to improve toughness based on the composition of the glass, the production as well as thermal and mechanical processing routes of metallic glasses can be utilised to enhance toughness by adjusting the amount of free volume [27,83,99] and increasing the energy stored in the metallic glass [43], leading to structural rejuvenation. This energy can be introduced thermally [43] or by mechanical treatments that induce not only energy, but also anisotropy and inhomogeneities preventing easy shear band propagation [50]. These mechanical treatments are reported to introduce a specific capacity of work-hardening into metallic glasses [49]. The introduction of “pre-existing shear bands” enhances toughness by crack deflection [98].

As small sample sizes enhance plasticity [50,64,74,75], extrinsic toughening routes aim to form microstructures by introduction of predominantly ductile, crystalline second phases such as dendrites or layers to stabilize the shear localization in metallic glasses [27] and confine the space available for shear bands [50,69]. However, while the controlled introduction of crystalline phases can enhance toughness, crystallisation due to annealing is reported to deteriorate the toughness of metallic glasses [100]. These nano-structured glasses will be discussed in more detail in section 1.4. All approaches to enhance toughness in metallic glasses have in common that they aim to prevent shear band propagation and to create multiple shear bands [50].

Nevertheless, metallic glasses are not predominantly attractive for structural applications because of one single mechanical property, but because of their unique property combinations [17] such as high strength and toughness, two mutually exclusive properties in metals [101]. This combination of strength and fracture toughness constitutes damage tolerance [31].

1.3. Quantum mechanical prediction of metallic glass properties

To predict the mechanical properties of metallic glasses, empirical models such as the one by Zhang [102] are proposed. Zhang predicts the mechanical properties as well as the glass

forming ability based on the estimated Young's modulus [102]. Those empirical models, however, take into account macroscopic properties and depend on databases of amorphous and crystalline alloys, interpolating the properties of known alloys to predict the properties of novel alloys by a composition based rule of mixture approach [102], for example. However, as already indicated by Davis *et al.* in 1982, the electronic structure is decisive for the mechanical properties [103], especially hybridization [103] and electron density [104,105]. Hence, rule of mixture approaches are more reliable when based on the ratio of atomic bonds instead of composition [106].

Following the line of Davis *et al.* [103], the macroscopic properties are dependent on the atomic interactions [106], composition and topology [103,107]. Especially the elastic constants reflect topology and atomic bonding on the macroscopic scale, as they can be calculated from the energy volume curve in the continuum [102,108]. The origin of stiffness needs thus to be sought in the bond strength [106] or valence electron density [104], if the bonding is predominantly metallic [109]. According to Schnabel *et al.* [110], however, the stiffness in terms of bulk modulus does not scale universally with valence electron density. They report based on a correlative analysis of density, electronic structure, and the integrated crystal orbital Hamilton population (COHP) [111] as a measure for bond energy that the bulk moduli of metal-metal and metal-metalloid glasses scale best with bond energy density [110]. Hence, they propose the bond energy density as the origin of stiffness in metallic glasses [110].

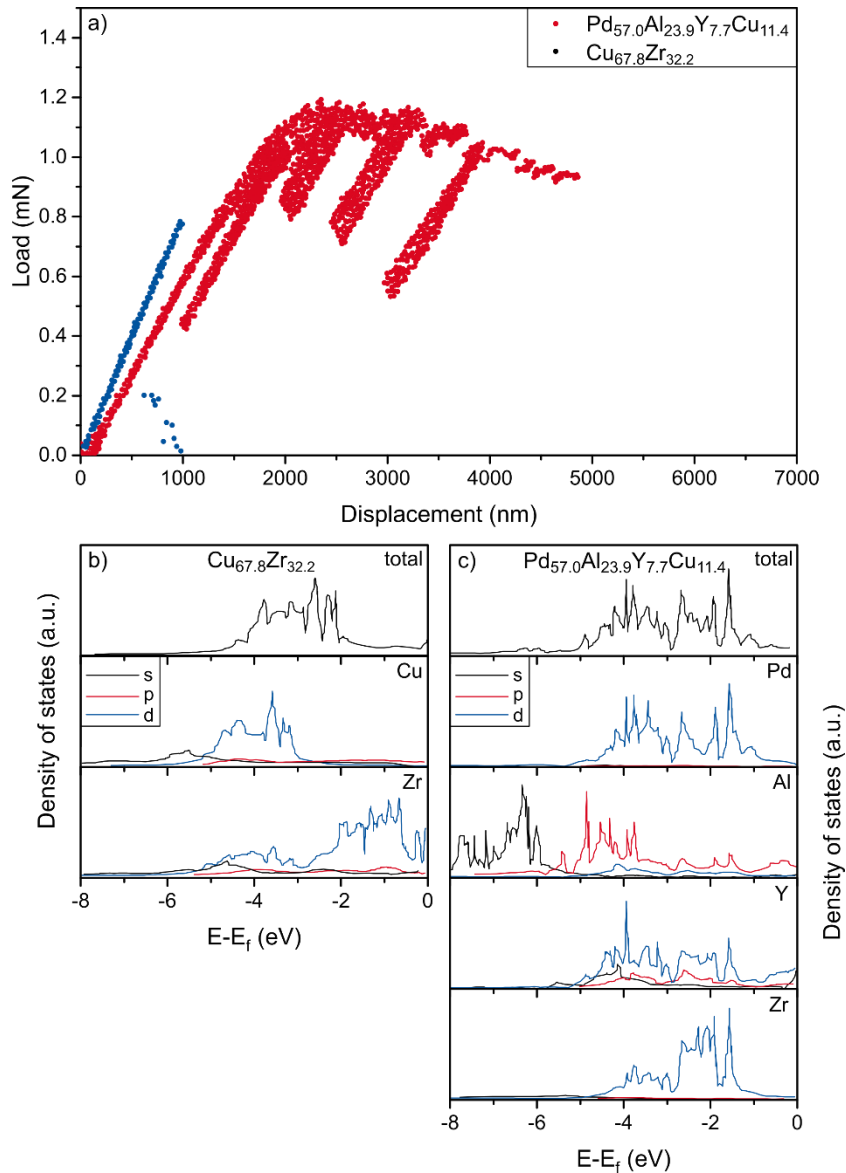


Fig. 4: Comparison of tough $\text{Pd}_{57.0}\text{Al}_{23.9}\text{Y}_{7.7}\text{Cu}_{11.4}$ and brittle $\text{Cu}_{67.8}\text{Zr}_{32.3}$. a) Load-displacement curves of micro-mechanical bending experiments. Electronic density of states (DOS) of b) $\text{Cu}_{67.8}\text{Zr}_{32.3}$ and c) $\text{Pd}_{57.0}\text{Al}_{23.9}\text{Y}_{7.7}\text{Cu}_{11.4}$ showing the total as well as the partial DOS. Figure adapted from [93] under the Creative Commons Attribution 4.0 license. Data of the DOS is smoothed by adjacent averaging to enhance clarity of the figure.

Next to stiffness, also the toughness of metallic glasses can be linked to the electronic structure. The electronic structure dependence of toughness of metallic glasses is already hidden in the proposed design guideline based on Poisson's ratio [90], because Poisson's ratio corresponds to bond covalence [22]. Based on literature, the more covalent, directional the bonding, the lower fracture toughness is expected [78,87]. The surface energy, which is

important due to the formation of surfaces during crack growth, is influenced by the bond strength [87] and hence the electronic structure. Comparing the electronic density of states (DOS) of a brittle $\text{Cu}_{67.8}\text{Zr}_{32.2}$ and a tough $\text{Pd}_{57.0}\text{Al}_{23.9}\text{Cu}_{11.4}\text{Y}_{7.7}$ metallic glass (load-displacement curves presented in Fig. 4a), more hybridization is observed between Cu and Zr (Fig. 4b) than between the main constituents Pd and Al of the Pd-based metallic glass (Fig. 4c). Hence, a low fraction of hybridized bonds is proposed to be a fingerprint for toughness in metallic glasses since it promotes shear relaxation and therewith the formation of shear transformation zones [93]. This is consistent with the COHP analysis that shows more anti-bonding states and thereby weaker bonding for $\text{Pd}_{57.0}\text{Al}_{23.9}\text{Cu}_{11.4}\text{Y}_{7.7}$ than for $\text{Cu}_{67.8}\text{Zr}_{32.2}$ [93]. This fingerprint can be used to qualitatively estimate the plastic deformation behaviour of metallic glasses. However, a quantitative predictor function has not been available so far. Therefore, one focus of this work is to establish a quantitative correlation between the fracture toughness and the electronic structure of metallic glasses.

1.4. Nano-structured glasses

While intrinsic toughening of metallic glasses focuses on crack initiation, extrinsic toughening strategies focus on crack propagation and aim to introduce a microstructure in metallic glasses to hinder crack propagation. A microstructure in metallic glasses can be established by the introduction of second phases. The introduction of crystalline, quasi-crystalline or second amorphous phases into a metallic glass results in glass matrix composites [112,113]. One can differentiate between *ex situ* composites [114,115], where the second phases are added during glass synthesis [113,116], and *in situ* composites [114,117–122], where second phases form during synthesis or processing within the metallic glass [113]. The second phases confine the movement of shear bands and promote shear band multiplication [28,113,114,117,121–123]. However, not alone the presence of a second phase is sufficient to enhance the mechanical properties, but also the distribution of second phases is important, which needs to be on the correct length scale [113,117]. To prevent brittle failure of a metallic glass, the distance between the second phases is required to be of the size of the critical crack length or smaller [124] and the distribution of the second phases needs to be homogeneous [116,117,123].

Deformation induced phase transformations such as the martensitic transformation in the second phases are beneficial for the mechanical properties [123]. Dendritic precipitations have been proven efficient to enhance the mechanical properties [113,118,119,122]. Pekarskaya *et al.* report that soft crystalline phases carry the plastic deformation partially by dislocations if the stress concentration in the glassy matrix is large enough [120]. As thin films, crystalline-amorphous multilayers have been shown to exhibit enhanced mechanical properties [125].

Alternatively to crystalline phases, phase separation to introduce a second amorphous phase [126,127] or the design of an amorphous-amorphous microstructure similar to the microstructure of crystalline materials – known as nano-glasses – is proposed to enhance the mechanical properties, especially plasticity [128]. Phase separation usually occurs if the enthalpies of mixing between all constituent pairs except one are negative or the mixing enthalpy of one constituent pair is significantly more negative than the others [36,126,127]. Nano-glasses contain consolidated glassy particles, mimicking a nanocrystalline microstructure. Hence, nano-glasses contain glassy regions and lower-density glass-glass interfaces. Nano-glasses show enhanced plasticity and even work-hardening due to the formation and interaction of multiple shear bands at the glass-glass interfaces [128,129]. However, due to the lower activation barrier of shear bands in nano-glasses, the yield strength of nano-glasses is lowered compared to conventional bulk metallic glasses [128].

Recently, the *in situ* formation of compositionally nano-structured metallic glasses has been reported in thin films [130]. In the Co-Ta-B system, a self-organized periodic lamellar nanostructure formed with a wavelength in the order of magnitude of 10^1 nm that is decreasing with increasing B content. Concomitantly, hardness, Young's modulus, fracture strength and fracture toughness increase significantly [130]. The origin of the two amorphous phases is not clear yet, because all enthalpies of mixing are negative [130], which is not expected for phase separation according to literature [36]. Nevertheless, the *in situ* formation of nanostructured metallic glasses is proposed as a design route for enhanced mechanical properties [130]. The

self-organized nano-structured metallic glass formation with increasing B contents opens a composition space promising in terms of mechanical properties, which is not explored yet.

1.5. Research questions

The previous sections have given an overview about the mechanical properties and underlying physical mechanisms thereof (section 1.2): A low fraction of hybridized bonds on the overall bonding has been identified as the fingerprint of high fracture toughness [93]. The stiffness of metallic glasses scales with bond energy density, hence a high bond energy density has been proposed to be the origin of high stiffness [110]. Thus, quantum mechanical predictions of mechanical properties and topology can be a powerful tool for the design of metallic glasses for structural applications (section 1.3). However, since quantum mechanically guided design strategies cannot quantitatively predict fracture toughness and thermal expansion yet, this work focuses on the following research questions to advance the quantum mechanically based design of the mechanical properties and thermal expansion of metallic glass thin films:

- I. Can the thermal expansion of metallic glasses be predicted *ab initio* by the Debye-Grüneisen model?

The coefficient of thermal expansion (CTE) is of critical importance to minimize the amount of post-machining as well as due to the importance of thermal stresses in micro-mechanical devices and thin film applications [17,20,21]. While the CTE has been predicted by *ab initio* methods using the Debye-Grüneisen model for crystalline cubic [131–137], tetragonal [136,137], trigonal, and hexagonal [137] materials, it has not been employed to predict the CTE of amorphous materials. Hence, the goal is to predict the thermal expansion of metallic glasses *ab initio* using the Debye-Grüneisen model and to validate the prediction experimentally.

- II. Can the fracture toughness of metallic glasses be predicted quantitatively?

Schnabel's *et al.* qualitative design proposal that the fracture toughness is increased by a low fraction of hybridized bonds [93] will be validated by comparing the electronic structure of metallic glasses with fracture toughness data reported in

literature [31]. The aim is to quantify the fraction of hybridized bonds and to relate it to the fracture toughness of metallic glasses. Thereby, the proposal of an enhanced, quantitative predictor function for fracture toughness of metallic glasses based on the crystal orbital overlap population [138] is envisaged.

- III. Can metalloids-containing metallic glasses and network glasses be discriminated based on their electronic structure and topology?

Co-Ta-B metallic glasses have been reported to exhibit excellent fracture toughness and strength, hardness as well as Young's modulus with a B content of up to 49.5 at.% due to the formation of nanolaminates [130] and a high bond energy density [110]. High B-containing solids with B contents around 90 at.% are reported to be ultra-hard as a consequence of an icosahedral B-network [139–141]. However, the transition region between 50 and 90 at.% B has not been investigated yet. Hence, the goal is to identify topology and electronic structure differences between B-containing metallic glasses and icosahedral network formers – B-containing network glasses or amorphous borides – in terms of topology and electronic structure to identify potential criteria for the discrimination between metallic glasses and network glasses.

- IV. What is the effect of free volume of metallic glasses on the electronic structure?

Increasing the free volume content has been proposed to enhance plastic deformation of metallic glasses and is often referred to as “structural rejuvenation” [43]. Recently, an enhanced free volume content was reported to induce work hardening and hence enables stable plastic deformation [49]. Free volume in metallic glasses consists of volume fractions containing atoms with lower coordination number [53], which allow the atoms to move within their nearest neighbour cage without energy change [54]. Thus, atomic mobility is enhanced [22,53] as the free volume lowers the energy barrier for shear transformations in metallic glasses [22,53] promoting plastic deformability [51]. While literature often focusses on the free volume induced changes in internal energy [43,51,142–144]

and topology [49,145–147], the effect of free volume on the electronic structure has so far been overlooked. Therefore, the goal is to understand the effect of free volume on the electronic structure and hence chemical bonding based on *ab initio* calculations by systematically increasing the free volume content of Cu₇₀Zr₃₀.

2. Methods

In the following sections, the background of the theoretical and experimental concepts and methods used in this work is introduced. As the details of the theoretical and experimental strategies employed differ depending on the research question addressed, the reader is referred to the original publications attached to this work for the detailed setups used.

2.1. *Ab initio* calculations

Ab initio calculations are atomic calculations with the composition and topology as the – in principle – only input parameters. The calculation of forces between the atoms requires solving the multi-body Schrödinger equation. This is already challenging for He atoms containing two electrons. For a typical *ab initio* calculation that contains several atoms larger than hydrogen, the solution of the multi-body Schrödinger is therefore analytically not possible and computationally cost-intensive. To use computational resources efficiently, the *ab initio* calculations conducted here are based on density functional theory (DFT), which will be introduced here in a nutshell.

Hohenberg and Kohn proved the possibility to determine material properties as well as the total energy based on the electron density $n(\mathbf{r})$ [148]. The total energy of the system is calculated by

$$E = \min_n \{ F[n] + \int d^3r n(\mathbf{r})v(\mathbf{r}) \}. \quad (1)$$

In eq. 1, $v(\mathbf{r})$ is the single-body potential, \mathbf{r} the atomic position, and $F[n]$ is the universal functional

$$F[n] = \min_{\Psi \rightarrow \infty} \langle \Psi | \hat{T} + \hat{V} | \Psi \rangle \quad (2)$$

with the kinetic energy operator \hat{T} , the potential energy operator \hat{V} and the wavefunction Ψ [149]. Kohn and Sham reduced the computational effort further by introducing non-interacting electrons with the same density as in the original problem, resulting in Kohn-Sham eigenvalues $\varepsilon_{j\sigma}$ and single-electron orbitals $\Phi_{j\sigma}$ by the non-interacting Schrödinger equation [149]

$$\left\{ -\frac{1}{2}\nabla^2 + v_{\sigma}(\mathbf{r}) \right\} \Phi_{j\sigma}(\mathbf{r}) = \varepsilon_{j\sigma} \Phi_{j\sigma}(\mathbf{r}) \quad (3)$$

where $v_{\sigma}(\mathbf{r})$ is the potential energy. Based on eq. 2 and 3, the energetic contributions for the ground state are separated into the kinetic contribution $T_S[n]$; the Hartree functional $U[n]$ describing the electron-electron interactions; and the exchange-correlation functional $E_{XC}[n]$:

$$F[n] = T_S[n] + U[n] + E_{XC}[n] \quad (4)$$

This solution for the ground state energy is exact [149,150]. However, the exchange-correlation functional is only defined by eq. 4 and hence, in practice, approximations are used. In this work, the general gradient approximation is employed (GGA, eq. (5)), which includes not only electron densities $n_{\uparrow}(\mathbf{r})$ and $n_{\downarrow}(\mathbf{r})$ (arrows indicating spin-up and spin-down electrons) but also the electron density gradients [149].

$$E_{XC}^{GGA} = \int d\mathbf{r}^3 e_{XC}^{GGA}(n_{\uparrow}(\mathbf{r}), n_{\downarrow}(\mathbf{r}), |\Delta n_{\uparrow}(\mathbf{r})|, |\Delta n_{\downarrow}(\mathbf{r})|) \quad (5)$$

Here, the GGA versions developed by Perdew and Wang (PW-91) [151] and Perdew, Burke and Ernzerhof (PBE, eq. 5) [152] are utilized. Based on these principles, by finding the minimum of the energy, the ground state energy can be determined.

To produce an amorphous structure *in silico*, *ab initio* molecular dynamics (AIMD) is used. Thereby, the forces between the atoms i and j are calculated from the total energy instead of giving a classical potential as it is done in classical molecular dynamics. With these forces $f(r_{ij}(t))$, the movement of the atoms in a given timestep Δt is determined and the atoms are moved from their initial position $r(t)$ to the new position $r(t+\Delta t)$, typically by the Verlet algorithm (eq. 6) [153].

$$r(t + \Delta t) = 2r(t) - r(t - \Delta t) + (\Delta t)^2 \sum_{i \neq j} f(r_{ij}(t)) \quad (6)$$

In the new configuration, energy and forces are then determined again by solving eq. (3) to determine the movement in the next iteration steps.

However, these calculations are carried out at 0 K. To introduce temperature into AIMD, two approaches are the most common ones used and implemented in the openMX-code [154,155], which is used for AIMD in this work, employing canonical ensembles: controlling the temperature by velocity scaling or a Nosé-Hoover thermostat. For velocity scaling according to Woodcock [156], the mean squared velocity of the atoms is calculated for a specified temperature and compared to the actual mean squared velocity of the atoms in the system. Based on the difference between specified and actual mean squared velocity, a scaling factor is calculated that adjusts the position $r(t-\Delta t)$ in eq. (6) in such a way that the atoms are effectively accelerated or decelerated to maintain the specified temperature [156]. With the Nosé-Hoover thermostat, the system is connected to a heat bath via friction coefficients. The heat bath controls the atomic velocities and keeps the temperature constant [157].

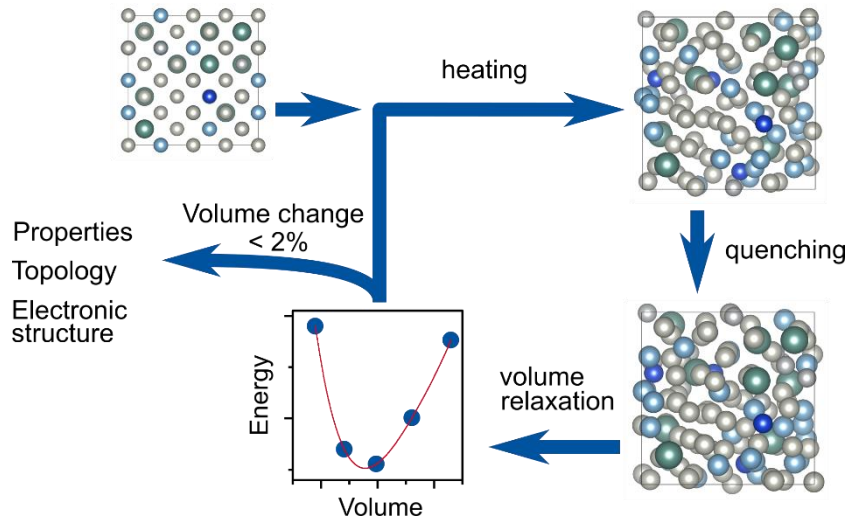


Fig. 5: Schematic representation of the *ab initio* modelling routine for metallic glasses introduced by Hostert *et al.* [158].

The modelling routine for metallic glasses employed in this work was developed by Hostert *et al.* [158] and is schematically shown in Fig. 5. A cubic supercell containing 115 atoms that are

initially placed randomly on a bcc lattice is heated to 4000 K for 400 fs. Subsequently, the cell is quenched to 0 K by geometry optimization. Afterwards, the volume of the cell is relaxed to minimize the energy while keeping the relative atomic positions constant. This heating – quenching – relaxation cycle is iterated until the volume change between two subsequent cycles is smaller than 2%. Based on the final structural model, the ground-state properties, electronic structure, and topology are then calculated.

From the *ab initio* calculations, the elastic properties can be directly determined by hydrostatic deformations and volume conserving shear distortions in the case of a cubic cell. The bulk modulus is proportional to the second derivative of the energy-volume curve. Thus, by hydrostatic expansion and compression of the simulation cell while keeping the relative atomic positions fixed, the bulk modulus is calculated by fitting the obtained energy-volume curve with the Birch-Munarghan equation of state [159]:

$$-\left(\frac{\delta E_{el}}{\delta V}\right)_T \frac{1}{K_0} = 3e(1 + 2e)^{\frac{5}{2}} \left[1 - \frac{1}{2} \frac{\delta_3}{\delta_2} e + \frac{1}{3} \frac{\delta_4}{\delta_2} e^2 + \dots \right] \quad (7)$$

Where K_0 is the bulk modulus at zero pressure, E_{el} the elastic energy, e the negative strain and $\frac{\delta_3}{\delta_2} = 3(4 - K_0')$; and $\frac{\delta_4}{\delta_2} = 9K_0K_0'' + 9(K_0')^2 - 63K_0' + 143$ with K_0' and K_0'' being the first and second derivative of K_0 to the pressure [159], the latter one being of importance to describe the pressure dependence of K_0 and K_0' . The elastic constants of shear in the cubic system, c_{11} , c_{12} and c_{44} are obtained via the volume conservative shear distortions D and D_{44} (eq. 8 and 9) and subsequent fitting of the resulting energy-shear dilatation curves, eq. 10 and 11, where δ is the distortion matrix element, V the volume and E the energy of the supercell [160].

$$D = \begin{pmatrix} 1 + \delta & 0 & 0 \\ 0 & 1 - \delta & 0 \\ 0 & 0 & \frac{1}{1 - \delta^2} \end{pmatrix} \quad (8)$$

$$D_{44} = \begin{pmatrix} 1 & \delta_{44} & 0 \\ \delta_{44} & 1 & 0 \\ 0 & 0 & \frac{1}{1 - \delta_{44}^2} \end{pmatrix} \quad (9)$$

$$\Delta E = V(c_{11} - c_{12})\delta^2 + O(\delta^4) \quad (10)$$

$$\Delta E_{44} = 2Vc_{44}\delta_{44}^2 + O(\delta_{44}^4) \quad (11)$$

2.2. Bonding analysis

Here, bonding analysis is understood in terms of topology and electronic structure analysis. The main tool for the topological analysis of short-range ordered materials is the radial distribution function $R(r)$ and the closely related reduced pair distribution function $G(r)$. $R(r) \cdot dr$ describes the number of atoms in a shell of thickness dr in a distance r from an arbitrary atom [161] as defined by eq. (12):

$$R(r) = \sum_i \sum_j \frac{b_i b_j}{\langle b \rangle^2} \delta(r - r_{ij}) \quad (12)$$

$$g(r) = \frac{R(r)}{4\pi r^2 \rho_0} \quad (13)$$

b_i , b_j , $\langle b \rangle$ are the atomic scattering lengths of the atoms and the mean scattering length of the sample, which are necessary to compare the *ab initio* data with experimental results from high energy scattering (section 2.5). $R(r)$ can be directly calculated from the atomic positions in the system. The pair distribution function $g(r)$ (eq. (13) with ρ_0 the atomic number density) is the histogram of bond distances with an arbitrary atom as the origin. Due to the large number of atoms in physical systems, the pair distribution function is a quasi-continuous function [161].

The pair distribution function $g(r)$ describes very well the short-range order for small bond distances r , while it asymptotes to 1 for large bond distances. The amplitude of the structural information-containing oscillations decreases with $1/r$. However, also the uncertainties in the experimental data scale with $1/r$, hence the emphasis of the short bond distances in $g(r)$ is statistically not significant [161]. Therefore, the reduced pair distribution function $G(r)$ is used for analysis, as the uncertainties are constant with r and $G(r)$ can be directly obtained by a Fourier transform of the experimentally obtained structure factor (section 2.5). $G(r)$ is defined in eq. 14 [161].

$$G(r) = 4\pi r \rho_0 (g(r) - 1) \quad (14)$$

Another topological parameter is the coordination number CN, describing the number of nearest neighbours of an arbitrary atom. These nearest neighbours are within the first coordination shell around an atom that is described by the first main peak in $R(r)$ and $G(r)$. The first minimum in $R(r)$ or $G(r)$ is used as a cutoff-radius when counting the number of atoms surrounding an atom. Next to counting the number of atoms within the first coordination shell surrounding an atom and averaging this number for all atoms, the CN can be calculated by integrating $R(r)$ within the boundaries r_1 and r_2 , which are the boundaries of the first coordination shell [161]:

$$CN = \int_{r_1}^{r_2} R(r) dr \quad (15)$$

By considering only certain atomic pairs for these topological quantities introduced here, the partial correlation functions or CN are obtained while the total quantities are the average of the partial ones. The total $R(r)$ and $G(r)$ as well as the total CN are also obtainable by X-ray scattering.

For the bonding analysis based on the electronic structure, the starting point is the electronic density of states (DOS). The DOS describes the number of occupied and unoccupied electronic states as a function of energy [162]. Thus, the DOS is an integrated measure for the band structure. The DOS is a real space quantity, while the band structure is determined in reciprocal space [138]. The peak positions and peak shapes as well as the position of the Fermi level allow conclusions about the bonding in the material. The DOS analysis gains added value by calculation of the partial, orbital-resolved DOS, i.e. the DOS per alloy constituent. This enables the identification of the peaks in the total DOS as well as conclusions about the hybridization of orbitals.

For an in-depth bonding analysis, the concepts of the crystal orbital overlap population (COOP) and the crystal orbital Hamilton population (COHP) are considered. The COOP weights the DOS by the orbital overlap [138]. Therefore, the probability to find an electron in a two-centre molecular orbital Ψ built from two atomic orbitals X_1 and X_2 needs to be considered:

$$1 = \int \Psi^2 dt = \int (c_1 X_1 + c_2 X_2)^2 dt = c_1^2 + c_2^2 + 2c_1 c_2 S_{12} \quad (16)$$

S_{12} is the overlap integral between X_1 and X_2 . The term $2c_1 c_2 S_{12}$ describes the interaction between atomic orbitals and is the weighting factor to obtain the COOP from the DOS [138].

The COHP is an energy-resolved bonding descriptor [111]. This is again a weighted representation of the DOS, however, here the DOS is weighted by an occupation number and is multiplied with an Hamiltonian operator, resulting in the energy resolution [111]. The COHP does, as the COOP, not only give information about bonding (negative COHP, positive COOP) and antibonding states (positive COHP, negative COOP), but integration of the COHP up to the Fermi levels yields a measure of bond strength [163]. However, COOP and COHP cannot be directly calculated from the output of projector augmented wave (PAW) codes such as the Vienna Ab-Initio Simulation package (VASP) used here for the calculation of the DOS [164,165], which is a consequence of the delocalized nature of the plane-waves and PAWs [163]. The LOBSTER software is used to project the delocalized PAWs onto localized orbitals and subsequently to calculate the COOP and COHP [166].

2.3. Magnetron sputtering

The metallic glass samples in this work were synthesised as thin film metallic glasses by magnetron sputtering. In magnetron sputtering, ions of a working gas – typically Ar^+ ions – are accelerated towards a cathode made of the material to sputter – the target – by applying a negative potential to the cathode. The process takes place at low pressures which are realized by the introduction of the inert working gas into a high-vacuum chamber. The ion source in magnetron sputtering is a plasma, i.e. an electrically neutral mixture of ions and electrons, that is concentrated in the vicinity of the target by a magnetic field surrounding the cathode [167,168]. When an ion impinges the target surface, the momentum of the arriving ion is reversed and partially absorbed, eventually causing the ejection of a target atom if the energy was sufficiently high [167,168]. The efficiency of ejecting target atoms by sputtering is called the sputter yield and depends on the target material and potential as well as the ion species, energy and impinging angle [167,168]. Hence, the target composition or – when using

elemental targets – the power ratio is not equal to the film composition. Parameters to define composition, structure and morphology of the deposited film are the deposition rate, substrate temperature, substrate bias voltage, particle flux and the sputtering mode [167].

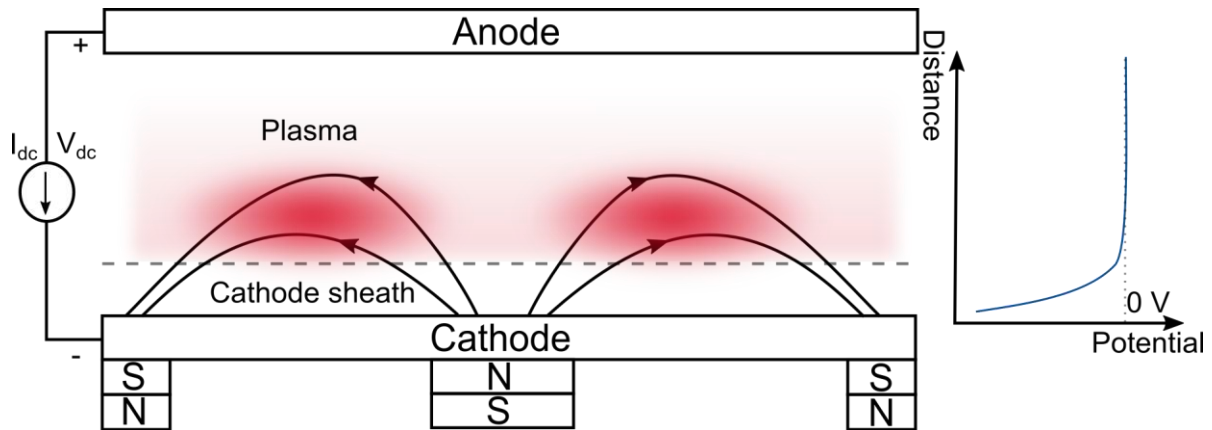


Fig. 6: Schematic of the magnetron sputtering process based on [168,169].

Different sputtering modes are available. Among those, the simplest one is direct current magnetron sputtering (DCMS), which is usable with all conducting materials, while radio frequency magnetron sputtering (RFMS) can be employed also for non-conducting materials. Both methods are used in this work, DCMS for metallic targets and RFMS for B targets. For DCMS, a constant voltage is applied between cathode and anode, ionizing the gas atoms. As the plasma is quasineutral, the voltage is mainly found in the region between the plasma and the cathode, called the cathode sheath, as schematically shown in Fig. 6 [169]. The cathode sheath thickness is in the order of mm [169]. Due to the potential difference in the cathode sheath, the ions are accelerated towards the cathode, which is the target. Next to sputtering target atoms when impinging the target, the ions cause the ejection of secondary electrons that are accelerated away from the cathode to the plasma and provide the energy for the plasma [168]. With the help of magnetic fields, in magnetron sputtering the plasma is concentrated close to the cathode. Confining the movement of electrons in this dense plasma region increases the lifetime of the electrons and allows the usage of lower voltages and deposition pressures compared to a pure DC-glow discharge without magnetic fields [168]. Crucial parameters are the target-to-substrate distance and the chamber pressure as both

influence the deposition rate [167,168] as well as the number of collisions and hence scattering events of atoms during sputtering [170]. The latter is decreased due to the low deposition pressure in magnetron sputtering [168].

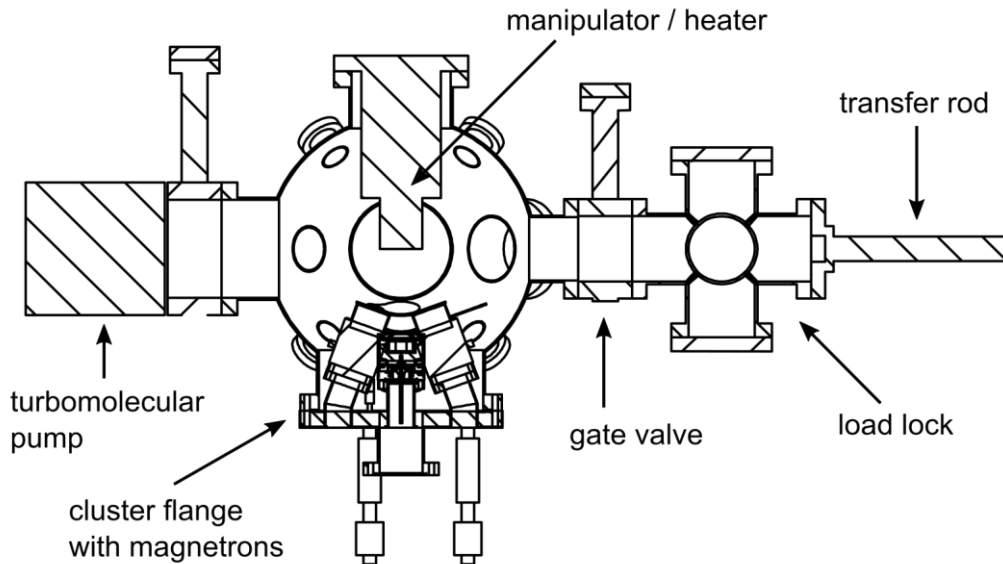


Fig. 7: Schematic of the ultra-high vacuum deposition system used. Visible in the centre is the main deposition chamber with the cluster flange of four 2-inch cathodes on the bottom and the substrate holder at the top; to the right the separately pumped load lock that enables a fast exchange of samples. Load lock and main chamber are separated by a gate valve.

Charge builds up at the surface of non-conducting targets due to immobile electrons, which would be neutralized by incoming positive ions. Thereby, the cathode would be shielded by a neutral layer. To avoid neutralization of the cathode's surface, an alternating potential is applied with a frequency sufficiently high to suppress charge neutralization while recharging the target surface with electrons [167]. In practice, a frequency of 13.56 MHz is used (radio frequency, RF) [167]. Insulating materials can be directly sputtered by RFMS, while for conductive materials the power supply needs to be capacitively coupled with the target [167]. The oscillating electrons in the radio frequency field generate the plasma, thus the secondary electrons necessary for DCMS are not required to sustain the RF-plasma. While it is possible

to sputter nearly all materials by RFMS, operating RFMS is more challenging than DCMS due to the complexity of matching the impedance of the plasma to the generator [167].

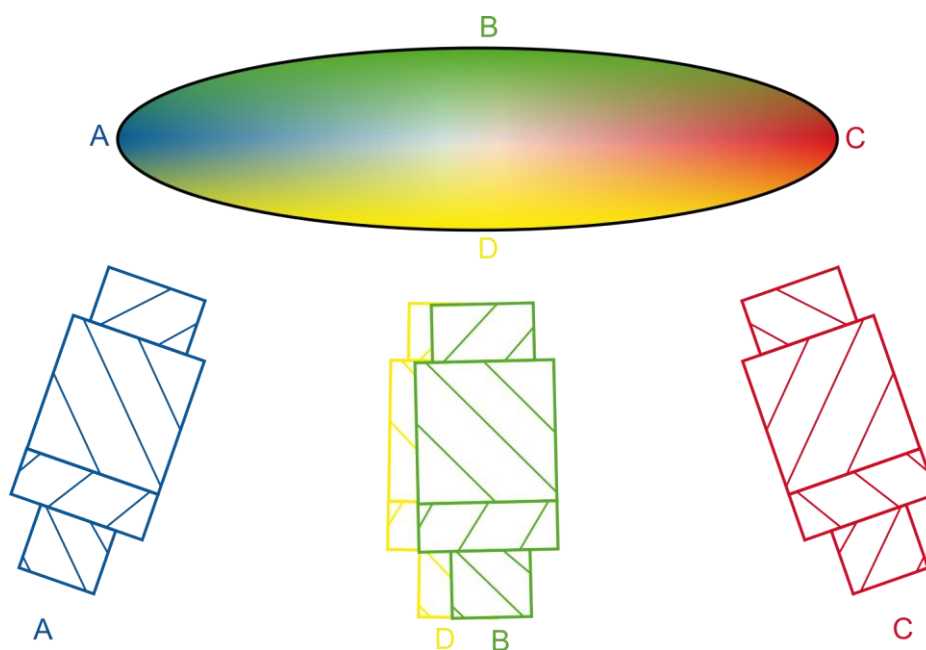


Fig. 8: Schematic of sample library synthesis by magnetron sputtering. The four magnetrons with targets of element A, B, C, and D (bottom) are tilted by 20° and the substrate centre is placed in the common focal point (top, not to scale). Thereby, the composition of the sample changes along the two perpendicular composition gradients A-C and B-D.

In this work, an ultra-high vacuum deposition system with four 2-inch cathodes was used (Fig. 7). The cathodes were tilted by 20° to the substrate normal to allow the deposition of compositional gradients (Fig. 8), creating sample libraries on the substrate wafer [171]. The substrate to target distance was 10 cm. Samples were deposited onto different types of substrates: Single crystal Si wafers for chemical characterization as well as for probing the mechanical properties and atom probe tomography, polyimide (Kapton) for high energy X-ray scattering on sample libraries, and NaCl substrates to obtain powder samples. For the latter, the NaCl substrates were dissolved in water after deposition and the resulting thin film flakes were cleaned in isopropanol and acetone. The cleaned thin film flakes were ground in a mortar to obtain metallic glass powders [172]. For compositionally homogeneous films as required for

the powder samples, the substrate was rotated. The reader is referred to the original publications attached for details of the deposition settings.

2.4. Energy dispersive X-ray spectroscopy

Energy dispersive X-ray spectroscopy (EDX) is used to determine the chemical composition. EDX requires electrons as primary beam and is hence available in many scanning as well as transmission electron microscopes. Due to the electron bombardment, atoms in the sample become ionized. The resulting electron hole is then filled by a higher-energetic electron from a more outer shell while the excess energy is released as a characteristic X-ray photon. Thereby, electron transitions have to satisfy following conditions: I) $\Delta n > 0$; II) $\Delta l = \pm 1$; and III) $\Delta j = -1, 0, +1$, where n is the principle quantum number, l the angular momentum quantum number and $j = l \pm s$ is the total angular momentum with s describing the spin ($\pm 1/2$) [173].

The spatial resolution is determined by the sample as well as the primary electron energy, as every interaction deflects the electron path. Elements with a large atomic number and hence many electrons cause multiple interactions and result in a smaller interaction volume compared to light elements, where the electrons penetrate a larger volume. Additionally, high electron energies cause a larger interaction volume than low electron energies and hence worsen the spatial resolution [173].

The characteristic X-rays are detected by a semiconductor detector made either of Li-doped Si (Si(Li), used in this work) or Ge crystals. The detection principle is the same in both cases: The X-rays create electron-hole pairs until the complete X-ray energy is dissipated. The energy required for one electron-hole pair in Si(Li) is 3.8 eV [173]. Accordingly, the number of electron-hole pairs is proportional to the energy of the X-ray photon. Electrons and holes are separated, the resulting electrical pulse is amplified and analysed in a multi-channel analyser [173]. The detector needs to be cooled by liquid nitrogen to reduce noise and to avoid diffusion of Li.

To avoid contamination of the detector by condensation of hydrocarbons and water from the microscope environment, the detector is separated from the microscope chamber by a window. In very pure vacuum environments, a window is not necessary. The disadvantage of the

window is the absorption of X-rays, especially at low energies. Thus, X-rays of light elements such as B, C, N, and O are lowered in intensity while even lighter elements are not possible to detect [173].

In the EDX spectrum, the peaks of the characteristic X-rays are superimposed on a background caused by bremsstrahlung [173]. From the peak position, one can qualitatively infer the elements present in the sample. For quantitative analysis, one needs to take the peak intensities into account that are proportional to the concentration of the respective constituent. The proportionality constant combines contributions of ZAF, standing for: Z – correction for inelastic scattering due to differences in mean atomic numbers; A – correction for X-ray absorption; and F – correction for X-ray fluorescence. These contributions have to be determined by modelling, called ZAF-correction, or by using a reference of known composition [173].

While EDX is a widely available technique, it is not the ideal solution for light elements such as B. The detector window is not fully transparent for the low K_{α} X-ray energy of 0.183 keV for B [174]. Moreover, the B K_{α} -peak (partially) overlaps with C K_{α} (0.277 keV [174]), which is always detected due to condensation of hydrocarbons during contact with air and impurities of the B target. Hence, to obtain precise and accurate B concentrations, the measurement with reference to a standard sample is necessary.

The composition of the standard sample is determined by time-of-flight elastic recoil detection analysis (ToF-ERDA) in this work. ToF-ERDA enables the quantification of the chemical composition without the usage of a standard sample [175]. In ToF-ERDA, sample atoms are recoiled due to impingement of an ion beam with energies in the MeV range. The energy spectrum of the recoiled atoms is analysed to determine the composition of the sample: the energy allows identification of the element, the intensity conclusions on the composition. To separate the recoiled sample atoms from the scattered atoms of the ion beam, the time-of-flight is considered [173]. The sensitivity of ERDA is approximately independent of the atomic mass [173], and thus suited to determine the composition of samples containing light elements.

ToF-ERDA measurements in this work were carried out at the tandem accelerator laboratory of Uppsala University. Recoils were generated by $^{127}\text{I}^{8+}$ primary ions with a kinetic energy of 36 MeV. The detector telescope consisted of thin carbon foils for the ToF measurement [176] as well as a gas ionization detection system [177] and was situated at an angle of 45° with respect to the primary ions. Hence, both the incidence and exit angles were 22.5° with respect to the specimen surface. Time and energy coincidence spectra were converted into a depth profile using the CONTES software package [178].

The error of ToF-ERDA consists of the systematic uncertainties, which are in the order of 10% for light elements. The systematic uncertainties arise as a consequence of the energy loss of primary and recoiled species as well as the detection efficiency, which is significantly smaller than 1 for light elements such as B [175,176]. The detection efficiency is determined by the probability of electron emission when passing the carbon foils in the detector and the probability of detection [176]. Hence, the detection efficiency is limited by the electron stopping power of the carbon foil [176]. Moreover, statistical uncertainties, caused by counting statistics, were maximum for B with 2%. While the error on the content of light elements is hence rather high and affects the uncertainties of the metal content, the relative compositions can be determined with a higher precision as those are mainly influenced by the statistical uncertainties (supplementary material of [179]).

2.5. High energy X-ray scattering

Since the focus of this work is on metallic glasses and amorphous materials, X-ray scattering will not yield Bragg diffraction peaks that are known from crystalline materials. The scattering method used instead is called “total scattering” and treats Bragg peaks as well as diffuse scattering equally – containing information about the non-crystalline structure [161]. The intensity $I(Q)$ obtained in the total-scattering experiment is corrected for background and Compton scattering and subsequently normalized by the mean atomic scattering length $\langle b \rangle$ of the sample to obtain the structure factor $S(Q)$, eq. (17) [161].

$$S(Q) = \frac{I(Q)}{\langle b \rangle^2} \quad (17)$$

From the structure factor, the reduced pair distribution function $G(r)$ is calculated by a Fourier transform [161]:

$$G(r) = \left(\frac{2}{\pi}\right) \int_0^\infty Q[S(Q) - 1] \sin(Qr) dQ \quad (18)$$

Q is the wavevector in reciprocal space. In the experiment, the limits 0 and ∞ cannot be reached and must be replaced by the limiting Q_{\min} and Q_{\max} . As the scattering data is collected in reciprocal space, the high- Q data are describing the short-range order in the low- r range of $G(r)$ and vice versa. Therefore, one needs to collect data over a Q -range as wide as possible. This can be achieved by using high X-ray energies and a short sample to detector distance. Hence, high energy X-ray scattering was carried out at the synchrotron light source PETRA III at Deutsches Elektronen-Synchrotron DESY in Hamburg. At beamline P02.1, an X-ray energy of 60 keV and a sample to detector distance of roughly 200 mm has been used in combination with a Perkin Elmer XRD1621 area detector [180] to probe the wavevector space up to more than 14 \AA^{-1} .

While the experimental pair-distribution functions are well suited for short-range order information in metallic environments, information on the B-bonds is hard to capture due to the low scattering length of B. The atomic scattering length is a complex quantity, however, for high X-ray energies and scattering in forward direction, the real part is the dominating one and approaches the atomic number, while the imaginary part gains importance close to absorption edges [174]. Hence, B yields a low intensity in the scattered X-rays, while the metals yield a high scattering intensity. As a result, B-metal bonds can be observed in experimental pair distribution functions, while B-B bonds are hardly visible.

2.6. X-ray photoelectron spectroscopy

X-ray photoelectron spectroscopy (XPS) is a surface-sensitive technique to probe the chemical environment in the sample by measuring the binding energy of core and valence electron states [173]. By irradiation of the sample with monochromatic X-rays in ultra-high vacuum,

electrons in the sample are excited and some leave the sample. This is called the photoeffect. The photoeffect can be understood as a three step process: First, the electrons are excited by the impinging X-rays. Thereafter, the excited electrons move through the sample to the surface while potentially exciting secondary electrons. Lastly, some electrons surmount the energy barrier between surface and vacuum – the work function – and leave the sample [181]. The sample contains a small positive potential afterwards as result of the electron hole [181]. The electrons that left the sample are detected and their kinetic energy E_k is measured. E_k contains the impinging X-ray energy $\hbar\omega$ (\hbar : Planck constant divided by 2π ; ω : frequency of X-rays), the binding energy E_B and the work function φ :

$$E_{\text{kin}} = \hbar\omega - E_B - \varphi \quad (19)$$

As $\hbar\omega$ and φ are known, the binding energy is the quantity usually shown. After ejection of the electron from the sample, the remaining electrons react to the positive potential, thus changing the electronic structure in the sample. The so-called final state is hence not identical with the initial state. This can result in satellite and plasmon peaks in the electron spectrum [181].

The electron mean free path in the sample is crucial for the photoelectron to reach the sample surface and is in the range of less than 50 Å [181]. Hence, XPS is very surface sensitive. This leads to the challenge to differentiate bulk and surface properties [181]. As instrumental condition, a ultra-high vacuum (UHV) environment is necessary, not only to allow the photoelectron to travel to the detector, but also to avoid the adsorption of volatile atoms or molecules on the sample surface that interfere with the measurement [181].

2.7. Micromechanical beam bending tests

The fracture toughness can be determined based on linear elastic fracture mechanics (LEFM). LEFM requires completely elastic deformation in the material, plastic deformation is only allowed in small regions, so that the overall deformation remains elastic [86]. If a crack is introduced into a material, a stress concentration field in front of the crack tip will form, which is quantified by the stress intensity factor K . The evolving stress field depends on the loading mode, which is differentiated by crack-opening (mode I), in-plane shear (mode II), and out-of-

plane shear (mode III, Fig. 3). Hence, K depends on the mode present in the sample as well as on the testing geometry [86]. Here, only mode I and K_I are discussed as this mode is the condition important for most applications [86]. The stress in front of the crack tip decreases proportionally to the reciprocal square root of the radial distance. Thus, the stress is maximum in the vicinity of the tip. Due to the large stress at the crack tip, plastic deformation may occur locally, forming a plastic zone with the radius r_p . LEFM requires r_p to be much smaller than the size of the stress field described by K as well as much smaller than the sample dimensions to avoid size effects [86]. If these conditions are satisfied, K_I is a measure for the load at the crack tip and is called fracture toughness. The crack grows when a critical K_{Ic} is reached. An equivalent condition can be formulated based on the energy release rate [86].

Energetically, during crack growth the formation of surfaces as well as the breaking of bonds requires energy, described by $2\gamma Ba$, where γ is the surface energy and B and a are width and length of the crack, respectively. On the other hand, there is the elastic energy released by the growing crack $-\frac{\sigma^2\pi}{2E}Ba^2$, where σ is the crack opening stress and E the Young's modulus. The equilibrium of these energies defines the critical crack length a_c :

$$a_c = \frac{2\gamma E}{\sigma^2\pi} \quad (20)$$

As K_{Ic}/E is equal to the surface energy (2γ), the critical stress intensity factor K_{Ic} is defined by the surface energy, which is known as Griffith criterion [86]:

$$K_{Ic} = \sqrt{2\gamma E} \quad (21)$$

A concept that can be used for inelastic mechanical behaviour is the J-integral, which is the energy integral of the strain energy around the crack tip. It captures the energy change in the elastic system arising from defects such as growing cracks. Being a parameter of the state around the crack tip, the J-concept is equivalent to the K-concept [86].

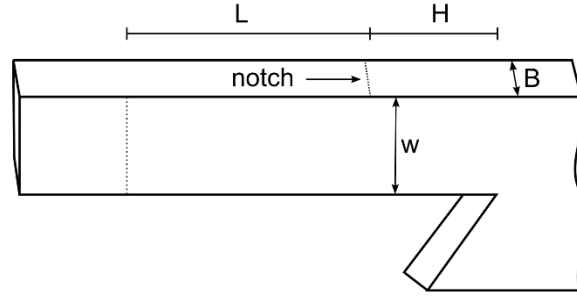


Fig. 9: Schematic of a notched cantilever for micro-mechanical bending experiments after Matoy *et al.* [182].

The fracture toughness is measured by fracturing notched samples, for example as defined by ASTM 399 [27,86]. A typical sample geometry for micro-mechanical bending experiments is the notched cantilever (Fig. 9) as described by Matoy *et al.* [182] with a height:length:ligament width:breadth (H:L:w:B) ratio of 2:5:2.1:1.7 [182] a notch of depth a . The notch can exhibit material bridges at the edges that break first due to the high stress intensity there and thereby introduce a real crack tip at the notch root [182]. The effect of a notch or fatigue pre-crack may be small for metallic glasses [82], while the notch root radius affects shear banding [27]. The fracture toughness of these cantilevers is calculated by eq. (22) [182].

$$K_I = \sigma_F \sqrt{\pi a} f\left(\frac{a}{w}\right) = \frac{F_{\max} L}{B w^{\frac{3}{2}}} f\left(\frac{a}{w}\right) \quad (22)$$

σ_F is the flow stress, F_{\max} the maximum load and $f(a/w)$ a geometry factor depending on the sample geometry used [182]. The measured K_I values are only valid when the sample size fulfils eq. (23) to ensure a sample size independent fracture toughness K_{Ic} , which is a material property.

$$a, w, B \geq 2.5 \left(\frac{K_{Ic}}{\sigma_Y}\right)^2 \quad (23)$$

with σ_Y being the yield stress [27,84,182]. Due to eq. (23), large sample sizes are required to determine the fracture toughness of tough materials. Hence, it is difficult to comply with the sample size conditions for metallic glasses since for most metallic glasses only small sample sizes are available. Samples smaller than required exhibit a larger toughness than K_{Ic} , since

the plastic zone size may be larger than the sample size, resulting in the inapplicability of LEFM [86].

If a material deforms plastically, LEFM is no longer applicable due to crack blunting and elastic-plastic fracture mechanics needs to be used. While in elastic-plastic fracture the K-concept is not valid anymore [86], the J-concept can be applied and is complemented by the crack tip opening displacement (CTOD) δ_t . Both are directly connected via the fracture strength σ_f [86]:

$$J_C = \sigma_f \delta_{tc} \quad (24)$$

However, these concepts are only valid if the samples are sufficiently large since the zone around the crack tip being described by the J or δ_t concept needs to be significantly larger than the plastic zone. Moreover, elastic-plastic fracture mechanics can only describe stable crack growth [86]. Hence, shear softening metallic glasses are out of the scope of this model.

2.8. Magnetometry

The magnetization of metallic glass samples is measured in a vibrating sample magnetometer. Therein, the sample and – at distance to avoid interference of the magnetic fields – a reference is oscillated in an external magnetic field. The magnetic field of the sample as response to the external magnetic field induces a voltage into detection coils that is proportional to the magnetic field of the sample [183]. Due to the comparison of the voltage induced by the sample and the voltage induced by the reference, the measurement is insensitive to the vibration amplitude and frequency as well as to instabilities and non-uniformities of the magnetic field [183].

2.9. Atom probe tomography

Atom probe tomography (APT) is used to investigate the chemical composition spatially resolved on a nano-meter scale, for example to probe the chemical heterogeneity of the samples as done in this work. In APT, a high voltage is applied between a sub-micrometre-sized sharp sample tip, which is cooled to cryogenic temperatures, and a local counter-electrode located in micrometre distance. By high voltage pulses or laser pulses surface atoms are evaporated from the tip and accelerated through the local electrode into a position sensitive

single ion detector. Based on the detector information and the time-of-flight, type and position of the ion in the tip can be reconstructed [173].

3. Summary of publications

In this section, the publications that address the research questions formulated in section 1.5 are summarized. The detailed results, discussion and methodology can be found in the attached original publications.

Paper I:

The coefficient of thermal expansion (CTE) is an important design parameter for structural applications as well as processing of metallic glasses. It is demonstrated that predictions of the coefficient of thermal expansion for metallic glasses by density functional theory-based *ab initio* calculations are efficient both with respect to time and resources. The coefficient of thermal expansion is predicted by an *ab initio* based method utilizing the Debye-Grüneisen model to be $3.4 \cdot 10^{-5} \text{ K}^{-1}$ at room temperature for a $\text{Pd}_{54.7}\text{Al}_{23.5}\text{Y}_{7.8}\text{Ni}_{11.3}$ metallic glass, which exhibits a pronounced medium-range order. The predictions are critically appraised by *in situ* synchrotron X-ray scattering and excellent agreement is observed. Through this combined theoretical and experimental research strategy, the feasibility to predict the CTE from the ground state structure of a metallic glass until the onset of structural changes is shown. Thereby, a method to efficiently probe a potentially vast number of metallic glass alloying combinations regarding thermal expansion is provided.

Paper II:

While thermal expansion is important for thermoplastic forming, for the application of metallic glasses as structural materials high fracture toughness is crucial to avoid catastrophic failure of the material in a brittle manner. One fingerprint for fracture toughness in metallic glasses is the fraction of hybridized bonds, which is in case of $\text{Pd}_{57.4}\text{Al}_{23.5}\text{Y}_{7.8}\text{M}_{11.3}$ affected by alloying with $\text{M} = \text{Fe}, \text{Ni}, \text{Co}, \text{Cu}, \text{Os}, \text{Ir}, \text{Pt}, \text{and Au}$. It is shown that experimental fracture toughness data is correlated to the fraction of hybridized bonds which scale with the localized bonds at the Fermi

level. Thus, the localized bonds at the Fermi level are utilized quantitatively as a measure for fracture toughness. Based on *ab initio* calculations, the minimum fraction of hybridized bonds was identified for $\text{Pd}_{57.4}\text{Al}_{23.5}\text{Y}_{7.8}\text{Ni}_{11.3}$. According to the ansatz that the crystal orbital overlap population at the Fermi level scales with fracture toughness, for $\text{Pd}_{57.4}\text{Al}_{23.5}\text{Y}_{7.8}\text{Ni}_{11.3}$ a value of around $95 \pm 20 \text{ MPa}\cdot\text{m}^{0.5}$ is predicted quantitatively for the first time. Consistent with this prediction, in micro-mechanical beam bending experiments $\text{Pd}_{57.4}\text{Al}_{23.5}\text{Y}_{7.8}\text{Ni}_{11.3}$ thin films show pronounced plasticity and absence of crack growth.

Paper III:

Metalloids are frequently alloyed into metallic glasses to enhance the mechanical properties [29,130,184] or the glass forming ability [21,185,186]. However, the effect of – especially large – metalloid concentrations on the electronic structure has not been investigated so far. As the behaviour of metallic glasses depends on the electronic structure which in turn is defined by chemical composition, the influence of B concentration on glass transition, topology, magnetism and bonding for B concentrations $x = 2$ to 92 at.% in the $(\text{Co}_{6.8}\text{Ta}_1)_{100-x}\text{B}_x$ system is systematically investigated. From an electronic structure and coordination point of view, the B concentration range is divided into three regions: Below 39 ± 5 at.% B, the material is a metallic glass due to the dominance of metallic bonds. Above 69 ± 6 at.% the presence of an icosahedra-like B network is observed. As the B concentration is increased above 39 ± 5 at.%, the B network evolves while the metallic coordination of the material decreases until the B concentration of 67 ± 5 at.% is reached. Hence, a composite is formed. It is evident that based on the B concentration, the ratio of metallic bonding to icosahedral bonding in the composite can be controlled. It is proposed that by tuning the coordination in the composite region, glassy materials with defined plasticity and processability can be designed.

Paper IV:

While it is accepted that the plastic behaviour of metallic glasses is affected by their free volume content, the effect thereof on chemical bonding has not been investigated systematically. According to electronic structure analysis, the overall bond strength is not

significantly affected by the free volume content. However, with increasing free volume content, the average coordination number decreases. Furthermore, the volume fraction of regions containing atoms with lower coordination number increases. As the local bonding character changes from bonding to anti-bonding with decreasing coordination number, bonding is weakened in the volume fraction of lower coordination number. During deformation, the number of strong, short-distance bonds decreases more for free volume containing samples than for samples without free volume, resulting in additional bond weakening. Thus, it is shown that the introduction of free volume causes the formation of volume fractions of lower coordination number resulting in weaker bonding and proposed that this is the electronic structure origin of the enhanced plastic behaviour reported for glasses containing free volume.

4. Contribution to the field

In this work, the Debye-Grüneisen model is proposed as a reliable *ab initio*-based method to predict the CTE of metallic glasses. Moreover, a predictor function for fracture toughness based on the correlation between the fraction of localized, anti-bonding bonds scaling with the crystal orbital overlap population at the Fermi level and experimental fracture toughness data is proposed. Both methods - to predict CTE and fracture toughness – expand the available *ab initio* predictor functions to metallic glasses. The prediction of fracture toughness is crucial to avoid catastrophic failure and the CTE has an impact on near net-shape forming. Thus, this work enables the identification of promising metallic glass compositions for structural applications and processing out of the vast metallic glass composition space fraction. Due to the here employed *ab initio* approach, this identification is efficient both with respect to time and resources.

In paper III, it is proposed that by controlling the coordination in a self-organized metallic glass – network glass Co-Ta-B composite, soft-magnetic amorphous materials with defined plasticity and processability can be designed. Thereby, an experimentally unexplored compositional space fraction is opened up which is promising in terms of mechanical properties by the combination of the beneficial mechanical properties of metallic as well as network glasses. In

addition, the coordination based composite formation may point towards the origin of self-organized nano-laminate formation in metallic glasses, which has not been explained so far.

In paper IV, bond weakening due to a local rise of anti-bonding states in volume fractions of lower coordination is proposed as the electronic structure origin of the enhanced plastic behaviour reported for free volume containing metallic glasses. Considering this free volume effect on the electronic structure enables fine-tuning of the quantum-mechanical predictor functions, yielding in a suitable composition and free volume content for the optimal performance of a metallic glass in a specific application. Simultaneously, the complexity of metallic glass synthesis increases, as not only the composition, but also the free volume content needs to be controlled. As the density is affected by the free volume content, the former is identified as a key parameter for the quantum mechanically guided design of metallic glasses.

5. Future work

Quantum mechanical methods have limitations due to the computational resources required when predicting amorphous materials on time-scales larger than femtoseconds. Simulations of atomic rearrangements during structural relaxation or investigations of shear bands and their electronic structure would require simulations with supercells in the order of μm and time scales in the order of seconds or at least milliseconds. Compared to the spatial and temporal scales used in the studies presented here, this means increasing the temporal scale by a factor of $10^9 - 10^{12}$ and the spatial scale by a factor of 10^3 in each direction. Therefore, one simulation cell would contain 10^{11} atoms, and the number of electrons is even larger. The computational time required would hence increase by a factor much larger than 10^{33} due to the cubic scaling of the computational time with electrons [187]. To avoid the drawbacks of potentials used in classical molecular dynamics, which is capable of large cell sizes, these demanding calculations need to be conducted based on linear scaling ($O(N)$) DFT algorithms [188]. $O(N)$ algorithms use the fact that electronic interactions are mainly confined to the short-range order [188] and are hence suited for short-range ordered (non-metallic) materials. However, $O(N)$

algorithms for metallic systems have been developed [188]. Next to $O(N)$ algorithms, new modelling routines for large metallic glass systems need to be developed that reduce the computational effort by identifying and focussing on the regions of interest in the supercell. The precision of the calculations is to be kept high in these regions of interest, while the precision in the rest of the simulation cell may be lowered to reduce the computational effort.

The continuous evolution of short and medium-range order in $\text{Pd}_{62.1}\text{Al}_{27.3}\text{Y}_{4.2}\text{Ni}_{6.4}$ towards the crystalline structure during heating was reported in this work based on high energy X-ray scattering. While this technique can resolve the average structural evolution, the formation of embryos for crystallization, their structure as well as competing phases has not been understood so far. To gain this understanding, the movement and evolution of the atomic structure on the atomic level needs to be tracked. As atom probe tomography in combination with field ion microscopy allows three-dimensional atomic resolution [189], the crystallization of metallic glasses can be investigated on stepwise heated samples by the combination of these techniques. Due to the beneficial effects of crystalline phases in the metallic glass matrix [113], once the mechanisms of the crystallization process in metallic glasses are understood, the design of metallic glass matrix composites with defined mechanical properties will be enabled.

Not only the metallic glass matrix composites, but also composites containing icosahedra-like network fragments as well as metallically bonded regions are promising for the design of metallic glasses with enhanced mechanical properties. However, the effect of the ratio of network fragments to metallically bonded regions on the mechanical properties as well as the effect of composition, substrate temperature and ion energy on the self-organized formation of these self-organized composites needs to be understood to design composites with tailored mechanical properties. Therefore, a systematic study on the deposition conditions combined with electron microscopy techniques that probe the local topology such as electron loss near edge fine structure spectroscopy needs to be conducted. Correlative *ab initio* calculations to determine the surface energies are required to explain the self-organized formation of these

amorphous composites. The amorphous nature of the glass, however, makes the calculation of surface energies complex since the surface of amorphous materials is not precisely defined. Hence, a routine must be developed that first identifies representative surface configurations out of the vast number of potential surfaces. Only in the second step, the surface energies can be calculated. Micro-mechanical experiments show the influence of the different composite structures on the mechanical properties.

The predictor function for fracture toughness of metallic glasses based on the number of localized states at the Fermi level, as presented here, does neglect the influence of magnetism as well as free volume. As magnetism influences the electronic states at the Fermi level [190] and the effects of magnetism on the electronic structure of metallic glasses are not systematically investigated yet, the predictor function needs to be expanded for magnetic metallic glasses based on the understanding of the electronic structure of these materials. The free volume needs also to be incorporated into the predictor functions, as the free volume is a crucial parameter for fracture toughness [43] and leads to bond weakening due to a local rise of anti-bonding states in volume fractions containing atoms of low coordination number, which are identified as free volume sites [53]. Therefore, the theoretical study on the effect of free volume on the electronic structure needs to be critically appraised by an experimental study that connects the free volume content of thin film metallic glasses measured by high energy X-ray diffraction according to Yavari *et al.* [145] with the mechanical properties. Moreover, the distribution of volume fractions containing atoms of low coordination number needs to be critically appraised by determining the free volume distribution experimentally employing fluctuation electron microscopy [191].

References

- [1] W. Klement, R.H. Willens, P.O.L. Duwez, Non-crystalline Structure in Solidified Gold–Silicon Alloys, *Nature* 187 (1960) 869–870.
- [2] H.-W. Chen, K.-C. Hsu, Y.-C. Chan, J.-G. Duh, J.-W. Lee, J.S.-C. Jang, G.-J. Chen, Antimicrobial properties of Zr–Cu–Al–Ag thin film metallic glass, *Thin Solid Films* 561 (2014) 98–101.
- [3] J.-H. Chu, J. Lee, C.-C. Chang, Y.-C. Chan, M.-L. Liou, J.-W. Lee, J.S.-C. Jang, J.-G. Duh, Antimicrobial characteristics in Cu-containing Zr-based thin film metallic glass, *Surface and Coatings Technology* 259 (2014) 87–93.
- [4] P.-T. Chiang, G.-J. Chen, S.-R. Jian, Y.-H. Shih, J.S.-C. Jang, C.-H. Lai, Surface Antimicrobial Effects of Zr₆₁Al_{7.5}Ni₁₀Cu_{17.5}Si₄ Thin Film Metallic Glasses on *Escherichia coli*, *Staphylococcus aureus*, *Pseudomonas aeruginosa*, *Acinetobacter baumannii* and *Candida albicans*, *Footprint Journal of Health Sciences* 2 (2010) 12–20.
- [5] L. Huang, E.M. Fozo, T. Zhang, P.K. Liaw, W. He, Antimicrobial behavior of Cu-bearing Zr-based bulk metallic glasses, *Materials science & engineering. C, Materials for biological applications* 39 (2014) 325–329.
- [6] Y. Liu, J. Padmanabhan, B. Cheung, J. Liu, Z. Chen, B.E. Scanley, D. Wesolowski, M. Pressley, C.C. Broadbridge, S. Altman, U.D. Schwarz, T.R. Kyriakides, J. Schroers, Combinatorial development of antibacterial Zr-Cu-Al-Ag thin film metallic glasses, *Scientific reports* 6 (2016) 26950.
- [7] Y.Y. Chu, Y.S. Lin, C.M. Chang, J.-K. Liu, C.H. Chen, J.C. Huang, Promising antimicrobial capability of thin film metallic glasses, *Materials science & engineering. C, Materials for biological applications* 36 (2014) 221–225.
- [8] J.P. Chu, J.S.C. Jang, J.C. Huang, H.S. Chou, Y. Yang, J.C. Ye, Y.C. Wang, J.W. Lee, F.X. Liu, P.K. Liaw, Y.C. Chen, C.M. Lee, C.L. Li, C. Rullyani, Thin film metallic glasses, *Thin Solid Films* 520 (2012) 5097–5122.
- [9] P. Yiu, W. Diyatmika, N. Bönninghoff, Y.-C. Lu, B.-Z. Lai, J.P. Chu, Thin film metallic glasses, *Journal of Applied Physics* 127 (2020) 30901.

- [10] Z. Parlar, M. Bakkal, A.J. Shih, Sliding tribological characteristics of Zr-based bulk metallic glass, *Intermetallics* 16 (2008) 34–41.
- [11] J. Bhatt, S. Kumar, C. Dong, B.S. Murty, Tribological behaviour of Cu₆₀Zr₃₀Ti₁₀ bulk metallic glass, *Materials Science and Engineering: A* 458 (2007) 290–294.
- [12] A. Baiker, Metallic glasses in heterogeneous catalysis, *Faraday Discuss. Chem. Soc.* 87 (1989) 239.
- [13] M. Zhao, K. Abe, S.-i. Yamaura, Y. Yamamoto, N. Asao, Fabrication of Pd–Ni–P Metallic Glass Nanoparticles and Their Application as Highly Durable Catalysts in Methanol Electro-oxidation, *Chem. Mater.* 26 (2013) 1056–1061.
- [14] Y.C. Hu, Y.Z. Wang, R. Su, C.R. Cao, F. Li, C.W. Sun, Y. Yang, P.F. Guan, D.W. Ding, Z.L. Wang, W.H. Wang, A Highly Efficient and Self-Stabilizing Metallic-Glass Catalyst for Electrochemical Hydrogen Generation, *Advanced materials (Deerfield Beach, Fla.)* 28 (2016) 10293–10297.
- [15] Z. Jia, X. Duan, P. Qin, W. Zhang, W. Wang, C. Yang, H. Sun, S. Wang, L.-C. Zhang, Disordered Atomic Packing Structure of Metallic Glass, *Adv. Funct. Mater.* 27 (2017) 1702258.
- [16] V. Hasannaemi, S. Mukherjee, Noble-Metal based Metallic Glasses as Highly Catalytic Materials for Hydrogen Oxidation Reaction in Fuel Cells, *Scientific reports* 9 (2019) 12136.
- [17] M. Ashby, A.L. Greer, Metallic glasses as structural materials, *Scripta Mater.* 54 (2006) 321–326.
- [18] A.L. Greer, Metallic glasses... on the threshold, *Mater. Today* 12 (2009) 14–22.
- [19] G. Kumar, A. Desai, J. Schroers, Bulk metallic glass: the smaller the better, *Adv. Mater.* 23 (2011) 461–476.
- [20] M. Telford, The case for bulk metallic glass, *Mater. Today* 7 (2004) 36–43.
- [21] A. Inoue, B. Shen, A. Takeuchi, Developments and Applications of Bulk Glassy Alloys in Late Transition Metal Base System, *Mater. Trans.* 47 (2006) 1275–1285.

- [22] T. Egami, T. Iwashita, W. Dmowski, Mechanical Properties of Metallic Glasses, *Metals* 3 (2013) 77–113.
- [23] R.O. Ritchie, The conflicts between strength and toughness, *Nat. Mater.* 10 (2011) 817–822.
- [24] J. Xu, U. Ramamurty, E. Ma, The fracture toughness of bulk metallic glasses, *JOM* 62 (2010) 10–18.
- [25] C.A. Schuh, T.C. Hufnagel, U. Ramamurty, Mechanical behavior of amorphous alloys, *Acta Mater.* 55 (2007) 4067–4109.
- [26] J.J. Gilman, Mechanical behavior of metallic glasses, *Journal of Applied Physics* 46 (1975) 1625–1633.
- [27] B.A. Sun, W.H. Wang, The fracture of bulk metallic glasses, *Prog. Mater. Sci.* 74 (2015) 211–307.
- [28] E.S. Park, D.H. Kim, Design of Bulk metallic glasses with high glass forming ability and enhancement of plasticity in metallic glass matrix composites, *Met. Mater. Int.* 11 (2005) 19–27.
- [29] A. Inoue, B.L. Shen, H. Koshiba, H. Kato, A.R. Yavari, Ultra-high strength above 5000 MPa and soft magnetic properties of Co-Fe-Ta-B bulk glassy alloys, *Acta Mater.* 52 (2004) 1631–1637.
- [30] A. Inoue, X.M. Wang, W. Zhang, Developments and applications of bulk metallic glasses, *Rev. Adv. Mater. Sci.* 18 (2008) 1–9.
- [31] M.D. Demetriou, M.E. Launey, G. Garrett, J.P. Schramm, D.C. Hofmann, W.L. Johnson, R.O. Ritchie, A damage-tolerant glass, *Nat. Mater.* 10 (2011) 123–128.
- [32] J.J. Gilman, Metallic glasses, *Science (New York, N.Y.)* 208 (1980) 856–861.
- [33] J. Zarzycki, W.D. Scott, C. Massart, *Glasses and the vitreous state*, Cambridge University Press, Cambridge, 1991.
- [34] A. Inoue, Stabilization of metallic supercooled liquid and bulk amorphous alloys, *Acta Mater.* 48 (2000) 279–306.

- [35] Z. Liu, K.C. Chan, L. Liu, Enhanced glass forming ability and plasticity of a Ni-free Zr-based bulk metallic glass, *Journal of Alloys and Compounds* 487 (2009) 152–156.
- [36] T. Abe, M. Shimono, K. Hashimoto, K. Hono, H. Onodera, Phase separation and glass-forming abilities of ternary alloys, *Scripta Materialia* 55 (2006) 421–424.
- [37] T.W. Barbee, W.H. Holmes, D.L. Keith, M.K. Pyszyna, G. Ilonca, Synthesis of amorphous niobium-nickel alloys by vapor quenching, *Thin Solid Films* 45 (1977) 591–599.
- [38] H.A. Davies, The formation of metallic glasses, *Phys. Chem. Glasses* 17 (1976) 159–173.
- [39] F.H. Stillinger, A topographic view of supercooled liquids and glass formation, *Science* (New York, N.Y.) 267 (1995) 1935–1939.
- [40] P.G. Debenedetti, F.H. Stillinger, Supercooled liquids and the glass transition, *Nature* 410 (2001) 259–267.
- [41] J.C. Qiao, J.M. Pelletier, Dynamic Mechanical Relaxation in Bulk Metallic Glasses, *J. Mater. Sci. Technol.* 30 (2014) 523–545.
- [42] T. Egami, Structural Relaxation in Metallic Glasses, *Ann. NY. Acad. Sci.* 371 (1981) 238–251.
- [43] Y. Sun, A. Concustell, A.L. Greer, Thermomechanical processing of metallic glasses, *Nat. Rev. Mater.* 1 (2016) 16039.
- [44] L. Berthier, M. Ozawa, C. Scalliet, Configurational entropy of glass-forming liquids, *The Journal of chemical physics* 150 (2019) 160902.
- [45] P.K. Gupta, J.C. Mauro, Composition dependence of glass transition temperature and fragility. I. A topological model incorporating temperature-dependent constraints, *The Journal of chemical physics* 130 (2009) 94503.
- [46] Y.Q. Cheng, E. Ma, Atomic-level structure and structure–property relationship in metallic glasses, *Prog. Mater. Sci.* 56 (2011) 379–473.
- [47] O. Haruyama, H.M. Kimura, N. Nishiyama, A. Inoue, Isothermal Relaxation Behavior in a $\text{Pd}_{42.5}\text{Cu}_{30}\text{Ni}_{7.5}\text{P}_{20}$ Metallic Glass, *Mater. Trans.* 45 (2004) 1184–1188.

- [48] G. Kumar, D. Rector, R.D. Conner, J. Schroers, Embrittlement of Zr-based bulk metallic glasses, *Acta Mater.* 57 (2009) 3572–3583.
- [49] J. Pan, Y.P. Ivanov, W.H. Zhou, Y. Li, A.L. Greer, Strain-hardening and suppression of shear-banding in rejuvenated bulk metallic glass, *Nature* 578 (2020) 559–562.
- [50] A.L. Greer, Y.Q. Cheng, E. Ma, Shear bands in metallic glasses, *Mat. Sci. Eng. R* 74 (2013) 71–132.
- [51] N. Li, L. Liu, Q. Chen, J. Pan, K.C. Chan, The effect of free volume on the deformation behaviour of a Zr-based metallic glass under nanoindentation, *J. Phys. D: Appl. Phys.* 40 (2007) 6055–6059.
- [52] G. Gottstein, *Physikalische Grundlagen der Materialkunde: Mit 28 Tabellen*, 3rd ed., Springer, Berlin, Heidelberg, New York, 2007.
- [53] A.S. Argon, Plastic deformation in metallic glasses, *Acta Metall.* 27 (1979) 47–58.
- [54] F. Spaepen, A microscopic mechanism for steady state inhomogeneous flow in metallic glasses, *Acta Metall.* 25 (1977) 407–415.
- [55] Z.F. Zhang, J. Eckert, L. Schultz, Difference in compressive and tensile fracture mechanisms of Zr₅₉Cu₂₀Al₁₀Ni₈Ti₃ bulk metallic glass, *Acta Materialia* 51 (2003) 1167–1179.
- [56] F. Spaepen, Homogeneous flow of metallic glasses, *Scripta Mater.* 54 (2006) 363–367.
- [57] W.H. Wang, Y. Yang, T.G. Nieh, C.T. Liu, On the source of plastic flow in metallic glasses, *Intermetallics* 67 (2015) 81–86.
- [58] H. Guo, P.F. Yan, Y.B. Wang, J. Tan, Z.F. Zhang, M.L. Sui, E. Ma, Tensile ductility and necking of metallic glass, *Nat. Mater.* 6 (2007) 735–739.
- [59] C.-C. Yu, C.M. Lee, J.P. Chu, J.E. Greene, P.K. Liaw, Fracture-resistant thin-film metallic glass, *APL Materials* 4 (2016) 116101.
- [60] J.G. Wang, D.Q. Zhao, M.X. Pan, W.H. Wang, S.X. Song, T.G. Nieh, Correlation between onset of yielding and free volume in metallic glasses, *Scripta Materialia* 62 (2010) 477–480.

- [61] A.J. Cao, Y.Q. Cheng, E. Ma, Structural processes that initiate shear localization in metallic glass, *Acta Mater.* 57 (2009) 5146–5155.
- [62] N. Thurieau, L. Perrière, M. Laurent-Brocq, Y. Champion, Activation volume in heterogeneous deformation of Mg₆₅Cu_{12.5}Ni_{12.5}(Ce₇₅La₂₅)₁₀ metallic glass, *Journal of Applied Physics* 118 (2015) 204302.
- [63] S.T. Liu, Z. Wang, H.L. Peng, H.B. Yu, W.H. Wang, The activation energy and volume of flow units of metallic glasses, *Scripta Materialia* 67 (2012) 9–12.
- [64] J.H. Perepezko, S.D. Imhoff, M.-W. Chen, J.-Q. Wang, S. Gonzalez, Nucleation of shear bands in amorphous alloys, *Proceedings of the National Academy of Sciences of the United States of America* 111 (2014) 3938–3942.
- [65] T.C. Hufnagel, C.A. Schuh, M.L. Falk, Deformation of metallic glasses, *Acta Mater.* 109 (2016) 375–393.
- [66] Z.-D. Sha, Q.-X. Pei, V. Sorkin, P.S. Branicio, Y.-W. Zhang, H. Gao, On the notch sensitivity of CuZr metallic glasses, *Appl. Phys. Lett.* 103 (2013) 81903.
- [67] T.C. Hufnagel, P. El-Deiry, R.P. Vinci, Development of shear band structure during deformation of a Zr₅₇Ti₅Cu₂₀Ni₈Al₁₀ bulk metallic glass, *Scripta Mater.* 43 (2000) 1071–1075.
- [68] X.K. Xi, D.Q. Zhao, M.X. Pan, W.H. Wang, Y. Wu, J.J. Lewandowski, Fracture of brittle metallic glasses: brittleness or plasticity, *Phys. Rev. Lett.* 94 (2005) 125510.
- [69] R. Narasimhan, P. Tandaiya, I. Singh, R.L. Narayan, U. Ramamurty, Fracture in metallic glasses, *Int J Fract* 191 (2015) 53–75.
- [70] B.A. Sun, H.B. Yu, W. Jiao, H.Y. Bai, D.Q. Zhao, W.H. Wang, Plasticity of ductile metallic glasses, *Phys. Rev. Lett.* 105 (2010) 35501.
- [71] G.N. Yang, Y. Shao, K.F. Yao, The shear band controlled deformation in metallic glass, *Sci. Rep.* 6 (2016) 21852.
- [72] H. Bei, S. Xie, E.P. George, Softening caused by profuse shear banding in a bulk metallic glass, *Phys. Rev. Lett.* 96 (2006) 105503.

- [73] S. Evertz, I. Kirchlechner, R. Soler, C. Kirchlechner, P. Kontis, J. Bednarcik, B. Gault, G. Dehm, D. Raabe, J.M. Schneider, Electronic structure based design of thin film metallic glasses with superior fracture toughness, *Materials & Design* 186 (2020) 108327.
- [74] R.D. Conner, W.L. Johnson, N.E. Paton, W.D. Nix, Shear bands and cracking of metallic glass plates in bending, *J. Appl. Phys.* 94 (2003) 904–911.
- [75] F.F. Wu, W. Zheng, S.D. Wu, Z.F. Zhang, J. Shen, Shear stability of metallic glasses, *International Journal of Plasticity* 27 (2011) 560–575.
- [76] R.L. Narayan, P. Tandaiya, G.R. Garrett, M.D. Demetriou, U. Ramamurty, On the variability in fracture toughness of ‘ductile’ bulk metallic glasses, *Scripta Mater.* 102 (2015) 75–78.
- [77] J. Schroers, W.L. Johnson, Ductile bulk metallic glass, *Phys. Rev. Lett.* 93 (2004) 255506.
- [78] Q. He, Y.-Q. Cheng, E. Ma, J. Xu, Locating bulk metallic glasses with high fracture toughness, *Acta Mater.* 59 (2011) 202–215.
- [79] W. Chen, J. Ketkaew, Z. Liu, R.M.O. Mota, K. O’Brien, C.S. da Silva, J. Schroers, Does the fracture toughness of bulk metallic glasses scatter?, *Scripta Mater.* 107 (2015) 1–4.
- [80] M. Ghidelli, S. Gravier, J.-J. Blandin, P. Djemia, F. Momprou, G. Abadias, J.-P. Raskin, T. Pardoen, Extrinsic mechanical size effects in thin ZrNi metallic glass films, *Acta Mater.* 90 (2015) 232–241.
- [81] B. Gludovatz, D. Granata, K.V.S. Thurston, J.F. Löffler, R.O. Ritchie, On the understanding of the effects of sample size on the variability in fracture toughness of bulk metallic glasses, *Acta Mater.* 126 (2017) 494–506.
- [82] X.J. Gu, S.J. Poon, G.J. Shiflet, J.J. Lewandowski, Compressive plasticity and toughness of a Ti-based bulk metallic glass, *Acta Mater.* 58 (2010) 1708–1720.
- [83] A. Kawashima, H. Kurishita, H. Kimura, T. Zhang, A. Inoue, Fracture Toughness of Zr₅₅Al₁₀Ni₅Cu₃₀ Bulk Metallic Glass by 3-Point Bend Testing, *Mater. Trans., JIM* 46 (2005) 1725–1732.

- [84] B. Gludovatz, S.E. Naleway, R.O. Ritchie, J.J. Kruzic, Size-dependent fracture toughness of bulk metallic glasses, *Acta Mater.* 70 (2014) 198–207.
- [85] D. Geissler, J. Freudenberger, H. Wendrock, M. Zimmermann, A. Gebert, On sample size effects in fracture toughness determination of Bulk Metallic Glasses, *Eng. Fract. Mech.* 202 (2018) 500–507.
- [86] D. Gross, T. Seelig, *Bruchmechanik*, Springer Berlin Heidelberg, Berlin, Heidelberg, 2016.
- [87] T. Rouxel, Fracture surface energy and toughness of inorganic glasses, *Scripta Mater.* 137 (2017) 109–113.
- [88] Q. An, K. Samwer, M.D. Demetriou, M.C. Floyd, D.O. Duggins, W.L. Johnson, W.A. Goddard, How the toughness in metallic glasses depends on topological and chemical heterogeneity, *Proceedings of the National Academy of Sciences of the United States of America* 113 (2016) 7053–7058.
- [89] A. Shamimi Nouri, X.J. Gu, S.J. Poon, G.J. Shiflet, J.J. Lewandowski, Chemistry (intrinsic) and inclusion (extrinsic) effects on the toughness and Weibull modulus of Fe-based bulk metallic glasses, *Phil. Mag. Lett.* 88 (2008) 853–861.
- [90] J.J. Lewandowski, W.H. Wang, A.L. Greer, Intrinsic plasticity or brittleness of metallic glasses, *Phil. Mag. Lett.* 85 (2005) 77–87.
- [91] G.N. Greaves, A.L. Greer, R.S. Lakes, T. Rouxel, Poisson's ratio and modern materials, *Nat. Mater.* 10 (2011) 823–837.
- [92] J.J. Lewandowski, M. Shazly, A. Shamimi Nouri, Intrinsic and extrinsic toughening of metallic glasses, *Scripta Mater.* 54 (2006) 337–341.
- [93] V. Schnabel, B.N. Jaya, M. Kohler, D. Music, C. Kirchlechner, G. Dehm, D. Raabe, J.M. Schneider, Electronic hybridisation implications for the damage-tolerance of thin film metallic glasses, *Sci. Rep.* 6 (2016) 36556.
- [94] R. Raghavan, P. Murali, U. Ramamurty, On factors influencing the ductile-to-brittle transition in a bulk metallic glass, *Acta Mater.* 57 (2009) 3332–3340.

- [95] G. Kumar, S. Prades-Rodel, A. Blatter, J. Schroers, Unusual brittle behavior of Pd-based bulk metallic glass, *Scripta Mater.* 65 (2011) 585–587.
- [96] Z.-d. Zhu, P. Jia, J. Xu, Optimization for toughness in metalloid-free Ni-based bulk metallic glasses, *Scripta Mater.* 64 (2011) 785–788.
- [97] P. Jia, Z.-d. Zhu, E. Ma, J. Xu, Notch toughness of Cu-based bulk metallic glasses, *Scripta Mater.* 61 (2009) 137–140.
- [98] J. Yi, W.H. Wang, J.J. Lewandowski, Guiding and Deflecting Cracks in Bulk Metallic Glasses to Increase Damage Tolerance, *Adv. Eng. Mater.* 17 (2015) 620–625.
- [99] G.P. Zhang, Y. Liu, B. Zhang, Effect of annealing close to T_g on notch fracture toughness of Pd-based thin-film metallic glass for MEMS applications, *Scripta Mater.* 54 (2006) 897–901.
- [100] C.J. Gilbert, R.O. Ritchie, W.L. Johnson, Fracture toughness and fatigue-crack propagation in a Zr–Ti–Ni–Cu–Be bulk metallic glass, *Appl. Phys. Lett.* 71 (1997) 476–478.
- [101] M.E. Launey, R.O. Ritchie, On the Fracture Toughness of Advanced Materials, *Adv. Mater.* 21 (2009) 2103–2110.
- [102] S.G. Zhang, Signature of properties in elastic constants of no-metalloid bulk metallic glasses, *Intermetallics* 35 (2013) 1–8.
- [103] L.A. Davis, Y.T. Yeow, P.M. Anderson, Bulk stiffnesses of metallic glasses, *J. Appl. Phys.* 53 (1982) 4834–4837.
- [104] J.J. Gilman, *Electronic basis of the strength of materials*, Cambridge University Press, Cambridge, 2008.
- [105] Y. Wu, H. Wang, Y. Cheng, X. Liu, X. Hui, T. Nieh, Y. Wang, Z. Lu, Inherent structure length in metallic glasses, *Sci. Rep.* 5 (2015) 12137.
- [106] W. Zhao, J.L. Cheng, S.D. Feng, G. Li, R.P. Liu, Intrinsic correlation between elastic modulus and atomic bond stiffness in metallic glasses, *Materials Letters* 175 (2016) 227–230.

- [107] Y.Q. Cheng, E. Ma, Configurational dependence of elastic modulus of metallic glass, *Phys. Rev. B* 80 (2009) 611.
- [108] L.A. Davis, C.-P. Chou, L.E. Tanner, R. Ray, Strengths and stiffnesses of metallic glasses, *Scripta Metallurgica* 10 (1976) 937–940.
- [109] J.J. Pang, M.J. Tan, K.M. Liew, On valence electron density, energy dissipation and plasticity of bulk metallic glasses, *J. Alloy. Compd.* 577 (2013) S56-S65.
- [110] V. Schnabel, M. Köhler, D. Music, J. Bednarcik, W.J. Clegg, D. Raabe, J.M. Schneider, Ultra-stiff metallic glasses through bond energy density design, *J. Phys. Condens. Mat.* 29 (2017) 265502.
- [111] R. Dronskowski, P.E. Bloechl, Crystal orbital Hamilton populations (COHP), *J. Phys. Chem.* 97 (1993) 8617–8624.
- [112] D.C. Hofmann, J.-Y. Suh, A. Wiest, G. Duan, M.-L. Lind, M.D. Demetriou, W.L. Johnson, Designing metallic glass matrix composites with high toughness and tensile ductility, *Nature* 451 (2008) 1085–1089.
- [113] J. Eckert, J. Das, S. Pauly, C. Duhamel, Mechanical properties of bulk metallic glasses and composites, *J. Mater. Res.* 22 (2007) 285–301.
- [114] Y.-K. Xu, H. Ma, J. Xu, E. Ma, Mg-based bulk metallic glass composites with plasticity and gigapascal strength, *Acta Materialia* 53 (2005) 1857–1866.
- [115] H. Choi-Yim, W.L. Johnson, Bulk metallic glass matrix composites, *Appl. Phys. Lett.* 71 (1997) 3808–3810.
- [116] J. Qiao, H. Jia, P.K. Liaw, Metallic glass matrix composites, *Materials Science and Engineering: R: Reports* 100 (2016) 1–69.
- [117] M. Calin, J. Eckert, L. Schultz, Improved mechanical behavior of Cu–Ti-based bulk metallic glass by in situ formation of nanoscale precipitates, *Scripta Mater.* 48 (2003) 653–658.
- [118] G. He, J. Eckert, W. Löser, L. Schultz, Novel Ti-base nanostructure-dendrite composite with enhanced plasticity, *Nature Materials* 2 (2003) 33–37.

- [119] U. Kühn, J. Eckert, N. Mattern, L. Schultz, ZrNbCuNiAl bulk metallic glass matrix composites containing dendritic bcc phase precipitates, *Appl. Phys. Lett.* 80 (2002) 2478–2480.
- [120] E. Pekarskaya, C.P. Kim, W.L. Johnson, In situ transmission electron microscopy studies of shear bands in a bulk metallic glass based composite, *J. Mater. Res.* 16 (2001) 2513–2518.
- [121] C. Fan, R.T. Ott, T.C. Hufnagel, Metallic glass matrix composite with precipitated ductile reinforcement, *Appl. Phys. Lett.* 81 (2002) 1020–1022.
- [122] Hays, Kim, Johnson, Microstructure controlled shear band pattern formation and enhanced plasticity of bulk metallic glasses containing in situ formed ductile phase dendrite dispersions, *Phys. Rev. Lett.* 84 (2000) 2901–2904.
- [123] Y. Wu, H. Wang, H.H. Wu, Z.Y. Zhang, X.D. Hui, G.L. Chen, D. Ma, X.L. Wang, Z.P. Lu, Formation of Cu–Zr–Al bulk metallic glass composites with improved tensile properties, *Acta Materialia* 59 (2011) 2928–2936.
- [124] B. Sarac, J. Schroers, Designing tensile ductility in metallic glasses, *Nature communications* 4 (2013) 2158.
- [125] Y. Wang, J. Li, A.V. Hamza, T.W. Barbee, Ductile crystalline-amorphous nanolaminates, *Proceedings of the National Academy of Sciences of the United States of America* 104 (2007) 11155–11160.
- [126] B.J. Park, H.J. Chang, D.H. Kim, W.T. Kim, K. Chattopadhyay, T.A. Abinandanan, S. Bhattacharyya, Phase separating bulk metallic glass: a hierarchical composite, *Physical review letters* 96 (2006) 245503.
- [127] J.C. Oh, T. Ohkubo, Y.C. Kim, E. Fleury, K. Hono, Phase separation in Cu₄₃Zr₄₃Al₇Ag₇ bulk metallic glass, *Scripta Materialia* 53 (2005) 165–169.
- [128] H. Gleiter, Nanoglasses: a new kind of noncrystalline materials, *Beilstein J. Nanotechnol.* 4 (2013) 517–533.
- [129] X.L. Wang, F. Jiang, H. Hahn, J. Li, H. Gleiter, J. Sun, J.X. Fang, Plasticity of a scandium-based nanoglass, *Scripta Materialia* 98 (2015) 40–43.

- [130] P. Kontis, M. Köhler, S. Evertz, Y.-T. Chen, V. Schnabel, R. Soler, J. Bednarick, C. Kirchlechner, G. Dehm, D. Raabe, J.M. Schneider, B. Gault, Nano-laminated thin film metallic glass design for outstanding mechanical properties, *Scripta Mater.* 155 (2018) 73–77.
- [131] P. Söderlind, L. Nordström, L. Yongming, B. Johansson, Relativistic effects on the thermal expansion of the actinide elements, *Phys. Rev. B* 42 (1990) 4544–4552.
- [132] X. Lu, M. Selleby, B. Sundman, Theoretical modeling of molar volume and thermal expansion, *Acta Mater.* 53 (2005) 2259–2272.
- [133] X.-G. Lu, M. Selleby, B. Sundman, Calculations of thermophysical properties of cubic carbides and nitrides using the Debye–Grüneisen model, *Acta Mater.* 55 (2007) 1215–1226.
- [134] V.L. Moruzzi, J.F. Janak, K. Schwarz, Calculated thermal properties of metals, *Phys. Rev. B* 37 (1988) 790–799.
- [135] X. Tao, Y. Ouyang, H. Liu, F. Zeng, Y. Feng, Y. Du, Z. Jin, Ab initio calculation of the total energy and elastic properties of Laves phase $C_{15}Al_2RE$ ($RE=Sc, Y, La, Ce-Lu$), *Comp. Mater. Sci.* 44 (2008) 392–399.
- [136] E. Deligoz, H.B. Ozisik, K. Colakoglu, Y.O. Ciftci, First principles prediction of structural stability, elastic, lattice dynamical and thermal properties of osmium carbides, *Mater. Sci. Tech.* 30 (2014) 842–849.
- [137] D. Music, R.W. Geyer, P. Keuter, Thermomechanical response of thermoelectrics, *Appl. Phys. Lett.* 109 (2016) 223903.
- [138] R. Hoffmann, How Chemistry and Physics Meet in the Solid State, *Angew. Chem. Int. Ed. Engl.* 26 (1987) 846–878.
- [139] O. Hunold, D. Music, J.M. Schneider, Theoretical study of phase stability and elastic properties of $T_{0.75}Y_{0.75}B_{14}$ ($T = Sc, Ti, V, Y, Zr, Nb, Si$), *J. Phys. Condens. Mat.* 28 (2016) 105501.
- [140] O. Hunold, P. Keuter, P. Bliem, D. Music, F. Wittmers, A.L. Ravensburg, D. Primetzhofer, J.M. Schneider, Elastic properties of amorphous $T_{0.75}Y_{0.75}B_{14}$ ($T =$

- Sc, Ti, V, Y, Zr, Nb) and the effect of O incorporation on bonding, density and elasticity (T' = Ti, Zr), *J. Phys. Condens. Mat.* 29 (2017) 85404.
- [141] M. Stock, P. Molian, Femtosecond pulsed laser deposition of amorphous, ultrahard boride thin films, *J. Vac. Sci. Technol. A* 22 (2004) 670.
- [142] A. Slipenyuk, J. Eckert, Correlation between enthalpy change and free volume reduction during structural relaxation of Zr₅₅Cu₃₀Al₁₀Ni₅ metallic glass, *Scripta Materialia* 50 (2004) 39–44.
- [143] O. Haruyama, Y. Nakayama, R. Wada, H. Tokunaga, J. Okada, T. Ishikawa, Y. Yokoyama, Volume and enthalpy relaxation in Zr₅₅Cu₃₀Ni₅Al₁₀ bulk metallic glass, *Acta Mater.* 58 (2010) 1829–1836.
- [144] Z. Evenson, R. Busch, Equilibrium viscosity, enthalpy recovery and free volume relaxation in a Zr₄₄Ti₁₁Ni₁₀Cu₁₀Be₂₅ bulk metallic glass, *Acta Mater.* 59 (2011) 4404–4415.
- [145] A.R. Yavari, A. Le Moulec, A. Inoue, N. Nishiyama, N. Lupu, E. Matsubara, W.J. Botta, G. Vaughan, M. Di Michiel, Å. Kvik, Excess free volume in metallic glasses measured by X-ray diffraction, *Acta Mater.* 53 (2005) 1611–1619.
- [146] C. Fan, C.T. Liu, G. Chen, P.K. Liaw, Quantitatively defining free-volume, interconnecting-zone and cluster in metallic glasses, *Intermetallics* 57 (2015) 98–100.
- [147] J.C. Ye, J. Lu, C.T. Liu, Q. Wang, Y. Yang, Atomistic free-volume zones and inelastic deformation of metallic glasses, *Nature Materials* 9 (2010) 619–623.
- [148] P. Hohenberg, W. Kohn, Inhomogeneous Electron Gas, *Phys. Rev.* 136 (1964) B864–B871.
- [149] K. Burke, L.O. Wagner, DFT in a nutshell, *Int. J. Quantum Chem.* 113 (2013) 96–101.
- [150] K. Burke, *The ABC of DFT*, Irvine, 2007.
- [151] Perdew, Wang, Accurate and simple analytic representation of the electron-gas correlation energy, *Phys. Rev. B* 45 (1992) 13244–13249.
- [152] J.P. Perdew, K. Burke, M. Ernzerhof, Generalized Gradient Approximation Made Simple, *Phys. Rev. Lett.* 77 (1996) 3865–3868.

- [153] L. Verlet, Computer "Experiments" on Classical Fluids. I. Thermodynamical Properties of Lennard-Jones Molecules, *Phys. Rev.* 159 (1967) 98–103.
- [154] T. Ozaki, H. Kino, Numerical atomic basis orbitals from H to Kr, *Phys. Rev. B* 69 (2004) 195113.
- [155] T. Ozaki, H. Kino, Efficient projector expansion for the ab initio LCAO method, *Phys. Rev. B* 72 (2005) 45121.
- [156] L.V. Woodcock, Isothermal molecular dynamics calculations for liquid salts, *Chemical Physics Letters* 10 (1971) 257–261.
- [157] Hoover, Canonical dynamics: Equilibrium phase-space distributions, *Physical review. A, General physics* 31 (1985) 1695–1697.
- [158] C. Hostert, D. Music, J. Bednarcik, J. Keckes, V. Kapaklis, B. Hjorvarsson, J.M. Schneider, Ab initio molecular dynamics model for density, elastic properties and short range order of Co-Fe-Ta-B metallic glass thin films, *J. Phys. Condens. Mat.* 23 (2011) 475401.
- [159] F. Birch, Finite strain isotherm and velocities for single-crystal and polycrystalline NaCl at high pressures and 300°K, *J. Geophys. Res.* 83 (1978) 1257.
- [160] D. Music, T. Takahashi, L. Vitos, C. Asker, I.A. Abrikosov, J.M. Schneider, Elastic properties of Fe–Mn random alloys studied by ab initio calculations, *Appl. Phys. Lett.* 91 (2007) 191904.
- [161] T. Egami, S.J.L. Billinge, *Underneath the Bragg peaks: Structural analysis of complex materials*, 2nd ed., Elsevier, Amsterdam, 2012.
- [162] W.A. Harrison, *Electronic Structure and the Properties of Solids: The Physics of the Chemical Bond*, Dover Publications, 2012.
- [163] S. Maintz, V.L. Deringer, A.L. Tchougréeff, R. Dronskowski, Analytic projection from plane-wave and PAW wavefunctions and application to chemical-bonding analysis in solids, *J. Comput. Chem.* 34 (2013) 2557–2567.
- [164] G. Kresse, J. Furthmüller, Efficient iterative schemes for ab initio total-energy calculations using a plane-wave basis set, *Phys. Rev. B* 54 (1996) 11169–11186.

- [165] G. Kresse, D. Joubert, From ultrasoft pseudopotentials to the projector augmented-wave method, *Phys. Rev. B* 59 (1999) 1758–1775.
- [166] S. Maintz, V.L. Deringer, A.L. Tchougréeff, R. Dronskowski, LOBSTER, *J. Comput. Chem.* 37 (2016) 1030–1035.
- [167] E.D. McClanahan, N. Laegreid, Production of Thin Films by Controlled Deposition of Sputtered Material, in: R. Behrisch, K. Wittmaack (Eds.), *Sputtering by Particle Bombardment III: Characteristics of Sputtered Particles, Technical Applications*, Springer, Berlin, Heidelberg, 1991.
- [168] J.T. Gudmundsson, D. Lundin, 1 - Introduction to magnetron sputtering, in: D. Lundin, T. Minea, J.T. Gudmundsson (Eds.), *High power impulse magnetron sputtering: Fundamentals, technologies, challenges and applications*, Elsevier, 2020, pp. 1–48.
- [169] M.A. Lieberman, A.J. Lichtenberg, *Principles of plasma discharges and materials processing*, Wiley, New York, NY, 1994.
- [170] M. Rausch, S. Mráz, P. Kreiml, M.J. Cordill, J.M. Schneider, J. Winkler, C. Mitterer, Angular resolved mass-energy analysis of species emitted from a dc magnetron sputtered NiW-target, *Journal of Vacuum Science & Technology A: Vacuum, Surfaces, and Films* 38 (2020) 23401.
- [171] V. Schnabel, M. Köhler, S. Evertz, J. Gamcova, J. Bednarcik, D. Music, D. Raabe, J.M. Schneider, Revealing the relationships between chemistry, topology and stiffness of ultrastrong Co-based metallic glass thin films, *Acta Mater.* 107 (2016) 213–219.
- [172] A. Abdulkadhim, M.t. Baben, T. Takahashi, V. Schnabel, M. Hans, C. Polzer, P. Polcik, J.M. Schneider, Crystallization kinetics of amorphous Cr₂AlC thin films, *Surf. Coat. Tech.* 206 (2011) 599–603.
- [173] G. Friedbacher, H. Bubert (Eds.), *Surface and thin film analysis: A compendium of principles, instrumentation, and applications*, 2nd ed., Wiley-VCH, Weinheim, op. 2011.
- [174] A. Thompson, D. Attwood, E. Gullikson, M. Howells, K.-J. Kim, J. Kirz, J. Kortright, I. Lindau, Y. Liu, P. Pianetta, A. Robinson, J. Scofield, J. Underwood, G. Williams, H. Winick, *X-Ray Data Booklet*, Berkeley, 2009.

- [175] M. Hans, J.M. Schneider, On the chemical composition of TiAlN thin films - Comparison of ion beam analysis and laser-assisted atom probe tomography with varying laser pulse energy, *Thin Solid Films* 688 (2019) 137251.
- [176] Y. Zhang, H.J. Whitlow, T. Winzell, I.F. Bubb, T. Sajavaara, K. Arstila, J. Keinonen, Detection efficiency of time-of-flight energy elastic recoil detection analysis systems, *Nuclear Instruments and Methods in Physics Research Section B: Beam Interactions with Materials and Atoms* 149 (1999) 477–489.
- [177] P. Ström, P. Petersson, M. Rubel, G. Possnert, A combined segmented anode gas ionization chamber and time-of-flight detector for heavy ion elastic recoil detection analysis, *The Review of scientific instruments* 87 (2016) 103303.
- [178] M.S. Janson, CONTES Instruction Manual, Uppsala University, Uppsala, Sweden, 2004.
- [179] M. to Baben, M. Hans, D. Primetzhofer, S. Evertz, H. Ruess, J.M. Schneider, Unprecedented thermal stability of inherently metastable titanium aluminum nitride by point defect engineering, *Mater. Res. Lett.* (2016) 1–12.
- [180] A.-C. Dippel, H.-P. Liermann, J.T. Delitz, P. Walter, H. Schulte-Schrepping, O.H. Seeck, H. Franz, Beamline P02.1 at PETRA III for high-resolution and high-energy powder diffraction, *J. Synchrotron. Radiat.* 22 (2015) 675–687.
- [181] S. Hüfner, *Photoelectron spectroscopy: Principles and applications ; with 28 tables*, 3rd ed., Springer, Berlin, 2003.
- [182] K. Matoy, H. Schönherr, T. Detzel, T. Schöberl, R. Pippan, C. Motz, G. Dehm, A comparative micro-cantilever study of the mechanical behavior of silicon based passivation films, *Thin Solid Films* 518 (2009) 247–256.
- [183] S. Foner, Versatile and Sensitive Vibrating-Sample Magnetometer, *Review of Scientific Instruments* 30 (1959) 548–557.
- [184] J. Wang, R. Li, N. Hua, T. Zhang, Co-based ternary bulk metallic glasses with ultrahigh strength and plasticity, *J. Mater. Res.* 26 (2011) 2072–2079.

- [185] T.D. Shen, R.B. Schwarz, Bulk ferromagnetic glasses prepared by flux melting and water quenching, *Appl. Phys. Lett.* 75 (1999) 49–51.
- [186] Y. Wu, X.D. Hui, Z.P. Lu, Z.Y. Liu, L. Liang, G.L. Chen, Effects of metalloid elements on the glass-forming ability of Fe-based alloys, *J. Alloy. Compd.* 467 (2009) 187–190.
- [187] D.C. Young, *Computational chemistry: A practical guide for applying techniques to real world problems*, Wiley, New York, 2001.
- [188] J. Grotendorst, N. Attig (Eds.), *Multiscale simulation methods in molecular sciences: Winter school, 2 - 6 March 2009, Forschungszentrum Jülich, Germany ; lecture notes*, Supercomputing Centre Forschungszentrum Jülich, Jülich, 2009.
- [189] S. Katnagallu, M. Dagan, S. Parviainen, A. Nematollahi, B. Grabowski, P.A.J. Bagot, N. Rolland, J. Neugebauer, D. Raabe, F. Vurpillot, M.P. Moody, B. Gault, Impact of local electrostatic field rearrangement on field ionization, *J. Phys. D: Appl. Phys.* 51 (2018) 105601.
- [190] G.A. Landrum, R. Dronskowski, The Orbital Origins of Magnetism, *Angew. Chem. Int. Ed.* 39 (2000) 1560–1585.
- [191] P.M. Voyles, J.E. Gerbi, M.M. Treacy, J.M. Gibson, J.R. Abelson, Absence of an abrupt phase change from polycrystalline to amorphous in silicon with deposition temperature, *Phys. Rev. Lett.* 86 (2001) 5514–5517.

Paper I

Thermal expansion of Pd-based metallic glasses by ab initio methods and high energy

X-ray diffraction

S. Evertz, D. Music, V. Schnabel, J. Bednarcik and J. M. Schneider

Scientific Reports **7**, 15744 (2017), doi:10.1038/s41598-017-16117-7

SCIENTIFIC REPORTS



OPEN

Thermal expansion of Pd-based metallic glasses by *ab initio* methods and high energy X-ray diffraction

Simon Evertz¹, Denis Music¹, Volker Schnabel², Jozef Bednarcik³ & Jochen M. Schneider¹

Metallic glasses are promising structural materials due to their unique properties. For structural applications and processing the coefficient of thermal expansion is an important design parameter. Here we demonstrate that predictions of the coefficient of thermal expansion for metallic glasses by density functional theory based *ab initio* calculations are efficient both with respect to time and resources. The coefficient of thermal expansion is predicted by an *ab initio* based method utilising the Debye-Grüneisen model for a Pd-based metallic glass, which exhibits a pronounced medium range order. The predictions are critically appraised by *in situ* synchrotron X-ray diffraction and excellent agreement is observed. Through this combined theoretical and experimental research strategy, we show the feasibility to predict the coefficient of thermal expansion from the ground state structure of a metallic glass until the onset of structural changes. Thereby, we provide a method to efficiently probe a potentially vast number of metallic glass alloying combinations regarding thermal expansion.

Metallic glasses are promising materials for micromechanical structural applications due to the combination of high strength and elasticity, hardness and toughness^{1–3}, leading to an outstanding property combination compared to other material classes⁴. In addition to these property combinations, the absence of microstructural features² makes metallic glasses ideal for micromechanical applications. The low viscosity in the supercooled liquid region allows the near net-shape production of structural components by thermoplastic forming, while volume shrinkage during casting is one magnitude lower compared to crystalline materials due to the lack of a first order phase transition during solidification⁵. For processing by near net shape production methods and application in micromechanical devices the coefficient of thermal expansion (CTE) is of critical importance in terms of dimensional accuracy and thermal stresses^{1–3,5}.

Pd-based metallic glasses exhibit promising property combinations such as high strength and toughness, leading to damage tolerant materials⁶. Schnabel *et al.* reported a metalloid-free Pd_{57.0}Al_{23.9}Y_{7.7}Cu_{11.4} metallic glass with extensive plastic deformation before fracture and a high damage tolerance⁴. Following the electronic structure based design proposal of Schnabel *et al.* that a low fraction of hybridised bonds is a fingerprint of damage-tolerance⁴, Pd_{62.1}Al_{27.3}Y_{4.2}Ni_{6.4} is predicted to exhibit damage tolerance. In addition to the damage tolerance, the knowledge of the CTE is crucial for potential micromechanical applications.

While knowledge based *ab initio* models to predict structure and mechanical, electrical and magnetic properties of metallic glasses are state of the art^{7–10}, there are no reports on Debye-Grüneisen model to predict the CTEs of metallic glasses in literature. The CTEs of cubic^{11–17}, tetragonal^{16,17}, hexagonal and trigonal materials¹⁷ have been calculated by the Debye-Grüneisen model. To our knowledge, the Debye-Grüneisen model has not been applied to amorphous materials yet. Here it is demonstrated that the *ab initio* based prediction of CTEs is efficient with respect to time and resources. As a model system we have evaluated a Pd_{54.7}Al_{23.5}Y_{7.8}Ni_{11.3} thin film metallic glass by the *ab initio* based Debye-Grüneisen model and validated the theoretical predictions by high energy X-ray diffraction experiments.

¹Materials Chemistry, RWTH Aachen University, Kopernikusstr. 10, 52074, Aachen, Germany. ²Laboratory for Nanometallurgy, ETH Zürich, Vladimir-Prelog-Weg 5, 8093, Zurich, Switzerland. ³Deutsches Elektronen-Synchrotron DESY, FS-PE Group, Notkestr. 85, 22607, Hamburg, Germany. Correspondence and requests for materials should be addressed to S.E. (email: evertz@mch.rwth-aachen.de)

Methods

In this work, *ab initio* molecular dynamic simulations were carried out using the density functional theory¹⁸ based openMX code^{19,20}. Electronic potentials with the generalised gradient approximation were employed²¹. Basis functions were linear combinations of localised pseudoatomic orbitals²². The following basis functions were applied: Pd5.0-s2p1d1, Al6.0s1p2, Y6.5-s3p2d1 and Ni6.0-s2p2d2f1. The first symbol designates the chemical element followed by the cutoff radius. The last set of symbols defines the primitive orbitals. An N-point grid of $85 \times 85 \times 85$ and a cutoff energy of 150 Ry has been used. For volume relaxation at 0 K the Vienna *Ab-initio* Simulation Package was utilised^{23,24}. Thereby, the ultrasoft pseudopotentials were employed and the Brillouin zone was integrated on a $3 \times 3 \times 3$ Monkhorst-Pack *k*-point grid²⁵.

To model both short- and medium-ranged order, the structural model introduced by Hostert *et al.*⁸ was modified in terms of the size of the supercell and of relaxation time. Here, a larger supercell containing 389 atoms and 43 vacancies was employed. In order to obtain an amorphous structure, the supercell was heated to 4000 K for 4000 fs and quenched to 0 K with infinite cooling rate until the volume change between two subsequent cycles was <2%. As described previously by Hostert *et al.*⁸, the application of an infinite cooling rate is appropriate compared to cooling rates accessible in thin film synthesis. The bulk modulus B was obtained from the ground state by fitting the volume-energy data with the Birch-Munarghan equation of state²⁶. Shear and Young's modulus were calculated by means of volume conservative distortions²⁷. In order to allow a medium range order to develop, relaxation of the atomic positions was allowed at 300, 400, 700 and 800 K for 4400 fs. Taking the scattering powers of the constituents into account, the pair distribution function (PDF) $g(r)$ was calculated from the atomic positions⁸.

To estimate the CTE, a Debye-Grüneisen theory based method described by Söderlind *et al.*¹¹ was used. Thereby the Helmholtz free energy (eq. (1)) was calculated for different temperatures.

$$F(r, T) = E_e(r) - Nk_B T \left[3 \left(\frac{T}{\Theta} \right)^3 \int_0^{\frac{\Theta}{T}} \frac{x^3}{e^x - 1} dx - 3 \ln \left(1 - e^{-\frac{\Theta}{T}} \right) - \frac{9\Theta}{8T} \right] \quad (1)$$

$E_e(r)$ is the temperature independent electron energy, N the number of atoms in the supercell, k_B Boltzmann's constant and T the temperature. From the mechanical properties obtained in the *ab initio* calculations, namely bulk modulus B and Poisson's ration ν , the Debye temperature Θ was calculated by eq. (2)

$$\Theta = \frac{h}{k_B} \left(\frac{4\pi}{3} \right)^{-\frac{1}{6}} \left[\frac{2}{3} \left(\frac{2}{1-2\nu} \right)^{\frac{3}{2}} + \frac{1}{3} \left(\frac{1}{1-\nu} \right)^{\frac{1}{3}} \right]^{\frac{1}{3}} \left(\frac{3}{1+\nu} \right)^{\frac{1}{2}} \left(\frac{rB}{M} \right)^{\frac{1}{2}} \quad (2)$$

h is the Planck constant and M the atomic mass. The dependence of the free energy on the Wigner-Seitz radius r was introduced via the change of Debye Θ temperature with r (eq. (3)), whereby γ is the Grüneisen parameter and r_0 the equilibrium radius.

$$\Theta = \Theta_0 \left(\frac{r_0}{r} \right)^{3\gamma} \quad (3)$$

From the free energy curve calculated for several temperatures the equilibrium radii at each temperature were calculated. From the change of the equilibrium radius r_0 with temperature T, the linear and volumetric thermal expansion coefficients α_{lin} and α_{vol} , respectively, were obtained by eq. (4)

$$\alpha_{lin}(T) = \frac{1}{3} \alpha_{vol} = \frac{1}{r_0(T)} \frac{dr_0(T)}{dT} \quad (4)$$

To measure the thermal expansion by synchrotron X-ray diffraction Pd_{62.1}Al_{27.3}Y_{4.2}Ni_{6.4} thin films were deposited on rotating NaCl substrates by magnetron sputtering of elemental targets in DC mode in an ultra-high vacuum chamber (base pressure <51 mPa). Floating bias was utilised, the power densities on the Pd, Al, Y and Ni targets were 4.2, 4.7, 1.7 and 1.3 W/cm², respectively. Ar was employed as working gas with a pressure of 0.4 Pa during sputtering. For the synchrotron measurements, the NaCl substrate was dissolved in water to obtain thin film particles, which were subsequently cleaned in isopropanol and acetone.

High-energy X-ray diffraction was conducted at beamline P02.1 of the PETRA III electron storage ring at DESY, Hamburg. X-rays with a wavelength of 0.20701 Å were used and data collected with a Perkin Elmer XRD1621 fast detector. The sample was positioned in a Linkam THMS 600 heating stage and heated up with a heating rate of 10 K/min up to 863 K, hold at this temperature for 300 s and cooled down to room temperature with 10 K/min. Diffraction patterns were taken continuously with a measurement and detector read-out time of 12 s. The diffraction patterns were integrated over this time interval, which leads to a temperature resolution of 2 K. We used the FIT2D software^{28–30} to process the diffraction patterns.

The thermal expansion of an amorphous substance is connected to the shift of the principal peak position Q in reciprocal space as described in eq. (5)³¹, where Q is the principal peak position, V the atomic volume and α_{vol} the volumetric CTE. T_0 indicates the reference temperature, in this study room temperature.

$$\left\{ \frac{Q(T_0)}{Q(T)} \right\}^3 = \frac{V(T)}{V(T_0)} = 1 + \alpha_{vol}(T - T_0) \quad (5)$$

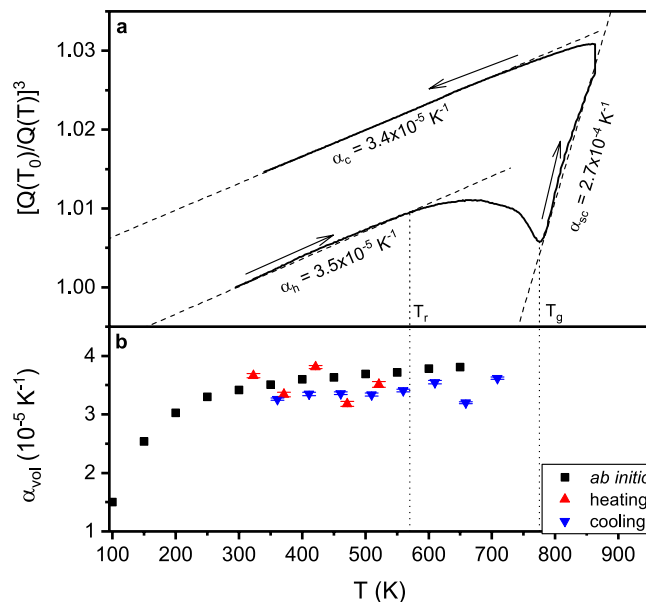


Figure 1. Thermal expansion of a Pd based metallic glass. **(a)** Ratio of the principle peak positions of the structure factor $(Q(T_0)/Q(T))^3$ of $\text{Pd}_{62.1}\text{Al}_{27.3}\text{Y}_{4.2}\text{Ni}_{6.4}$ as a function of temperature. The dashed lines are linear fits with the slopes as the volumetric coefficient of thermal expansion in the heating, cooling and supercooled region α_h , α_c and α_{sc} , respectively. Dotted lines mark the relaxation and glass transition temperature T_r and T_g . Arrows indicate the direction of heating. **(b)** Coefficient of thermal expansion of $\text{Pd}_{54.7}\text{Al}_{23.5}\text{Y}_{7.8}\text{Ni}_{11.3}$ by *ab initio* based Debye-Grüneisen model. Debye temperature is 332 K. The red and blue triangles represent the experimental CTEs in the heating and cooling sections, respectively.

The principal peak was fitted by a Pseudo-Voigt function in order to obtain the quantitative peak positions. Throughout this work, all CTEs are given as volumetric CTEs.

To study the structural changes during heating, the structure factor $S(Q)$ and the reduced PDF $G(r)$ were obtained using the PDFgetX3 software³². From the structure factor $S(Q)$ the reduced PDF $G(r)$ was calculated by a Fourier transformation. $g(r)$ and $G(r)$ are connected by

$$g(r) = \frac{\rho(r)}{\rho_0} = \frac{G(r)}{4\pi\rho_0 r} + 1 \quad (6)$$

Results and Discussion

In this part, first the CTE of $\text{Pd}_{54.7}\text{Al}_{23.5}\text{Y}_{7.8}\text{Ni}_{11.3}$ metallic glass is predicted by the Debye-Grüneisen model and critically appraised by *in situ* X-ray diffraction. Thereafter, the calculated and experimentally observed structures are compared to validate the employed *ab initio* model. In the third part, a refined structural analysis is conducted to investigate the changes in the atomic structure observed in the experiments.

Thermal expansion. We evaluate the thermal expansion of $\text{Pd}_{62.1}\text{Al}_{27.3}\text{Y}_{4.2}\text{Ni}_{6.4}$ thin film metallic glasses by *in situ* X-ray diffraction and by *ab initio* methods utilising the Debye-Grüneisen model. Figure 1(a) shows the synchrotron X-ray diffraction results for the thermal expansion of $\text{Pd}_{62.1}\text{Al}_{27.3}\text{Y}_{4.2}\text{Ni}_{6.4}$ thin film powder. The ratio of the principal peak positions $(Q(T_0)/Q(T))^3$ of the structure factor $S(Q)$ is depicted as a function of temperature since this ratio is directly related to volume changes in the glass^{31,33,34}. Thus, the CTE is related to $(Q(T_0)/Q(T))^3$ below T_g provided that no structural change occurs³¹, as has been reported for several La-, Pd-, Sm-, Co- and Zr-based metallic glasses^{31,33–40}. In the heating section, beginning at room temperature, the ratio $(Q(T_0)/Q(T))^3$ is increasing linearly. From 570 K onwards (this temperature is referred to as relaxation temperature T_r), the CTE decreases and eventually turns negative at $T_n = 670$ K. The $(Q(T_0)/Q(T))^3$ curve reaches a minimum at 775 K. According to Bednarcik *et al.*³⁴ the minimum in the $(Q(T_0)/Q(T))^3$ curve corresponds to the glass transition temperature T_g . The continuing change in the $(Q(T_0)/Q(T))^3$ ratio due to homogenisation of the sample temperature at the maximum temperature of 863 K during a holding time of 5 min causes an infinite slope. In the cooling section, the $(Q(T_0)/Q(T))^3$ ratio decreases linearly. The linear regions of the heating and cooling sections are fitted in intervals of 50 K. The resulting CTEs are shown in Fig. 1(b). The average in CTE for the heating and cooling section are $3.5 \pm 0.2 \times 10^{-5}$ and $3.4 \pm 0.1 \times 10^{-5} \text{ K}^{-1}$, respectively, which is consistent with CTE for other Pd-based metallic glasses⁴¹. In the supercooled region above T_g we measured a CTE of $2.7 \times 10^{-4} \text{ K}^{-1}$, which is 8 times larger than the CTEs in the glassy regions. This can be rationalized based on additional excitations of atomic oscillators at the glass transition^{33,34,42}. In contrast to the thermal expansion while cooling, the thermal expansion while heating begins to deviate from a linear dependence at T_r . Throughout the whole cooling region a linear dependency of $(Q(T_0)/Q(T))^3$ to the temperature is observed. The non-linear dependency of $(Q(T_0)/Q(T))^3$ on temperature while heating is caused by the annihilation of free volume in the structure^{31,33,43}. The CTEs in the

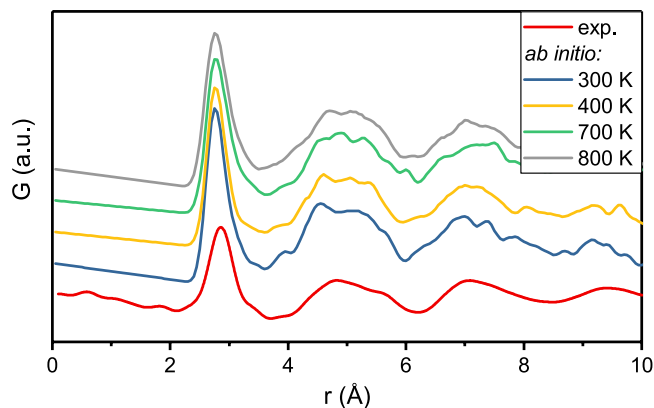


Figure 2. Experimental and calculated pair distribution functions of $\text{Pd}_{62.1}\text{Al}_{27.3}\text{Y}_{4.2}\text{Ni}_{6.4}$ at 300, 400, 700 and 800 K.

heating and cooling section are consistent within the error of the measurement. This holds because the difference in free volume between the heating and cooling curves does not influence the relative shift of the principle maximum of $S(Q)$ in the relaxation free temperature region³³. While heating the metallic glass, excess free volume is annihilated. Hence, with increasing temperature the thermal expansion is superimposed by free volume annihilation. Above T_r the influence of free volume annihilation on the macroscopic thermal expansion is larger than the thermal volume expansion. Eventually, this causes a negative CTE at 670 K.

Figure 1(b) depicts the calculated CTEs from the Debye-Grüneisen model based on the *ab initio* calculations in the ground state and the experimental CTEs as a function of temperature. The calculated CTEs increase between 100 and 300 K from 1.5×10^{-5} to $3.4 \times 10^{-5} \text{ K}^{-1}$. Above the Debye temperature $\Theta_D = 332 \text{ K}$, the CTE increases only slightly. Hence, we observe excellent agreement between the experimentally and theoretically obtained CTEs of the $\text{Pd}_{54.7}\text{Al}_{23.5}\text{Y}_{7.8}\text{Ni}_{11.3}$ thin film metallic glass, which is within the error of the measurement and the precision of the Debye temperature calculation. The Debye temperature depends on the temperature dependent equilibrium volume, elastic constants and composition, whereby the calculated CTE can deviate up to 30%¹⁷. The Debye-Grüneisen method models the acoustic mode of the phonons below Θ and the increased amplitudes of anharmonic vibrations at higher temperatures by the Grüneisen constant as long as structural changes such as relaxation or the approach of the melting point do not occur¹³. Deviations of the experimentally obtained CTEs from the predicted CTEs indicate regions with and without structural relaxation. For $\text{Pd}_{62.1}\text{Al}_{27.3}\text{Y}_{4.2}\text{Ni}_{6.4}$ the experimental CTE begins to decrease at T_p , marking the onset of structural relaxation. Therefore, we propose the Debye-Grüneisen model as a reliable *ab initio* based method to predict CTEs of metallic glasses, provided a realistic structural model is applied, which will be discussed in the next section.

The applicability of the Debye-Grüneisen model can be justified by the work of Safarik and Schwarz⁴⁴. The signature of a metallic glass in terms of lattice vibrations are low frequency lattice vibrations that can be modelled by Einstein oscillators. These vibrations that deviate from the Debye model are highly anharmonic. However, the anharmonic modes do not influence the bulk modulus⁴⁴. As the bulk modulus is one major input parameter for the Debye-Grüneisen model and is not influenced by an anomalous large density of low frequency vibrations in glasses, this model can be applied for metallic glasses without the addition of Einstein oscillators in the Debye-Grüneisen model.

Ab initio structural model vs. experiment. The CTE predicted by the Debye-Grüneisen model depends entirely on the atomic configuration obtained in the *ab initio* calculations. Hence, we will compare the simulated configuration with the experimentally observed one. Besides topology, glass transition temperature is a representative gauge to judge the validity of an atomic configuration. The glass transition temperature T_g is estimated by an empirical model introduced by Wang *et al.*⁴⁵. They report the ratio of $1000T_g$ and $M\Theta_D^2$ (the Lindemann criterion) is approximately constant for metallic glasses, considering Zr-based, Pd-based, Nd-based, La-based and Cu-based metallic glass systems, where M is the average atomic mass⁴⁵. Based on this model, T_g of the calculated structure is 981 K compared to 775 K in the experiment (Fig. 1). This difference of 20% between theory and experiment is comparable with the deviations expected for the predicted CTE and even smaller compared to deviations of T_g calculated by classical molecular dynamics simulations for Ni-P^{45,46} and Zr-Al-Ni^{47,48} to the corresponding experimental values. Causes for this deviation might be the infinite quenching rate that increases T_g ⁴⁶ and the small difference in composition caused by the discrete number of atoms in the supercell. Thus, the accuracy of our structural model with respect to T_g is within the temperature range expected from our model and literature.

Short and medium range order have been reported in literature to have different contributions to thermal expansion⁴⁰. Hence, we compare the calculated and experimentally obtained PDF in Fig. 2. The PDFs calculated for 300, 400, 700 and 800 K, i.e. for whole temperature range encompassing T_r as well as T_p , resemble the first peak of the experimental PDF at 2.8 Å with a deviation of 0.1 Å. The second coordination shells of the calculations overlap with the experimental one. Similar to the experimental PDF, the calculated PDF for 300 K exhibits a distinct peak splitting with a peak at 4.8 Å and a shoulder at 5.3 Å, i.e. at the same positions as in the experimental case. The peak splitting is observed up to 800 K. In the third coordination shell, the calculated PDF at 300 K shows

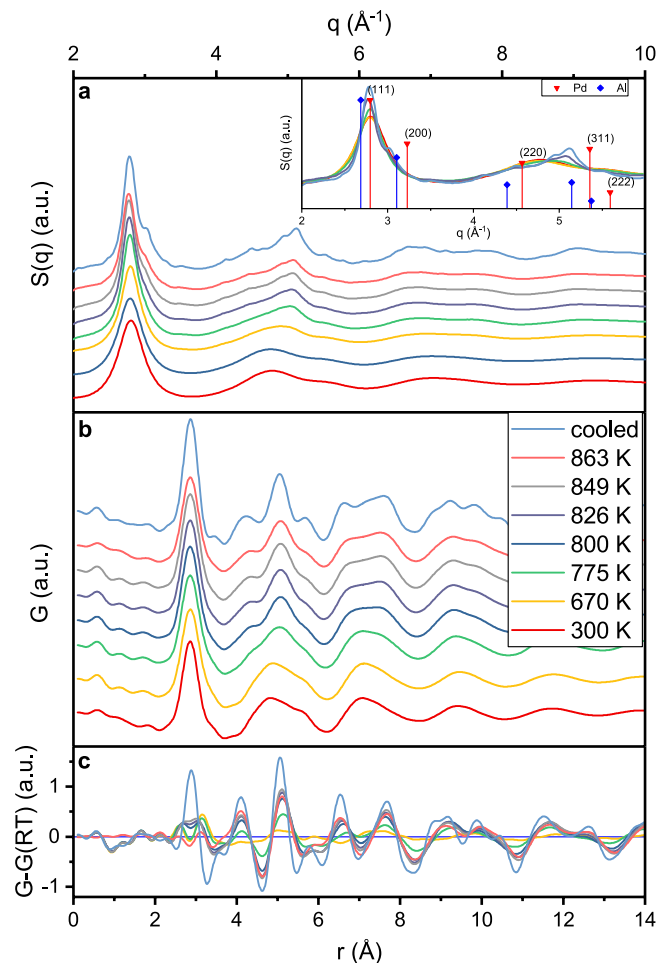


Figure 3. Changes in the structure of $\text{Pd}_{62.1}\text{Al}_{27.3}\text{Y}_{4.2}\text{Ni}_{6.4}$ during *in situ* heating and cooling. Structure factor $S(Q)$ (a) and PDF (b) and difference between PDF at elevated temperature and room temperature (c) of $\text{Pd}_{62.1}\text{Al}_{27.3}\text{Y}_{4.2}\text{Ni}_{6.4}$ for room temperature (300 K), 670 K, glass transition temperature (775 K), the supercooled region (800, 826 and 849 K), maximum heating temperature and the cooled down sample. The inset in (a) shows the peak positions of the Bragg peaks of the fcc-phases of the main constituents Pd and Al.

two distinct peaks which are different from the experimentally observed peak. However, the calculated third coordination shell covers the relevant r -range between 6.0 and 8.5 Å and exhibits the same asymmetric shape as the experimentally observed third coordination shell. For higher temperatures of 700 and 800 K the major peaks in the third coordination shell of the calculated PDFs are within the range of 7.5 and 7.0 Å. Despite computational constraints, the description of the short-range order up to the second coordination shell is feasible at room temperature, as the calculated PDF at 300 K resembles the experimental PDF despite the noise due to the low number of atoms. Therefore, the *ab initio* model introduced in ref.⁸ for a metalloids containing metallic glass produces a realistic atomic structure of a metalloids free metallic glass if the size of the supercell is adjusted to comprise higher coordination shells. Therefore, the increased size of the supercell compared to ref.⁸ is necessary. However, to account for structural relaxation an even larger supercell would be required. The number of 389 atoms used here, which corresponds to an increase of 338% in reference to ref.⁸, is still 1.5 times smaller than the number of atoms found in regions of correlative motion during structural relaxation in Pd-based metallic glasses⁴⁹. To summarize the comparison of *ab initio* model and experimentally observed structure, the calculated PDF, glass transition temperature and CTE are consistent with the experimental values. Hence, the *ab initio* model represents an atomic configuration comparable to the atomic configuration obtained with magnetron sputtering.

Structural rearrangements. The deviation of $(Q(T_0)/Q(T))^3$ from a linear dependence on T and the deviation of the CTE from the theoretical prediction at T_r indicate the onset of structural rearrangements, which have implications on mechanical properties⁴³. Temperature induced mechanical property and phase stability changes are of key importance for structural applications⁴¹. Thus, to investigate the atomic rearrangements, we employed a refined structural analysis. To understand the influence of structural rearrangements on the medium range order, we compare the structure factor obtained by high energy X-ray diffraction at room temperature; $T_n = 670$ K, at which the CTE changes from positive to negative values; $T_g = 775$ K; and the maximum heater temperature of 863 K (Fig. 3(a)). From the comparison of the structure factor at RT and 670 K we observe a slight peak shift towards lower wavevectors, while the peak width begins to decrease at T_r (Fig. 4(a)). This indicates an

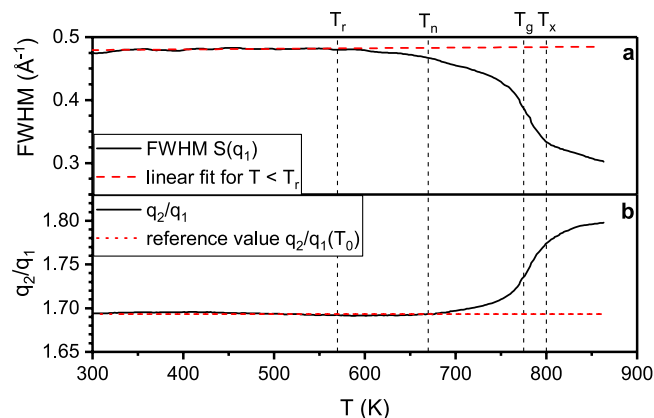


Figure 4. Changes in the structure factor with temperature. (a) Full width half maximum (FWHM) of principal peak of the structure factor as a function of temperature in the heating section, the dashed line is a linear fit of the FWHM below T_r , (b) second to first peak ratio q_2/q_1 of the structure factor as a function of temperature in the heating section, the dashed line marks a constant q_2/q_1 ratio.

onset of structural rearrangements towards a more ordered structure, which is consistent with the comparison of predicted and measured CTE. Between 670 K and $T_g = 775$ K, the second peak of $S(Q)$ (Fig. 3(a)) shifts significantly towards larger q values from 4.77 to 4.90 \AA^{-1} . Furthermore, the ratio of first and second peak positions q_2/q_1 (Fig. 4(b)) deviates from a constant value above 670 K. Hence, starting at $T_n = 670$ K inelastic structural changes occur that cannot solely be attributed to thermal expansion³³. The changes in $S(Q)$ (Fig. 3(a)) indicate that atomic rearrangements become more pronounced in the supercooled liquid region between T_g and 863 K. In the supercooled liquid region, the principal peak develops a shoulder at 3 \AA^{-1} and decreases in height due to atomic rearrangements, while a peak sharpening of the main peak in the second coordination shell is observed, indicating the onset of the Bragg peaks and hence structural rearrangements towards the formation of a crystalline phase. These small Bragg peaks are irreversible and clearly visible in the cooled down sample, which consists of nanocrystals in an amorphous matrix after the heating cycle.

Comparing the peak positions of $S(Q)$ to the Bragg peaks of the crystalline phases of the main constituents Pd and Al (inset in Fig. 3(a)), the principle peak shifts towards the (111) peak of Pd, while the shoulder of the principal peak is near the Bragg peaks of the (200) plane. The main peak of the second coordination shell matches the (311) peak of Al, while its shoulders are between the (220) and (222) peaks, respectively, of both elements. Thus, the fcc crystalline structures appear to evolve via fcc-like short-range ordered clusters before the onset of crystallisation. Similar observations have been reported by Voyles *et al.* for the amorphous to crystalline transition of Si⁵⁰.

Despite the nanocrystalline phase in the glass present in the cooling region, the CTE for the glass and a nanocrystal-glass composite material are equal within the error of the measurement. This equivalence of CTEs may be explained by the portion of the amorphous phase and the similarity of the CTE of the major constituent Pd. The rather broad principle peak of $S(Q)$ of the cooled down sample in Fig. 3(a) and the small Bragg peak indicate a considerably large amorphous portion after the heating and cooling cycle. Additionally, the CTE of $3.4 \times 10^{-5} \text{K}^{-1}$ for main constituent Pd¹³ is in agreement with the calculated CTE for the amorphous phase. Thus, the difference of CTE between crystalline and amorphous phase might be small, wherefore the CTE of the nanocrystal-glass composite is equal to the amorphous CTE.

Complementary to the medium-range order analysis, the development of short-range order is probed by employing real space PDFs. The experimentally obtained real space reduced PDF $G(r)$ shown in Fig. 3(b) underlines the structural changes during heating. Corrugations at bond distances lower than 2.1 \AA are artefacts from the Fourier transform of $S(Q)$ to $G(r)$ ⁵¹. The first peaks of $G(r)$ are at distances of 2.9, 4.8, 7.1 and 9.4 \AA . The first peak indicates Pd-dominated bonding, as its position is at the distance of Pd-Pd bonds in icosahedral coordination. The $G(r)$ at RT and 670 K resemble each other in terms of peak shape and position. Within the temperature range of RT to 863 K the shape of the nearest neighbour shell remains unchanged. However, the peak height is decreasing until T_g by 13%, while the full width half maximum (FWHM) is increasing until T_g by 8%. The difference between the PDF at elevated temperatures and PDF at 300 K (Fig. 4(c)) shows an increase of the peak flanks with a larger portion at the right flank, while the height at the peak centre decreases. Thus, thermal rejuvenation might occur, that broadens the atomic bond length distribution in the first coordination shell and thereby increases the disordering⁵² by thermally activated atomic movements. However, the thermal rejuvenation of the short range order does not affect the average atomic volume, as the FWHM of the principle peak of $S(Q)$ begins to narrow and the $(Q(T_0)/Q(T))^3$ ratio begins to change already at 570 K. Since the average volume is represented by the principle peak of $S(Q)$, the changing $(Q(T_0)/Q(T))^3$ ratio indicates free volume annihilation³¹ concurrent to thermal rejuvenation of the short range order. As can be derived by the continuously changing slope of $(Q(T_0)/Q(T))^3$ towards a more negative value, the free volume annihilation rate in the medium range order increases up to T_g , where the average atomic volume begins to increase again. Thermal rejuvenation stops at the glass transition temperature, where structural relaxation sets on as the FWHM decreases and principle peak height increases⁵³ strongly up to T_x , where the slope decreases and thus structural relaxation slows down. During

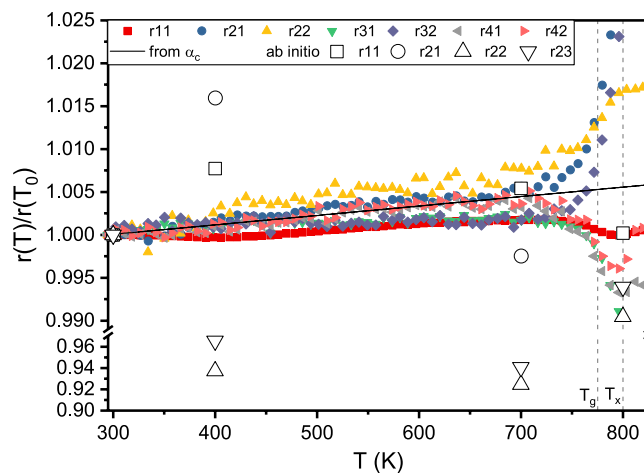


Figure 5. Relative shift of peak positions r_{ij} of $G(r)$ as a function of temperature of the j^{th} peak in the i^{th} coordination shell. The solid line marks the relative peak shift expected from the average CTE α_c obtained from the structure factor $S(Q)$. Empty symbols represent relative peak shifts of the calculated PDF from Fig. 2. T_g and T_x are the glass transition and crystallisation temperature, respectively.

structural relaxation, the right flank of the first coordination shell decreases (Fig. 4(c)), while the left flank is increased compared to the reference. Thus above T_g , free volume annihilation takes place in the short range order due to removal of large atomic bond distances⁵³. This structural relaxation towards a more ordered structure at T_x is consistent with the continuous development of a more ordered (crystalline) structure, which has been already observed by the evolution of the Bragg peaks in $S(Q)$.

While free volume is annihilated between the nearest neighbours above T_g , peak splitting is observed for the second to fifth coordination shell, indicating chemical rearrangement. Whereas the major subpeak of the second coordination shell below T_g is at 4.8 Å, the major peak at T_g is at 5.1 Å with shoulders at 4.3 and 5.6 Å. These three subpeaks become more pronounced with increasing temperature in the supercooled region. Also in the third coordination shell the subpeak at 7.4 Å, which was not dominating below T_g , evolves at T_g and eventually dominates the third coordination shell in the supercooled region. Shoulders evolve also in the fourth coordination shell in the supercooled region. This evolution of subpeaks in the second to fourth coordination shell hints to a rearrangement of local chemical environment⁵³ of Pd, which is the major constituent in this metallic glass.

The different behaviour of short and medium range order in terms of free volume annihilation, thermal rejuvenation and relaxation hints to a heterogeneous atomic environment on the short range order level. To understand the relation of the individual coordination shells in the short range ordered region and the thermal expansion, we calculated the temperature induced relative shift of peak positions of the individual coordination shells. Figure 5 depicts the relative shift of the peak positions r_{ij} of the PDF (indices indicating the j^{th} peak in the i^{th} coordination shell) during heating. The average thermal expansion obtained from the shift of the principle peak of $S(Q)$ is indicated by a solid line and supposed to be approximately the macroscopic thermal expansion⁴⁰. The reference peak positions at $T_0 = RT$ for r_{11} , r_{21} , r_{22} , r_{31} , r_{32} , r_{41} and r_{42} are 2.86, 4.75, 5.05, 6.95, 7.29, 9.26 and 9.54 Å, respectively. From Fig. 5 we learn that the thermal expansion of the coordination shells is inhomogeneous. The first and third coordination shell contract compared to the macroscopic thermal expansion, while the second coordination shell expands more than by the macroscopic thermal expansion. The expansion of the fourth coordination shell matches the macroscopic thermal expansion. The peak shifts of the first to third coordination shells are due to rearrangements on the atomic level (Fig. 3(b,c)). Comparing the cooled down sample to the initial sample, the second peak at 3.4 Å forms in the first coordination shell, might be associated with the bonds involving Y, while the second coordination shell consists of three distinct peaks at 4.2, 5.0 and 5.7 Å instead of one peak containing two subpeaks. The difference of the PDF of the cooled down sample and the pristine sample (Fig. 3(c)) reveals a sharpening of the peak of the first coordination shell, indicating a narrower bond length distribution. The distinct peaks in the second coordination shell verify the increased ordering in the sample after the heating cycle. However, in Fig. 5 we observe that the higher coordination shells reflect the macroscopic thermal expansion obtained from the principal peak shift in $S(Q)$ ⁴⁰. This can readily be understood based on the inverse relationship between wavenumber and bond distance. The principal peak of $S(Q)$ contains the major information of the medium range order^{34,54}. Thus, it is learned from the analysis of both $S(Q)$ and $G(r)$ that the macroscopic thermal expansion is reflected by the medium range order, while irreversible changes take place in the heterogeneous atomic environment of the short and near medium range order up to bond distances of 13.2 Å, which is in agreement to literature reports⁴⁰ on CuZr metallic glasses. During structural relaxation, the exchange of atoms with different sizes between the heterogeneous coordination shells is possible⁵⁵, allowing the contraction and expansion of coordination shells as is the case for the first to third coordination shell, leading to inhomogeneous thermal expansion on the atomic scale. Following the shifts of the peak positions in Fig. 5 we observe a significant change in slope around 745 K, inferring an increased rate of structural rearrangements. The inflection point at 775 K corresponds to the glass transition temperature T_g observed in $(Q(T_0)/Q(T))$ ³. Further heating leads to a

minimum at 800 K. This change of slope in real space is identified as crystallisation temperature T_x ³⁴. This temperature coincides with the flattening of the width of the principle peak of the structure factor and of the q_2/q_1 -ratio in Fig. 4. The onset of crystallisation at T_x is consistent with the observation of Bragg peaks in the structure factor (Fig. 3(a)) inferring nanocrystal formation within a glassy matrix.

The empty symbols in Fig. 5 show the relative peak shifts of the calculated PDFs in Fig. 2 and underline the lack of structural relaxation in the *ab initio* model. The peak positions of the calculated PDF do not shift in accordance with the experiments, but show a strong scattering. The scattering is likely caused by the small volume of the supercell, which introduces noise into the calculated PDF that is also observed for bond distance larger 4 Å (Fig. 2). Hence, a direct determination of CTEs from the shift of peak positions in real space is not feasible. However, as shown in Fig. 2 the description of the short-range order up to the third coordination shell by *ab initio* calculations is possible at room temperature. This enables the prediction of CTEs with the Debye-Grüneisen model, which is more efficient in terms of time and resources compared to experimental methods.

Conclusion

The average room temperature CTE of the $\text{Pd}_{54.7}\text{Al}_{23.5}\text{Y}_{7.8}\text{Ni}_{11.3}$ thin film metallic glass obtained from Debye-Grüneisen model is $3.4 \times 10^{-5} \text{ K}^{-1}$, while the experimental CTEs calculated from *in situ* heating and cooling cycles in synchrotron X-ray diffraction experiments are $3.5 \pm 0.3 \times 10^{-5}$ and $3.4 \pm 0.1 \times 10^{-5} \text{ K}^{-1}$, respectively. Hence, we observe excellent agreement between the experimentally and theoretically obtained CTEs. Therefore, we propose the Debye-Grüneisen model as a reliable *ab initio* based method for predicting the CTE of metallic glasses. A comparison between the calculated and experimental PDF shows that the experimentally observed structure at room temperature is well resembled by the *ab initio* model. The temperature induced structural relaxation is not covered by our model containing 389 atoms, which is the cause for the deviation between theoretical and experimental CTE data for temperatures above T_r . The deviation originates in the rearrangement of atoms and the annihilation of free volume during structural relaxation within the experiment.

The *in situ* high energy X-ray diffraction structure analysis reveals an inhomogeneous expansion of the individual coordination shells. For the $\text{Pd}_{62.1}\text{Al}_{27.3}\text{Y}_{4.2}\text{Ni}_{6.4}$ thin film metallic glass the macroscopic thermal expansion is dominated by the medium range order, while thermal rejuvenation and atomic rearrangements are observed in the short range order. Structural relaxation of the average structure starts at 570 K. The glass transition temperature of $\text{Pd}_{62.1}\text{Al}_{27.3}\text{Y}_{4.2}\text{Ni}_{6.4}$ is 775 K, which we identified through a change of signs of the CTE. Above T_g , the peaks of $S(Q)$ shift towards the positions of the Bragg peaks of the crystalline phases of the main constituents. Hence, before the onset of crystallisation a continuous evolution towards a fcc structure via a fcc-like arrangement of short-range ordered clusters is proposed, leading to the formation of a nanocrystal-glass composite material. The crystallisation temperature of 800 K is 25 K higher than T_g . The akin CTEs of the metallic glass and nanocrystal-glass composite material suggest thermal expansion based on the same mechanism of coordinated vibrations of strings of atoms next to highly defective areas in Pd-based metallic glasses and nanocrystal-glass composites.

Based on the average atomic volume, we observe free volume annihilation in the medium range order that exceeds the volume expansion at 670 K leading to a negative thermal expansion. Above T_g , free volume annihilation takes place in the short range order, while the average atomic volume increases in the supercooled region.

Data availability statement. The data generated and analysed during this study are available from the corresponding author on reasonable request.

References

- Telford, M. The case for bulk metallic glass. *Mater. Today* **7**, 36–43 (2004).
- Ashby, M. & Greer, A. L. Metallic glasses as structural materials. *Scripta Mater.* **54**, 321–326 (2006).
- Inoue, A., Shen, B. & Takeuchi, A. Developments and Applications of Bulk Glassy Alloys in Late Transition Metal Base System. *Mater. Trans.* **47**, 1275–1285 (2006).
- Schnabel, V. *et al.* Electronic hybridisation implications for the damage-tolerance of thin film metallic glasses. *Sci. Rep.* **6**, 36556 (2016).
- Schroers, J. Processing of bulk metallic glass. *Adv. Mater.* **22**, 1566–1597 (2010).
- Demetriou, M. D. *et al.* A damage-tolerant glass. *Nat. Mater.* **10**, 123–128 (2011).
- Wang, X. D. *et al.* Atomic picture of elastic deformation in a metallic glass. *Sci. Rep.* **5**, 9184 (2015).
- Hostert, C. *et al.* Ab initio molecular dynamics model for density, elastic properties and short range order of Co-Fe-Ta-B metallic glass thin films. *J. Phys. Condens. Mat.* **23**, 475401 (2011).
- Schnabel, V., Evertz, S., Ruess, H., Music, D. & Schneider, J. M. Stiffness and toughness prediction of Co-Fe-Ta-B metallic glasses, alloyed with Y, Zr, Nb, Mo, Hf, W, C, N and O by ab initio molecular dynamics. *J. Phys. Condens. Mat.* **27**, 105502 (2015).
- Hostert, C., Music, D., Bednarcik, J., Keckes, J. & Schneider, J. M. Quantum mechanically guided design of $\text{Co}_{43}\text{Fe}_{20}\text{Ta}_{5.5}\text{X}_{31.5}$ (X = B, Si, P, S) metallic glasses. *J. Phys. Condens. Mat.* **24**, 175402 (2012).
- Söderlind, P., Nordström, L., Yongming, L. & Johansson, B. Relativistic effects on the thermal expansion of the actinide elements. *Phys. Rev. B* **42**, 4544–4552 (1990).
- Lu, X., Selleby, M. & Sundman, B. Theoretical modeling of molar volume and thermal expansion. *Acta Mater.* **53**, 2259–2272 (2005).
- Moruzzi, V. L., Janak, J. F. & Schwarz, K. Calculated thermal properties of metals. *Phys. Rev. B* **37**, 790–799 (1988).
- Lu, X.-G., Selleby, M. & Sundman, B. Calculations of thermophysical properties of metallic glasses using the Debye-Grüneisen model. *Acta Mater.* **55**, 1215–1226 (2007).
- Tao, X. *et al.* Ab initio calculation of the total energy and elastic properties of Laves phase $\text{C}_{15}\text{Al}_2\text{RE}$ (RE = Sc, Y, La, Ce–Lu). *Comp. Mater. Sci.* **44**, 392–399 (2008).
- Deligoz, E., Ozisik, H. B., Colakoglu, K. & Ciftci, Y. O. First principles prediction of structural stability, elastic, lattice dynamical and thermal properties of osmium carbides. *Mater. Sci. Tech.* **30**, 842–849 (2014).
- Music, D., Geyer, R. W. & Keuter, P. Thermomechanical response of thermoelectrics. *Appl. Phys. Lett.* **109**, 223903 (2016).
- Hohenberg, P. & Kohn, W. Inhomogeneous Electron Gas. *Phys. Rev.* **136**, B864–B871 (1964).
- Ozaki, T. & Kino, H. Numerical atomic basis orbitals from H to Kr. *Phys. Rev. B* **69** (2004).

20. Ozaki, T. & Kino, H. Efficient projector expansion for the ab initio LCAO method. *Phys. Rev. B* **72** (2005).
21. Perdew, B. & Ernzerhof, G. Generalized Gradient Approximation Made Simple. *Phys. Rev. Lett.* **77**, 3865–3868 (1996).
22. Ozaki, T. Variationally optimized atomic orbitals for large-scale electronic structures. *Phys. Rev. B* **67** (2003).
23. Kresse, G. & Furthmüller, J. Efficient iterative schemes for ab initio total-energy calculations using a plane-wave basis set. *Phys. Rev. B* **54**, 11169–11186 (1996).
24. Kresse, G. & Joubert, D. From ultrasoft pseudopotentials to the projector augmented-wave method. *Phys. Rev. B* **59**, 1758–1775 (1999).
25. Monkhorst, H. J. & Pack, J. D. Special points for Brillouin-zone integrations. *Phys. Rev. B* **13**, 5188–5192 (1976).
26. Birch, F. Finite strain isotherm and velocities for single-crystal and polycrystalline NaCl at high pressures and 300°K. *J. Geophys. Res.* **83**, 1257 (1978).
27. Music, D. *et al.* Elastic properties of Fe–Mn random alloys studied by ab initio calculations. *Appl. Phys. Lett.* **91**, 191904 (2007).
28. Hammersley, A. P. FIT2D. An Introduction and Overview. ESRF, 1997.
29. Hammersley, A. P., Svensson, S. O., Hanfland, M., Fitch, A. N. & Hausermann, D. Two-dimensional detector software. *From real detector to idealised image or two-theta scan.* *High Pressure Res.* **14**, 235–248 (1996).
30. Hammersley, A. P., Svensson, S. O. & Thompson, A. Calibration and correction of spatial distortions in 2D detector systems. *Nucl. Instrum. Meth. A* **346**, 312–321 (1994).
31. Yavari, A. R. *et al.* Excess free volume in metallic glasses measured by X-ray diffraction. *Acta Mater.* **53**, 1611–1619 (2005).
32. Juhás, P., Davis, T., Farrow, C. L. & Billinge, S. J. L. PDFgetX3. A rapid and highly automatable program for processing powder diffraction data into total scattering pair distribution functions. *J. Appl. Crystallogr.* **46**, 560–566 (2013).
33. Mattern, N., Stoica, M., Vaughan, G. & Eckert, J. Thermal behaviour of Pd₄₀Cu₃₀Ni₁₀P₂₀ bulk metallic glass. *Acta Mater.* **60**, 517–524 (2012).
34. Bednarcik, J. *et al.* Thermal expansion of a La-based bulk metallic glass. Insight from *in situ* high-energy x-ray diffraction. *J. Phys. Condens. Mat.* **23**, 254204 (2011).
35. Georgarakis, K. *et al.* Variations in atomic structural features of a supercooled Pd–Ni–Cu–P glass forming liquid during *in situ* vitrification. *Acta Mater.* **59**, 708–716 (2011).
36. Jing, G. *et al.* Formation and interesting thermal expansion behavior of novel Sm-based bulk metallic glasses. *Intermetallics* **15**, 929–933 (2007).
37. Kato, H., Chen, H.-S. & Inoue, A. Relationship between thermal expansion coefficient and glass transition temperature in metallic glasses. *Scripta Mater.* **58**, 1106–1109 (2008).
38. Mattern, N. *et al.* Structural behavior of Pd₄₀Cu₃₀Ni₁₀P₂₀ bulk metallic glass below and above the glass transition. *Appl. Phys. Lett.* **82**, 2589–2591 (2003).
39. Qu, D. D., Mizuno, A., Watanabe, M., Bednarcik, J. & Shen, J. Undercooling behavior of Zr–Cu–Ni–Al bulk metallic glasses investigated by *in situ* synchrotron high energy X-ray diffraction. *Mater. Sci. Eng.* **555**, 36–43 (2012).
40. Mattern, N., Bednarcik, J., Stoica, M. & Eckert, J. Temperature dependence of the short-range order of Cu₆₅Zr₃₅ metallic glass. *Intermetallics* **32**, 51–56 (2013).
41. Liu, Y., Hata, S., Wada, K. & Shimokohbe, A. Thermal, Mechanical and Electrical Properties of Pd-Based Thin-Film Metallic Glass. *Jpn. J. Appl. Phys.* **40**, 5382–5388 (2001).
42. Mattern, N. *et al.* Thermal behavior and glass transition of Zr-based bulk metallic glasses. *Mater. Sci. Eng.* **375–377**, 351–354 (2004).
43. Chen, H. S. The influence of structural relaxation on the density and Young's modulus of metallic glasses. *J. Appl. Phys.* **49**, 3289–3291 (1978).
44. Safarik, D. J. & Schwarz, R. B. Evidence for highly anharmonic low-frequency vibrational modes in bulk amorphous Pd₄₀Cu₄₀P₂₀. *Phys. Rev. B* **80**, 94109 (2009).
45. Wang, W. H., Wen, P., Zhao, D. Q., Pan, M. X. & Wang, R. J. Relationship between glass transition temperature and Debye temperature in bulk metallic glasses. *J. Mater. Res.* **18**, 2747–2751 (2003).
46. Lewis, L. J. Atomic dynamics through the glass transition. *Phys. Rev. B* **44**, 4245–4254 (1991).
47. Guerdane, M. & Teichler, H. Structure of the amorphous, massive-metallic-glass forming Ni₂₅Zr₆₀Al₁₅ alloy from molecular dynamics simulations. *Phys. Rev. B* **65**, 177 (2001).
48. Inoue, A., Zhang, T. & Masumoto, T. Zr–Al–Ni Amorphous Alloys with High Glass Transition Temperature and Significant Supercooled Liquid Region. *Mater. Trans. JIM* **31**, 177–183 (1990).
49. Qiao, J., Casalini, R., Pelletier, J.-M. & Kato, H. Characteristics of the structural and Johari–Goldstein relaxations in Pd-based metallic glass-forming liquids. *J. Phys. Chem. B* **118**, 3720–3730 (2014).
50. Voyles, P. M., Gerbi, J. E., Treacy, M. M., Gibson, J. M. & Abelson, J. R. Absence of an abrupt phase change from polycrystalline to amorphous in silicon with deposition temperature. *Phys. Rev. Lett.* **86**, 5514–5517 (2001).
51. Egami, T. & Billinge, S. J. L. *Underneath the Bragg peaks. Structural analysis of complex materials* (Elsevier, Amsterdam, 2012).
52. Tong, Y. *et al.* Structural rejuvenation in bulk metallic glasses. *Acta Mater.* **86**, 240–246 (2015).
53. Dmowski, W., Fan, C., Morrison, M. L., Liaw, P. K. & Egami, T. Structural changes in bulk metallic glass after annealing below the glass-transition temperature. *Mater. Sci. Eng.* **471**, 125–129 (2007).
54. Bednarcik, J., Michalik, S., Kolesar, V., Rütt, U. & Franz, H. *In situ* XRD studies of nanocrystallization of Fe-based metallic glass. A comparative study by reciprocal and direct space methods. *Phys. Chem. Chem. Phys.* **15**, 8470–8479 (2013).
55. Tong, X. *et al.* Structural evolution and strength change of a metallic glass at different temperatures. *Sci. Rep.* **6**, 30876 (2016).

Acknowledgements

We acknowledge financial support of the German Research Foundation within the SPP 1594 “Topological Engineering of Ultrastrong Glasses”. *Ab initio* calculations were performed on the JARA HPC cluster of RWTH Aachen University within the project JARA0131. Parts of this research were carried out at beamline P02.1 of the light source PETRA III at DESY, a member of the Helmholtz Association (HGF).

Author Contributions

All authors designed the research, discussed the result and wrote the manuscript; S.E. and D.M. performed the *ab initio* molecular dynamics simulations; S.E. synthesised the samples and analysed the synchrotron data; S.E. and V.S. conducted the synchrotron experiments with support of J.B.

Additional Information

Competing Interests: The authors declare that they have no competing interests.

Publisher's note: Springer Nature remains neutral with regard to jurisdictional claims in published maps and institutional affiliations.



Open Access This article is licensed under a Creative Commons Attribution 4.0 International License, which permits use, sharing, adaptation, distribution and reproduction in any medium or format, as long as you give appropriate credit to the original author(s) and the source, provide a link to the Creative Commons license, and indicate if changes were made. The images or other third party material in this article are included in the article's Creative Commons license, unless indicated otherwise in a credit line to the material. If material is not included in the article's Creative Commons license and your intended use is not permitted by statutory regulation or exceeds the permitted use, you will need to obtain permission directly from the copyright holder. To view a copy of this license, visit <http://creativecommons.org/licenses/by/4.0/>.

© The Author(s) 2017

Paper II

Electronic structure based design of thin film metallic glasses with superior fracture toughness

S. Evertz, I. Kirchlechner, R. Soler, C. Kirchlechner, P. Kontis, J. Bednarcik, B. Gault, G.

Dehm, D. Raabe and J. M. Schneider

Materials and Design **186**, 108327 (2020), doi: 10.1016/j.matdes.2019.108327



Electronic structure based design of thin film metallic glasses with superior fracture toughness

Simon Evertz^{a,*}, Ines Kirchlechner^b, Rafael Soler^b, Christoph Kirchlechner^b, Paraskevas Kontis^b, Jozef Bednarcik^c, Baptiste Gault^{b,d}, Gerhard Dehm^b, Dierk Raabe^b, Jochen M. Schneider^a

^a Materials Chemistry, RWTH Aachen University, Kopernikusstr, 10, 52074 Aachen, Germany

^b Max-Planck-Institut für Eisenforschung, Max-Planck-Str. 1, 40237 Düsseldorf, Germany

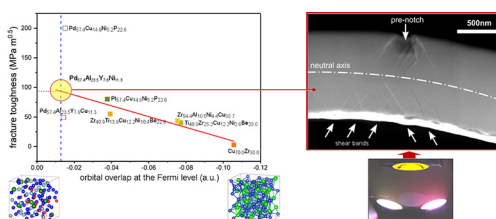
^c Department of Condensed Matter Physics, Institute of Physics, P.J. Safarik University, Park Angelinum 9, 041 54 Kosice, Slovakia

^d Department of Materials, Imperial College, South Kensington, London SW7 2AZ, United Kingdom

HIGHLIGHTS

- A model to quantitatively predict the fracture toughness based on the orbital overlap at the Fermi is introduced.
- The toughness of $\text{Pd}_{57.4}\text{Al}_{23.5}\text{Y}_{7.8}\text{Ni}_{11.3}$ metallic glass is predicted to be $95 \pm 20 \text{ MPa} \cdot \text{m}^{0.5}$
- $\text{Pd}_{57.4}\text{Al}_{23.5}\text{Y}_{7.8}\text{Ni}_{11.3}$ metallic glasses show pronounced plasticity and absence of crack growth in micro-mechanical cantilever bending experiments consistent with the predicted toughness.

GRAPHICAL ABSTRACT



ARTICLE INFO

Article history:

Received 19 July 2019

Received in revised form 31 October 2019

Accepted 2 November 2019

Available online 06 November 2019

Keywords:

Metallic glass

Ab initio

Fracture toughness

Chemical bonding

ABSTRACT

High fracture toughness is crucial for the application of metallic glasses as structural materials to avoid catastrophic failure of the material in a brittle manner. One fingerprint for fracture toughness in metallic glasses is the fraction of hybridized bonds, which is affected by alloying $\text{Pd}_{57.4}\text{Al}_{23.5}\text{Y}_{7.8}\text{M}_{11.3}$ with $\text{M} = \text{Fe}, \text{Ni}, \text{Co}, \text{Cu}, \text{Os}, \text{Ir}, \text{Pt}, \text{and Au}$. It is shown that experimental fracture toughness data is correlated to the fraction of hybridized bonds which scale with the localized bonds at the Fermi level. Thus, the localized bonds at the Fermi level are utilized quantitatively as a measure for fracture toughness. Based on *ab initio* calculations, the minimum fraction of hybridized bonds was identified for $\text{Pd}_{57.4}\text{Al}_{23.5}\text{Y}_{7.8}\text{Ni}_{11.3}$. According to the ansatz that the crystal orbital overlap population at the Fermi level scales with fracture toughness, for $\text{Pd}_{57.4}\text{Al}_{23.5}\text{Y}_{7.8}\text{Ni}_{11.3}$ a value of around $95 \pm 20 \text{ MPa} \cdot \text{m}^{0.5}$ is predicted quantitatively for the first time. Consistent with this prediction, in micro-mechanical beam bending experiments $\text{Pd}_{57.4}\text{Al}_{23.5}\text{Y}_{7.8}\text{Ni}_{11.3}$ thin films show pronounced plasticity and absence of crack growth.

© 2018 The Authors. Published by Elsevier Ltd. This is an open access article under the CC BY license (<http://creativecommons.org/licenses/by/4.0/>).

1. Introduction

Some metallic glasses envisaged for mechanical applications have a high strength [1–3] and show the capability of plastic deformation,

especially in geometries confined to the size of the plastic zone [4,5], which can be in the range of millimeters [6]. Plasticity in metallic glasses is especially reported to occur under bending load [7–10]. Lewandowski et al. put the Poisson's ratio ν forward as a design criterion for brittleness and toughness by reporting a brittle to ductile transition at $\nu = 0.31$ – 0.32 [11]. However, as this brittle to ductile transition is not universal [9,12,13], Schnabel et al. proposed the fraction of hybridized

* Corresponding author.

E-mail address: evertz@mch.rwth-aachen.de (S. Evertz).

bonds compared to the overall bonding as an electronically motivated measure for high fracture toughness [12] as covalent bonding induces brittleness in metallic glasses [10,14]. Decreasing the fraction of hybridized bonds [12] is therefore proposed to serve as a guideline for increasing fracture toughness. Based on this approach the high fracture toughness of $49.0 \text{ MPa} \cdot \text{m}^{0.5}$ reported for a $\text{Pd}_{57.0}\text{Al}_{23.5}\text{Y}_{7.7}\text{Cu}_{11.4}$ glass can be rationalized by a comparative analysis of densities of states and bonding with brittle metallic glass systems such as $\text{Cu}_{69.6}\text{Zr}_{30.4}$ [12]. For the design of tough metallic glasses, Schnabel's proposal lacks, however, predictive capability since a quantitative relationship between fracture toughness and electronic structure has not been established so far.

Hence, the quantitative model to predict the fracture toughness of metallic glasses based on the fraction of hybridized bonds presented here enables the quantitative prediction of fracture toughness of metallic glasses for the first time. In this model, the crystal orbital overlap population [15] at the Fermi level is utilized as a measure to quantify localized bonds. By correlating the localized bonds with fracture toughness values reported in literature, the fracture toughness of $\text{Pd}_{57.4}\text{Al}_{23.5}\text{Y}_{7.8}\text{Ni}_{11.3}$ is predicted. The prediction from this quantitative model is validated experimentally. Due to its fracture toughness of $49.0 \text{ MPa} \cdot \text{m}^{0.5}$ reported by Schnabel et al. [12], the $\text{Pd}_{57.0}\text{Al}_{23.9}\text{Y}_{7.7}\text{Cu}_{11.4}$ metallic glass is chosen as a reference and $\text{Pd}_{57.0}\text{Al}_{23.9}\text{Y}_{7.7}\text{M}_{11.4}$ ($\text{M} = \text{Fe}, \text{Ni}, \text{Os}, \text{Ir}, \text{Pt}, \text{and Au}$) as the model system with the aim to understand the relationship between electronic structure and fracture toughness by quantification of the fraction of hybridized bonds.

2. Methods

2.1. *Ab initio* calculations

The electronic structure of metallic glasses is the basis for the quantitative model introduced here to predict fracture toughness. To investigate the electronic structure of $\text{Pd}_{57.0}\text{Al}_{23.9}\text{Y}_{7.7}\text{M}_{11.4}$ metallic glasses, *ab initio* molecular dynamics calculations were carried out in this study to determine the fraction of hybridized bonds. Therefore, the density functional theory [16] based openMX code [17,18] was used by employing electronic potentials with the generalized gradient approximation [19]. The following linear combinations of localized pseudoatomic orbitals [20] were applied as basis functions: $\text{Pd}5.0\text{-s}2\text{p}1\text{d}1$, $\text{Al}6.0\text{-s}2\text{p}2$, $\text{Y}6.5\text{-s}3\text{p}2\text{d}1$, $\text{Ni}6.0\text{-s}2\text{p}2\text{d}2\text{f}1$, $\text{Au}8.0\text{-s}2\text{p}2\text{d}1$, $\text{Co}5.5\text{-s}2\text{p}1\text{d}1$, $\text{Ir}7.0\text{-s}2\text{p}2\text{d}2\text{f}1$, $\text{Cu}4.5\text{-s}1\text{p}1\text{d}1$, $\text{Os}7.0\text{-s}2\text{p}2\text{d}2\text{f}1$, $\text{Fe}5.0\text{-s}1\text{p}2\text{d}1$, $\text{Pt}7.0\text{-s}2\text{p}2\text{d}2\text{f}1$. Thereby, the first symbol designates the chemical element followed by the cutoff-radius of the potential in Bohr radii. The last set of symbols defines the primitive orbitals. A grid of $85 \times 85 \times 85$ N-points and a cutoff energy of 150 Ry have been used. The Vienna *Ab initio* Simulation Package (VASP) [21,22] was employed for volume relaxation at 0 K. Therefore, ultrasoft pseudopotentials were employed and the Brillouin zone was integrated at a $3 \times 3 \times 3$ Monkhorst-Pack *k*-point grid [23]. For the calculation of the electronic structure, projector augmented-wave potentials [22,24] were utilized. The Crystal Orbital Overlap Populations (COOP) [15] and Crystal Hamilton Overlap Populations (COHP) [25] were calculated by the projection of the wavefunction onto localized orbitals using the LOBSTER code (version 2.2.1) [26–28], taking all atomic orbitals in the supercell into account. For visualization, all atomic interactions within the first coordination shell of every atom are considered. To generate glassy structures comparable to experimental samples, the procedure introduced by Hostert et al. [29] was applied. Thereby, a supercell of 115 atoms was heated for 400 fs to 4000 K by scaling the velocities and then quenched to 0 K. Afterwards the volume of the structure was relaxed. The heating-quenching-relaxation cycle was repeated until the volume difference between two subsequent cycles was lower than 2%. To obtain the bulk modulus, the volume-energy data were fitted with the Birch-Murnaghan equation of state [30]. From the atomic positions, the reduced pair distribution function (PDF) $g(r)$ was calculated [29].

2.2. Sample synthesis and characterization

Metallic glass thin films were synthesized by magnetron sputtering from elemental targets on silicon and NaCl-substrates in DC mode in an ultra-high vacuum combinatorial growth system [31] with a base pressure lower than $8 \cdot 10^{-5}$ Pa. The substrate potential was kept floating and no intentional heating was applied. The target to substrate distance was 10 cm. For silicon substrates, no sample rotation was applied to achieve Pd—Ni and Al—Y gradients, from which the position with the calculated composition was selected. For NaCl-substrates, the sample was rotated with 30 rounds per minute to obtain a homogeneous film. The power densities at the targets were 4.2, 4.8, 1.7 and 1.3 W/cm^2 for Pd, Al, Y, and Ni, respectively. Ar was the working gas with a pressure of 0.4 Pa during sputtering [12]. After deposition, the NaCl substrates were dissolved in water, to obtain thin film flakes which were cleaned in isopropanol and acetone prior to the synchrotron measurements. Thin films deposited onto silicon substrates were used for micromechanical testing.

High energy X-ray diffraction (HEXRD) was carried out at beamline P02.1 [32] of the PETRA III electron storage ring at DESY, Hamburg, Germany. X-rays with a wavelength of 0.20701 \AA were utilized. Data were collected with a Perkin Elmer XRD1621 fast detector and processed by applying the FIT2D software [33–35]. The data were corrected for background scattering and the structure factor as well as pair distribution functions calculated by a fast Fourier transformation implemented in the PDFgetX3 software package [36]. The composition of the sample was investigated with an EDAX Genesis 2000 detector on a JEOL JSM-6480 scanning electron microscope. The electronic structure was explored by X-ray photoelectron spectroscopy in a JEOL JAMP 9500F Field Emission Auger microprobe.

The fracture toughness was evaluated using pre-notched micro specimens [37–39] produced *via* focused ion beam (FIB) milling in a Zeiss Auriga® Dual Beam FIB from $1 \mu\text{m}$ thick metallic glass thin films deposited onto Si substrates. Single cantilever bending on pre-notched specimen was used to reduce the possible impact of residual stresses [40]. The ion beam current was sequentially reduced from 2 nA to 50 pA for notching. The nominal dimensions of the cantilever were $1 \times 1 \times 10 \mu\text{m}^3$ with a crack length of 200 nm and a final bending length of $6 \mu\text{m}$ to meet the geometric requirements [41,42] on the used geometry factors. Subsequently, four samples were tested in a Zeiss Gemini 500 field emission scanning electron microscope equipped with an Asmec Unat II *in situ* indenter. The indenter operates in an intrinsic displacement controlled mode [43]. Numerous unloading segments were introduced to the applied displacement function to evaluate crack propagation *via* the unloading stiffness following the small scale approach of Wurster et al. [44]. While small scale fracture tests are not in full geometric accordance with the ASTM K_{IC} measurement standard, reproducible values for fracture toughness are obtained and reported here as K_Q [43].

Atom probe tomography (APT) specimens were prepared from the center of the metallic glass thin film deposited on a silicon substrate using an FEI Helios 600 following procedures described in Ref. [45]. APT measurements were carried out on a Cameca LEAP 3000× HR operated in voltage mode at a pulse repetition rate of 200 kHz, a pulse rate of 15% and the base temperature was set to 60 K. Data analysis was performed using the IVAS 3.8.2 software package.

3. Results and discussion

$\text{Pd}_{57.4}\text{Al}_{23.5}\text{Y}_{7.8}\text{Cu}_{11.3}$ was reported by Schnabel et al. [12] to exhibit a fracture toughness of $49 \text{ MPa} \cdot \text{m}^{0.5}$. Thus, $\text{Pd}_{57.4}\text{Al}_{23.5}\text{Y}_{7.8}\text{Cu}_{11.3}$ was selected as a reference system in the present study. To investigate the composition dependence of the fraction of localized bonds on the overall bonding, Cu in $\text{Pd}_{57.4}\text{Al}_{23.5}\text{Y}_{7.8}\text{Cu}_{11.3}$ has been substituted by Fe, Ni, Co, Os, Ir, Pt, and Au, *i.e.* by screening group 8–11 elements in the 4th and 6th period of the periodic table of elements. In the following, the

results of the *ab initio* calculations are presented. Based on the calculated electronic structure and fracture toughness data from literature, a quantitative model to predict the fracture toughness is introduced. Thereafter, the theoretical atomic scale topology is contrasted to experimental data. Finally, the predicted fracture toughness data and results of micro-mechanical bending tests are compared to critically appraise the prediction.

The total and partial electronic densities of states (DOS) of $\text{Pd}_{57.4}\text{Al}_{23.5}\text{Y}_{7.8}\text{M}_{11.3}$ ($M = \text{Cu, Ir, Au, Ni}$) are presented in Fig. 1 for the energy range of -10 to 0 eV below the Fermi level. The total DOS consist of the sum of the partial DOS of every atom in the supercell of the calculation. The partial DOS contains the summed DOS of all atoms of a certain species. For the partial DOS, the DOS for the s, p and d bands are shown separately to differentiate the individual orbital contributions. The DOS are smoothed by adjacent averaging with a smooth window of 7 data points to enhance clarity. Fig. 1a shows the DOS for the reference material $\text{Pd}_{57.4}\text{Al}_{23.5}\text{Y}_{7.8}\text{Cu}_{11.3}$ [12]. By comparing peak positions and shapes for the main constituents Pd and Al between -5 and -2 eV weak p-d hybridization as well as weak s-d hybridization around -6 eV is observed. While the Y d-band shows only minor overlap with the Pd d-band, strong d-d hybridization between Cu and Pd is present over the complete energy range of -6 to 0 eV populated in the Cu DOS.

Following the approach of Schnabel et al. [12], the hybridizing constituent Cu in the reference $\text{Pd}_{57.4}\text{Al}_{23.5}\text{Y}_{7.8}\text{Cu}_{11.3}$ was substituted in the simulations by Ir, Fe, Os, Pt, Au, Ni to identify a less hybridizing constituent. All compositions discussed here have in common that the main

alloy constituents Pd and Al show weak pd- and sd-hybridization between -6 and -2 eV and that the Y d-band overlaps only slightly with other bands (Fig. 1b–d), as has already been discussed for the reference material above. Therefore, the focus will be on the differences induced by the Cu-substituting element.

The partial DOS of $\text{Pd}_{57.4}\text{Al}_{23.5}\text{Y}_{7.8}\text{Ir}_{11.3}$ (Fig. 1b) resemble those of $\text{Pd}_{57.4}\text{Al}_{23.5}\text{Y}_{7.8}\text{Cu}_{11.3}$. The Ir d-states are more evenly distributed between -6 eV and the Fermi level compared to Cu (Fig. 1a). But as for $\text{Pd}_{57.4}\text{Al}_{23.5}\text{Y}_{7.8}\text{Cu}_{11.3}$, hybridization is evident from the partial DOS of the Ir and Pd d-bands. This type of electronic structure of $\text{Pd}_{57.4}\text{Al}_{23.5}\text{Y}_{7.8}\text{Ir}_{11.3}$ and $\text{Pd}_{57.4}\text{Al}_{23.5}\text{Y}_{7.8}\text{Cu}_{11.3}$ is representative for $\text{Pd}_{57.4}\text{Al}_{23.5}\text{Y}_{7.8}\text{M}_{11.3}$ alloyed with $M = \text{Fe, Os, and Pt}$ (Fig. S1 in the supplementary information).

In contrast to $\text{Pd}_{57.4}\text{Al}_{23.5}\text{Y}_{7.8}\text{Cu}_{11.3}$, the energy range populated by the Au d-band between -6 and -2 eV in $\text{Pd}_{57.4}\text{Al}_{23.5}\text{Y}_{7.8}\text{Au}_{11.3}$ (Fig. 1c) is rather narrow and only weak hybridization with the Pd d-band is found between -6 and -4 eV. In this energy range, however, the total DOS is dominated by the Au d-band. Around -4 eV, sd-hybridization is observed between Al and Au. Due to the small overlap of the Au d-band with the populated states of the other constituents and its domination of the total DOS between -6 and -4 eV, Au should be a suitable candidate element for the substitution of Cu in $\text{Pd}_{57.4}\text{Al}_{23.5}\text{Y}_{7.8}\text{Cu}_{11.3}$ to obtain a metallic glass with high fracture toughness through a low fraction of hybridized bonds.

In the DOS of $\text{Pd}_{57.4}\text{Al}_{23.5}\text{Y}_{7.8}\text{Ni}_{11.3}$ (Fig. 1d), the Ni d-band populates a small energy range between -4 eV and 0 eV similar to

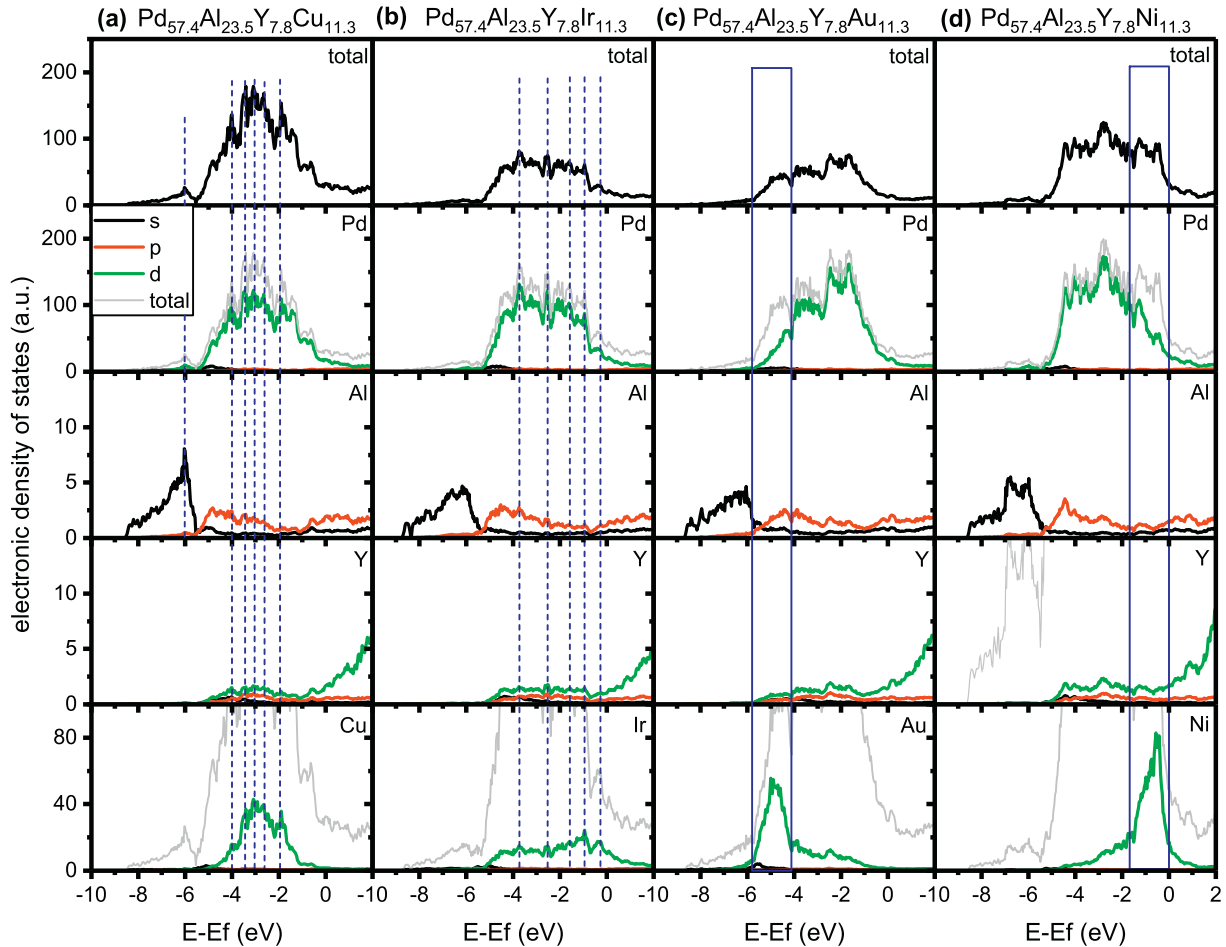


Fig. 1. Total and partial DOS of $\text{Pd}_{57.4}\text{Al}_{23.5}\text{Y}_{7.8}\text{M}_{11.3}$ ($M = \text{Cu, Ir, Au, Ni}$) (a) DOS of reference metallic glass $\text{Pd}_{57.4}\text{Al}_{23.5}\text{Y}_{7.8}\text{Cu}_{11.3}$ and metallic glasses where Cu is replaced by (b) Ir, (c) Au and (d) Ni. The top panels show the total DOS. In the panels of the partial DOS, the states of the s, p and d band are shown with black, red and green lines respectively. The grey line represents the total DOS to relate the partial DOS to the total DOS. In the case of the Ni-containing alloy, the different spin orientations due to spin polarization are summarized. The Fermi-level is shifted to 0 eV. Blue dashed lines indicate hybridization, blue boxes the dominance of the partial DOS of the M elements and are a guide for the eye. (For interpretation of the references to color in this figure legend, the reader is referred to the web version of this article.)

$\text{Pd}_{57.4}\text{Al}_{23.5}\text{Y}_{7.8}\text{Au}_{11.3}$. In this energy range, the Pd d-band becomes less populated, which leads to less hybridization while the Ni d-band dominates the total DOS. In contrast to $\text{Pd}_{57.4}\text{Al}_{23.5}\text{Y}_{7.8}\text{Au}_{11.3}$, due to the vicinity to the Fermi level, the hybridizing states of Ni form weaker bonds compared to the hybridizing states of Au in $\text{Pd}_{57.4}\text{Al}_{23.5}\text{Y}_{7.8}\text{Au}_{11.3}$ that are located at lower energies [15].

Based on the qualitative DOS analysis above, Ni is identified as the most promising candidate to substitute Cu in $\text{Pd}_{57.4}\text{Al}_{23.5}\text{Y}_{7.8}\text{Cu}_{11.3}$ with respect to fracture toughness. While Ir hybridizes strongly with Pd, Au populates only a narrow energy range around -6 eV. However, Ni shows qualitatively the lowest fraction of hybridized bonds on the overall bonding of the transition metals studied here and the hybridizing states of Ni form weak bonds due to the vicinity to the Fermi level [15], thereby promoting shear relaxation.

The bonding and anti-bonding contributions in the Pd-based metallic glass were investigated by the COHP depicted in Fig. 2a. The COHP of $\text{Pd}_{57.4}\text{Al}_{23.5}\text{Y}_{7.8}\text{Ir}_{11.3}$ is smoothed by a Savitzky-Golay [46] filter to enhance the clarity of the graphical representation. According to Rempp [47], these oscillations for $\text{Pd}_{57.4}\text{Al}_{23.5}\text{Y}_{7.8}\text{Ir}_{11.3}$ could

be caused by the energy difference between the Ir d- and both s- and p-bands.

Fig. 2a shows, that the COHPs of the Pd-based metallic glasses from Fig. 1 resemble each other. Below approximately -2.4 eV, the COHPs are negative, indicating bonding contributions to the overall bonding. Above -2.4 eV, all Pd-based metallic glasses show anti-bonding contributions to the bonding. Comparing the COHPs of $\text{Pd}_{57.4}\text{Al}_{23.5}\text{Y}_{7.8}\text{Ir}_{11.3}$ to the reference system $\text{Pd}_{57.4}\text{Al}_{23.5}\text{Y}_{7.8}\text{Cu}_{11.3}$, a slight shift of the COHP above -2.8 eV towards the Fermi level is identified, while it resembles the reference COHP of $\text{Pd}_{57.4}\text{Al}_{23.5}\text{Y}_{7.8}\text{Cu}_{11.3}$ below -2.8 eV. The resulting higher population of anti-bonding states at the Fermi-level indicates weaker bonding. $\text{Pd}_{57.4}\text{Al}_{23.5}\text{Y}_{7.8}\text{Au}_{11.3}$ exhibits fewer bonding contributions than the reference $\text{Pd}_{57.4}\text{Al}_{23.5}\text{Y}_{7.8}\text{Cu}_{11.3}$ between -5 and -3.3 eV, which is part of the energy range dominated by the Au d-band, while its anti-bonding states resemble the reference material. Thus, the lower population of bonding states and the lower fraction of hybridized bonds observed in Fig. 1 results in weaker localized bonds between -5 and -3.3 eV, which may, in turn, enable shear relaxation upon mechanical loading. In contrast to this, the COHP of

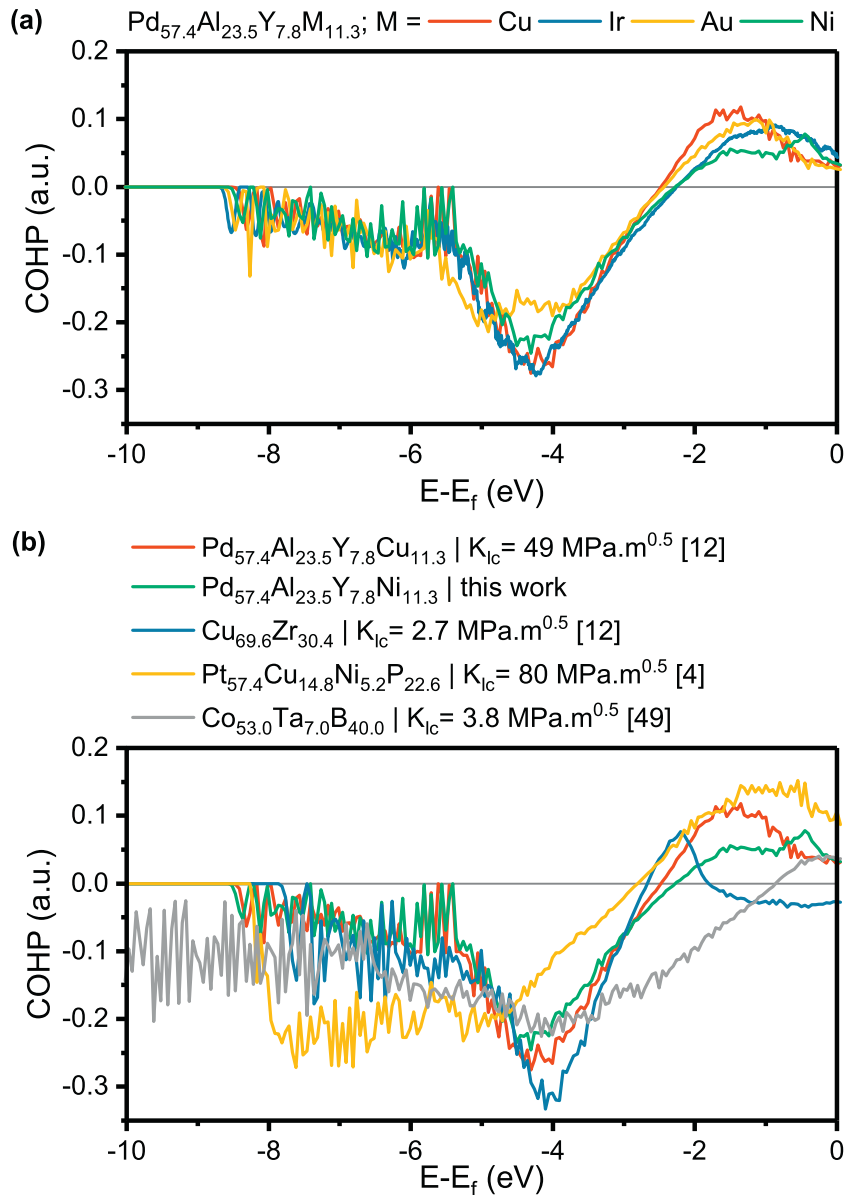


Fig. 2. Crystal Orbital Hamilton Populations (COHP) of (a) $\text{Pd}_{57.4}\text{Al}_{23.5}\text{Y}_{7.8}\text{M}_{11.3}$ ($M = \text{Cu, Ir, Au, Ni}$) metallic glasses shown on Fig. 1 and (b) selected $\text{Pd}_{57.4}\text{Al}_{23.5}\text{Y}_{7.8}\text{M}_{11.3}$ in comparison with $\text{Cu}_{69.6}\text{Zr}_{30.4}$ [12], $\text{Pt}_{57.4}\text{Cu}_{14.8}\text{Ni}_{5.2}\text{P}_{22.6}$ [4] and $\text{Co}_{53.0}\text{Ta}_{7.0}\text{B}_{40.0}$ [49] metallic glasses.

$\text{Pd}_{57.4}\text{Al}_{23.5}\text{Y}_{7.8}\text{Ni}_{11.3}$ resembles the COHP of the reference material in the bonding region, while the anti-bonding contributions are smaller than the reference and shifted to the Fermi-level similar to $\text{Pd}_{57.4}\text{Al}_{23.5}\text{Y}_{7.8}\text{Ir}_{11.3}$. Taking into account the integrated COHP (ICOHP) as a measure of bond strength [48], $\text{Pd}_{57.4}\text{Al}_{23.5}\text{Y}_{7.8}\text{Ni}_{11.3}$ exhibits weaker bonding than $\text{Pd}_{57.4}\text{Al}_{23.5}\text{Y}_{7.8}\text{Au}_{11.3}$ as its ICOHP of -0.509 eV is less negative and hence indicates weaker bond strength than -0.589 eV for $\text{Pd}_{57.4}\text{Al}_{23.5}\text{Y}_{7.8}\text{Au}_{11.3}$, which is consistent with the qualitative DOS analysis above.

Comparing the COHP of $\text{Pd}_{57.4}\text{Al}_{23.5}\text{Y}_{7.8}\text{Cu}_{11.3}$ and $\text{Pd}_{57.4}\text{Al}_{23.5}\text{Y}_{7.8}\text{Ni}_{11.3}$ with the COHP of brittle $\text{Cu}_{69.6}\text{Zr}_{30.4}$ [12], the similarly tough but nearly twice as strong $\text{Co}_{53.0}\text{Ta}_{7.0}\text{B}_{40.0}$ [49] and tough $\text{Pt}_{57.4}\text{Cu}_{14.8}\text{Ni}_{5.2}\text{P}_{22.6}$ [4] shows that $\text{Pd}_{57.4}\text{Al}_{23.5}\text{Y}_{7.8}\text{Ni}_{11.3}$ is similar to the Pt-based metallic glass. Contrary to $\text{Pd}_{57.4}\text{Al}_{23.5}\text{Y}_{7.8}\text{Ni}_{11.3}$, $\text{Pt}_{57.4}\text{Cu}_{14.8}\text{Ni}_{5.2}\text{P}_{22.6}$ exhibits more bonding states between -8 and

-5 eV and at the same time more anti-bonding states close to the Fermi level. Due to the presence of stronger bonding states below -5 eV, $\text{Pt}_{57.4}\text{Cu}_{14.8}\text{Ni}_{5.2}\text{P}_{22.6}$ is expected to be more shear resistant than $\text{Pd}_{57.4}\text{Al}_{23.5}\text{Y}_{7.8}\text{Ni}_{11.3}$. Nevertheless, as the COHP of $\text{Pt}_{57.4}\text{Cu}_{14.8}\text{Ni}_{5.2}\text{P}_{22.6}$ and $\text{Pd}_{57.4}\text{Al}_{23.5}\text{Y}_{7.8}\text{Ni}_{11.3}$ are similar, also the fracture toughness is expected to be similar. The brittle $\text{Cu}_{69.6}\text{Zr}_{30.4}$, in contrast, exhibits anti-bonding states only between -2 and -3 eV and hence bonding states close to the Fermi level, indicating strong, hybridized bonds. The COHP of $\text{Co}_{53.0}\text{Ta}_{7.0}\text{B}_{40.0}$ contains a broad energy range populated by bonding states, anti-bonding states are only present above -1 eV close to the Fermi level. Due to the larger amount of bonding contributions and thus stronger hybridized bonding, the shear resistance in the latter two glasses is predicted to be larger compared to $\text{Pt}_{57.4}\text{Cu}_{14.8}\text{Ni}_{5.2}\text{P}_{22.6}$ and the Pd-based glasses. This prediction is consistent with the brittle behavior reported for $\text{Cu}_{69.6}\text{Zr}_{30.4}$ [12] and

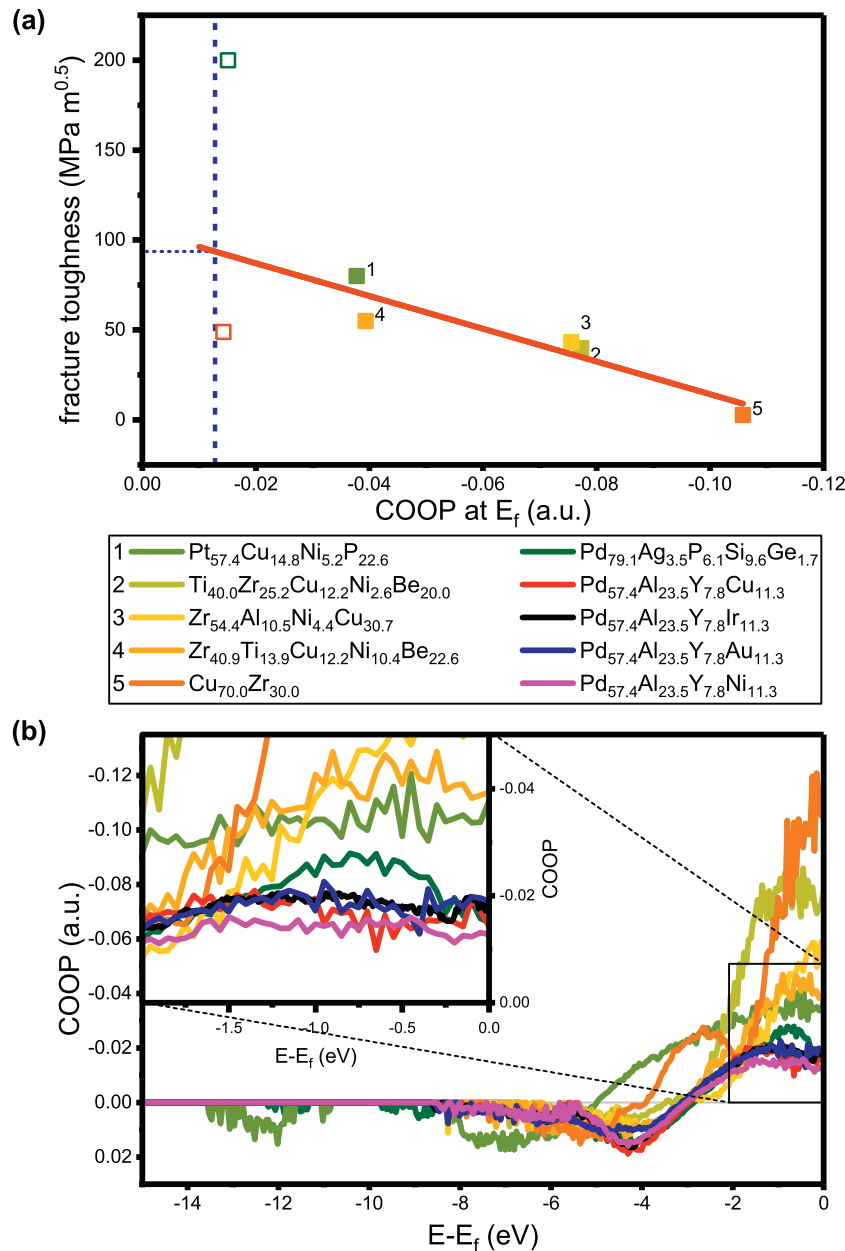


Fig. 3. (a) Fracture toughness as a function of COOP at the Fermi level. Values for fracture toughness were obtained from literature [4,50–54] and COOP calculated by *ab initio* methods. The solid red line represents a linear fit. The blue dashed line marks the COOP at E_f of $\text{Pd}_{57.4}\text{Al}_{23.5}\text{Y}_{7.8}\text{Ni}_{11.3}$. Dotted blue lines mark the minimum and maximum predicted fracture toughness values of $\text{Pd}_{57.4}\text{Al}_{23.5}\text{Y}_{7.8}\text{Ni}_{11.3}$. Note that the fracture toughness of all glasses included in the fit was obtained under similar loading conditions. (b) COOP of metallic glasses from (a) including glasses from Fig. 1. Negative values indicate anti-bonding contributions, positive values bonding contributions. The inset is a magnification of the marked region close to the Fermi level. (For interpretation of the references to color in this figure legend, the reader is referred to the web version of this article.)

$\text{Co}_{53.0}\text{Ta}_{7.0}\text{B}_{40.0}$ [49] in contrast to the plastic behavior reported for $\text{Pt}_{57.4}\text{Cu}_{14.8}\text{Ni}_{5.2}\text{P}_{22.6}$ [4] tested under bending load with slightly different sample sizes [4,12,49].

Above, Ni was identified as the most promising element to substitute Cu in $\text{Pd}_{57.4}\text{Al}_{23.5}\text{Y}_{7.8}\text{Cu}_{11.3}$ to improve fracture toughness. Here, the orbital overlap at the Fermi level is investigated to predict the fracture toughness quantitatively. We assume that for glasses with a low fraction of localized and hence hybridized bonds the balance to the overall bonding is given by metallic bonds. Thus, the ideal glass in terms of toughness exhibits metallic bonds only. By means of Crystal Orbital Overlap Population (COOP) and COHP, it is possible to characterize localized bonding [25], but not metallic bonding directly. Therefore, the fraction of metallic bonding is described indirectly by the absence of localized bonds. Focusing hence on the orbital overlap by means of the COOP, for ideal metallic bonding no localized bond overlap and thus a value of 0 for the COOP at the Fermi level is expected, as all electrons are shared in an electron gas. Due to the pronounced metallic bonding character consistent with the absence of hybridized bonds, a high fracture toughness is expected for metallic glasses with a low COOP at the Fermi level.

The fracture toughness of non-magnetic metallic glasses reported in literature [4,50–54] is presented in Fig. 3a) as a function of the COOP at the Fermi level. Therefore, we use the same data set for fracture toughness as Demetriou et al. [50] expanded by the data from Schnabel et al. [12]. These data are fitted by a linear fit excluding fracture toughness values of $\text{Pd}_{79.1}\text{Ag}_{3.5}\text{P}_{6.1}\text{Si}_{9.6}\text{Ge}_{1.7}$ and $\text{Pd}_{57.4}\text{Al}_{23.5}\text{Y}_{7.8}\text{Cu}_{11.3}$, as these data may be affected by sample size: The fracture toughness of $\text{Pd}_{79.1}\text{Ag}_{3.5}\text{P}_{6.1}\text{Si}_{9.6}\text{Ge}_{1.7}$ might be overestimated because the plastic zone size of 6 mm is larger than the actual sample size [50] of $2.1 \times 2.1 \times 20 \text{ mm}^3$ in two dimensions [5]. Fracture toughness of $\text{Pd}_{57.4}\text{Al}_{23.5}\text{Y}_{7.8}\text{Cu}_{11.3}$ is determined by the J-integral and might be sample size dependent [12]. The COOP at the Fermi level of $\text{Pd}_{57.4}\text{Al}_{23.5}\text{Y}_{7.8}\text{Ni}_{11.3}$ is indicated by a dashed blue line. Based on the intersection of the dashed blue line with the fit, the fracture toughness of $\text{Pd}_{57.4}\text{Al}_{23.5}\text{Y}_{7.8}\text{Ni}_{11.3}$ is predicted to be around $95 \pm 20 \text{ MPa} \cdot \text{m}^{0.5}$. Comparing this prediction with the Ashby map reported by Demetriou et al. [50], this predicted fracture toughness corresponds to a plastic zone size in the orders of 0.1 to 1 mm [50]. Furthermore, this analysis shows that in addition to the presence of localized bonds, also anti-bonding states at the Fermi level must be considered for the design of tough metallic glasses. Antibonding states increase the total bond energy and thus promote bond separation [55] and hence favor brittle behavior of metallic glasses. Due to the promotion of bond separation, not only the fracture toughness is affected by anti-bonding states, but also the cohesive energy and hence the elastic properties (cf. Fig. S2). The free volume in *ab initio* calculations is small and different free volume configurations were not tested. Hence, the free volume content is smaller than it might be in physical samples, as shown in Fig. 4 below. However, as a larger amount of free volume promotes fracture toughness by lowering the energy barrier for shear transformation and plastic deformation [56], the fracture toughness predicted based on the electronic structure serves as a lower bound while free volume affects the variability of fracture toughness observed in Fig. 3a.

The COOP of the glasses presented in Figs. 1 and 3a) are shown in Fig. 3b). While all material systems exhibit a transition between bonding and anti-bonding states between -5 and -3 eV, the amount of anti-bonding states close to the Fermi level differs significantly. It is evident that the difference between the COOPs depends mainly on the major constituent of the alloys. The difference between the Pd-based metallic glasses is hence rather small (inset Fig. 3b). Nevertheless, $\text{Pd}_{57.4}\text{Al}_{23.5}\text{Y}_{7.8}\text{Ni}_{11.3}$ clearly exhibits the smallest population of anti-bonding states at the Fermi level ($\text{COOP}(E_f)_{\text{Ni}} = -0.01278$), whereas $\text{Pd}_{57.4}\text{Al}_{23.5}\text{Y}_{7.8}\text{Au}_{11.3}$ – from a qualitative point of view (Fig. 1) also interesting – displays a larger population of anti-bonding states at the Fermi level ($\text{COOP}(E_f)_{\text{Au}} = -0.01901$). Therefore, the predicted fracture toughness of approximately $95 \pm 20 \text{ MPa} \cdot \text{m}^{0.5}$ of

$\text{Pd}_{57.4}\text{Al}_{23.5}\text{Y}_{7.8}\text{Ni}_{11.3}$ is the largest within the here considered group of metallic glasses.

Since the Ni-containing Pd-based metallic glass is the most promising candidate in terms of fracture toughness, this composition was synthesized by magnetron sputtering in the form of a $\text{Pd}_{57.9}\text{Al}_{25.0}\text{Y}_{4.9}\text{Ni}_{12.2}$ thin film on silicon and $\text{Pd}_{62.1}\text{Al}_{27.3}\text{Y}_{4.2}\text{Ni}_{6.4}$ for the thin film flakes. The constituents are homogeneously distributed based on the frequency distribution analysis performed on data collected by atom probe tomography (see Fig. S3 in supplementary information). Hence, chemical inhomogeneities on the here probed length scale cannot be revealed by atom probe tomography. To critically appraise the predicted topology, the calculated pair distribution function is compared to the experimentally obtained one in Fig. 4a. Considering the slight differences between the composition of the powder and the calculation, the pair distribution functions are in reasonable agreement. However, the first peak of the experimental pair distribution function is shifted to a larger bond distance compared to the theoretical one. This indicates that the synthesized material is less frustrated, most likely due to the presence of free volume. As the energy barrier for shear transformation and thus plastic deformation, which is required for high fracture toughness, decreases with increasing free volume content in the sample [56], the plastic deformation behavior of the experimental sample is expected to be more enhanced than predicted with the fracture toughness predicted serving as a lower bound. Fig. 4b compares the theoretical DOS with the experimental DOS. Due to the high energy of the X-rays in the XPS (1.49 keV) as well as the temperature in the experiment (298 K in experiment vs. 0 K in the calculation), the experimental DOS experiences severe peak broadening. Thereby, one broad hump is observed for the valence band, that covers the energy range of the more detailed theoretical DOS. The comparison between calculated and measured topology and electronic structure confirms the significance of the *ab initio* modeled structure.

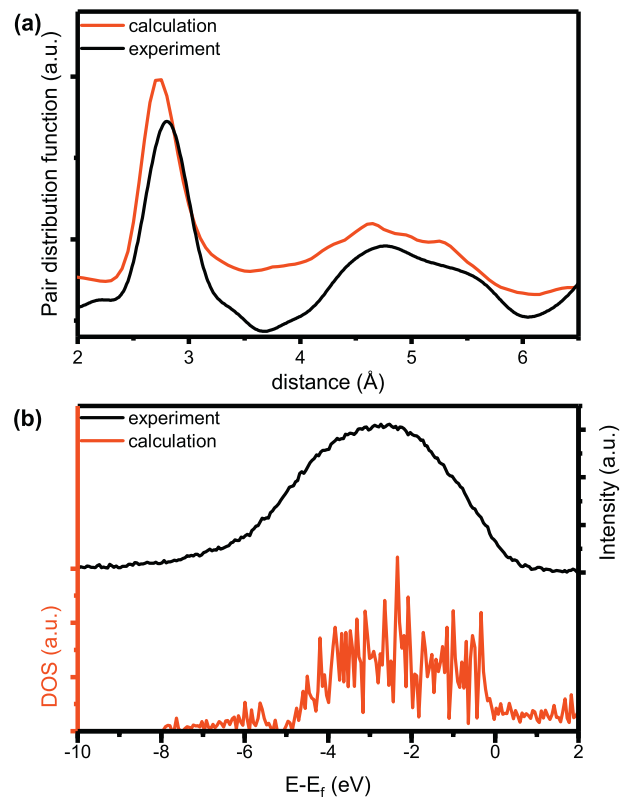


Fig. 4. (a) Calculated and experimental pair distribution function of $\text{Pd}_{57.4}\text{Al}_{23.5}\text{Y}_{7.8}\text{Ni}_{11.3}$ and $\text{Pd}_{62.1}\text{Al}_{27.3}\text{Y}_{4.2}\text{Ni}_{6.4}$, respectively. The experimental PDF has already been published in [57]. (b) Calculated density of states of $\text{Pd}_{57.4}\text{Al}_{23.5}\text{Y}_{7.8}\text{Ni}_{11.3}$ and the valence band of $\text{Pd}_{62.1}\text{Al}_{27.3}\text{Y}_{4.2}\text{Ni}_{6.4}$ measured by XPS.

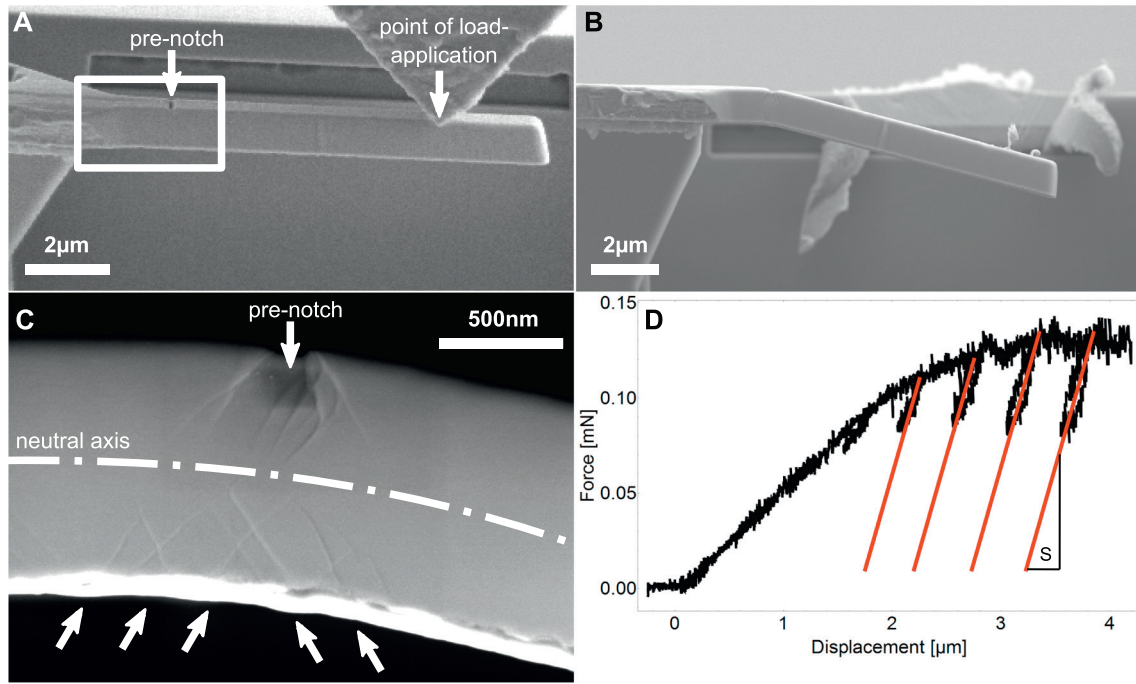


Fig. 5. (a) Snapshot of $\text{Pd}_{57.9}\text{Al}_{25.0}\text{Y}_{4.9}\text{Ni}_{12.2}$ micro cantilever during *in situ* loading. (b) *Post mortem* microbeam after $4\ \mu\text{m}$ deflection. (c) Detail in-lense-SE micrograph of the region highlighted in (a). Huge shear bands are formed at the location of the pre-notch. The arrows indicate the additional formation of shear bands at the compression side of the cantilever. (d) Force versus displacement raw-data. The unloading stiffness (S shown in red) does not significantly change during the experiment indicating an absence of substantial crack-growth. Plasticity in the vicinity of the pre-notch is observed right from the beginning resulting in a different initial loading slope compared to S . (For interpretation of the references to color in this figure legend, the reader is referred to the web version of this article.)

To investigate the fracture toughness of the $\text{Pd}_{57.9}\text{Al}_{25.0}\text{Y}_{4.9}\text{Ni}_{12.2}$ metallic glass, beams were prepared for micro-mechanical testing (Fig. 5a). The unloading slopes (S in Fig. 5d) performed after 2, 2.5, 3, and $3.5\ \mu\text{m}$ displacement do not change indicating an absence of crack extension. Also, at the final displacement of $4\ \mu\text{m}$, the beam did not fracture (Fig. 5b). In contrast, multiple shear-bands are formed not only around the pre-notch but also on the compressive side of the cantilever (Fig. 5c) indicating significant plastic deformation. The shear bands do not cross the neutral axis which indicates that shear band propagation is suppressed by the stress gradient and the change from tensile to compressive stresses across cantilever. Therefore, catastrophic shear band propagation is prevented because the suppressed shear band propagation requires the activation of new shear bands (see Fig. 5c) and allows the glass to deform plastically without catastrophic crack development [5] up to the final displacement of $4\ \mu\text{m}$. Since no evidence for crack extension was obtained in *post mortem* imaging, the fracture toughness exceeds the constraints of micromechanical fracture experiments. This is in agreement with the high fracture toughness expected from the plot in Fig. 3, which would require substantially larger samples to quantitatively proof the enormous fracture toughness [5,58]. Such sample dimensions are – in light of the chemical composition and technological constraints – currently not feasible.

4. Conclusions

Inspired by the qualitative notion of Schnabel et al. [12] that the fraction of bonds stemming from hybridized states compared to the overall bonding can be associated with damage tolerance in thin film metallic glasses, a correlation between the fraction of localized and anti-bonding bonds scaling with the crystal orbital overlap population at the Fermi level and experimental fracture toughness data is identified. It is shown that a low number of anti-bonding states at the Fermi-level is a necessary requirement for high fracture toughness. The electronic structures of $\text{Pd}_{57.4}\text{Al}_{23.5}\text{Y}_{7.8}\text{M}_{11.3}$ ($M = \text{Fe, Ni, Cu, Os, Ir, Pt, and Au}$) have been calculated by *ab initio* methods. $\text{Pd}_{57.4}\text{Al}_{23.5}\text{Y}_{7.8}\text{Ni}_{11.3}$ was identified to exhibit

the minimal fraction of hybridized bonds of the materials investigated. Moreover, the correlation between the fraction of localized anti-bonding bonds scaling with the crystal orbital overlap population at the Fermi level and experimental fracture toughness data was identified. This correlation allows the quantitative prediction of fracture toughness of metallic glasses that is crucial for the design of tough metallic glasses. With this model, the fracture toughness of $\text{Pd}_{57.4}\text{Al}_{23.5}\text{Y}_{7.8}\text{Ni}_{11.3}$ is predicted to be $95 \pm 20\ \text{MPa}\cdot\text{m}^{0.5}$, being the first fracture toughness value predicted quantitatively for a metallic glass based on the electronic structure. Consistent with this prediction, micro-mechanical beam bending experiments show that $\text{Pd}_{57.4}\text{Al}_{23.5}\text{Y}_{7.8}\text{Ni}_{11.3}$ thin films exhibit superior fracture toughness and form multiple shear bands.

CRediT authorship contribution statement

Simon Evertz: Conceptualization, Methodology, Formal analysis, Investigation, Writing - Original Draft. **Ines Kirchlechner:** Conceptualization, Methodology, Formal analysis, Investigation, Writing - Original Draft. **Rafael Soler:** Conceptualization, Methodology, Formal analysis, Investigation, Writing - Original Draft. **Christoph Kirchlechner:** Conceptualization, Methodology, Formal analysis, Investigation, Writing - Original Draft. **Paraskevas Kontis:** Conceptualization, Methodology, Formal analysis, Investigation, Writing - Original Draft. **Jozef Bednarcik:** Methodology, Formal analysis, Investigation, Writing - Original Draft. **Baptiste Gault:** Conceptualization, Methodology, Formal analysis, Writing - Original Draft. **Gerhard Dehm:** Conceptualization, Writing - Original Draft, Supervision, Funding acquisition. **Dierk Raabe:** Conceptualization, Writing - Original Draft, Supervision, Funding acquisition. **Jochen M. Schneider:** Conceptualization, Writing - Original Draft, Supervision, Funding acquisition.

Acknowledgements

We thank D. Music for fruitful discussions about the *ab initio* calculations. Financial support of the German Research Foundation within the

SPP 1594 “Topological engineering of Ultrastrong Glasses” is acknowledged (DE 796/9-2, SCHN 735/22-2, RA 123). *Ab initio* calculations were performed on the JARA-HPC Partition part of the supercomputer CLAIK at RWTH Aachen University within the project JARA0131. Parts of this research were carried out at beamline P02.1 of the light source PETRA III at DESY, a member of the Helmholtz Association (HGF).

Data availability

The raw/processed data required to reproduce these findings cannot be shared at this time due to technical or time limitations.

Declaration of competing interest

None.

Appendix A. Supplementary data

Supplementary data to this article can be found online at <https://doi.org/10.1016/j.matdes.2019.108327>.

References

- [1] M. Telford, The case for bulk metallic glass, *Mater. Today* 7 (2004) 36–43, [https://doi.org/10.1016/S1369-7021\(04\)00124-5](https://doi.org/10.1016/S1369-7021(04)00124-5).
- [2] M. Ashby, A.L. Greer, Metallic glasses as structural materials, *Scr. Mater.* 54 (2006) 321–326, <https://doi.org/10.1016/j.scriptamat.2005.09.051>.
- [3] A. Inoue, B. Shen, A. Takeuchi, Developments and applications of bulk glassy alloys in late transition metal base system, *Mater. Trans.* 47 (2006) 1275–1285, <https://doi.org/10.2320/matertrans.47.1275>.
- [4] J. Schroers, W.L. Johnson, Ductile bulk metallic glass, *Phys. Rev. Lett.* 93 (2004), 255506. <https://doi.org/10.1103/PhysRevLett.93.255506>.
- [5] B. Gludovatz, D. Granata, K.V.S. Thurston, J.F. Löffler, R.O. Ritchie, On the understanding of the effects of sample size on the variability in fracture toughness of bulk metallic glasses, *Acta Mater.* 126 (2017) 494–506, <https://doi.org/10.1016/j.actamat.2016.12.054>.
- [6] J. Schroers, Processing of bulk metallic glass, *Adv. Mater.* 22 (2010) 1566–1597, <https://doi.org/10.1002/adma.200902776>.
- [7] X.K. Xi, D.Q. Zhao, M.X. Pan, W.H. Wang, Y. Wu, J.J. Lewandowski, Fracture of brittle metallic glasses: brittleness or plasticity, *Phys. Rev. Lett.* 94 (2005), 125510. <https://doi.org/10.1103/PhysRevLett.94.125510>.
- [8] W. Chen, J. Ketkaew, Z. Liu, R.M.O. Mota, K. O'Brien, C.S. da Silva, et al., Does the fracture toughness of bulk metallic glasses scatter? *Scr. Mater.* 107 (2015) 1–4, <https://doi.org/10.1016/j.scriptamat.2015.05.003>.
- [9] Z.-d. Zhu, P. Jia, J. Xu, Optimization for toughness in metalloid-free Ni-based bulk metallic glasses, *Scr. Mater.* 64 (2011) 785–788, <https://doi.org/10.1016/j.scriptamat.2010.12.047>.
- [10] Q. He, Y.-Q. Cheng, E. Ma, J. Xu, Locating bulk metallic glasses with high fracture toughness: chemical effects and composition optimization, *Acta Mater.* 59 (2011) 202–215, <https://doi.org/10.1016/j.actamat.2010.09.025>.
- [11] J.J. Lewandowski, W.H. Wang, A.L. Greer, Intrinsic plasticity or brittleness of metallic glasses, *Philos. Mag. Lett.* 85 (2005) 77–87, <https://doi.org/10.1080/09500830500080474>.
- [12] V. Schnabel, B.N. Jaya, M. Köhler, D. Music, C. Kirchlechner, G. Dehm, et al., Electronic hybridisation implications for the damage-tolerance of thin film metallic glasses, *Sci. Rep.* 6 (2016), 36556. <https://doi.org/10.1038/srep36556>.
- [13] R. Raghavan, P. Murali, U. Ramamurty, On factors influencing the ductile-to-brittle transition in a bulk metallic glass, *Acta Mater.* 57 (2009) 3332–3340, <https://doi.org/10.1016/j.actamat.2009.03.047>.
- [14] T. Rouxel, Fracture surface energy and toughness of inorganic glasses, *Scr. Mater.* 137 (2017) 109–113, <https://doi.org/10.1016/j.scriptamat.2017.05.005>.
- [15] R. Hoffmann, How chemistry and physics meet in the solid state, *Angew. Chem. Int. Ed. Eng.* 26 (1987) 846–878, <https://doi.org/10.1002/anie.198708461>.
- [16] P. Hohenberg, W. Kohn, Inhomogeneous electron gas, *Phys. Rev.* 136 (1964) B864–B871, <https://doi.org/10.1103/PhysRev.136.B864>.
- [17] T. Ozaki, H. Kino, Numerical atomic basis orbitals from H to Kr, *Phys. Rev. B* 69 (2004), 195113. <https://doi.org/10.1103/PhysRevB.69.195113>.
- [18] T. Ozaki, H. Kino, Efficient projector expansion for the *ab initio* LCAO method, *Phys. Rev. B* 72 (2005), 045121. <https://doi.org/10.1103/PhysRevB.72.045121>.
- [19] J.P. Perdew, K. Burke, M. Ernzerhof, Generalized gradient approximation made simple, *Phys. Rev. Lett.* 77 (1996) 3865–3868, <https://doi.org/10.1103/PhysRevLett.77.3865>.
- [20] T. Ozaki, Variationally optimized atomic orbitals for large-scale electronic structures, *Phys. Rev. B* 67 (2003), 155108. <https://doi.org/10.1103/PhysRevB.67.155108>.
- [21] G. Kresse, J. Furthmüller, Efficient iterative schemes for *ab initio* total-energy calculations using a plane-wave basis set, *Phys. Rev. B* 54 (1996) 11169–11186, <https://doi.org/10.1103/PhysRevB.54.11169>.
- [22] G. Kresse, D. Joubert, From ultrasoft pseudopotentials to the projector augmented-wave method, *Phys. Rev. B* 59 (1999) 1758–1775, <https://doi.org/10.1103/PhysRevB.59.1758>.
- [23] H.J. Monkhorst, J.D. Pack, Special points for Brillouin-zone integrations, *Phys. Rev. B* 13 (1976) 5188–5192, <https://doi.org/10.1103/PhysRevB.13.5188>.
- [24] P.E. Blöchl, Projector augmented-wave method, *Phys. Rev. B* 50 (1994) 17953–17979, <https://doi.org/10.1103/PhysRevB.50.17953>.
- [25] R. Dronskowski, P.E. Blöchl, Crystal orbital Hamilton populations (COHP): energy-resolved visualization of chemical bonding in solids based on density-functional calculations, *J. Phys. Chem.* 97 (1993) 8617–8624, <https://doi.org/10.1021/j100135a014>.
- [26] V.L. Deringer, A.L. Tchougréeff, R. Dronskowski, Crystal orbital Hamilton population (COHP) analysis as projected from plane-wave basis sets, *J. Phys. Chem. A* 115 (2011) 5461–5466, <https://doi.org/10.1021/jp202489s>.
- [27] S. Maintz, V.L. Deringer, A.L. Tchougréeff, R. Dronskowski, Analytic projection from plane-wave and PAW wavefunctions and application to chemical-bonding analysis in solids, *J. Comput. Chem.* 34 (2013) 2557–2567, <https://doi.org/10.1002/jcc.23424>.
- [28] S. Maintz, V.L. Deringer, A.L. Tchougréeff, R. Dronskowski, LOBSTER: a tool to extract chemical bonding from plane-wave based DFT, *J. Comput. Chem.* 37 (2016) 1030–1035, <https://doi.org/10.1002/jcc.24300>.
- [29] C. Hostert, D. Music, J. Bednarcik, J. Keckes, V. Kapaklis, B. Hjörvarsson, et al., *Ab initio* molecular dynamics model for density, elastic properties and short range order of Co-Fe-Ta-B metallic glass thin films, *J. Phys. Condens. Matter* 23 (2011), 475401. <https://doi.org/10.1088/0953-8984/23/47/475401>.
- [30] F. Birch, Finite strain isotherm and velocities for single-crystal and polycrystalline NaCl at high pressures and 300°K, *J. Geophys. Res.* 83 (1978) 1257, <https://doi.org/10.1029/JB083iB03p01257>.
- [31] V. Schnabel, M. Köhler, S. Evertz, J. Gamcova, J. Bednarcik, D. Music, et al., Revealing the relationships between chemistry, topology and stiffness of ultrastrong Co-based metallic glass thin films: a combinatorial approach, *Acta Mater.* 107 (2016) 213–219, <https://doi.org/10.1016/j.actamat.2016.01.060>.
- [32] A.-C. Dippel, H.-P. Liemann, J.T. Delitz, P. Walter, H. Schulte-Schrepping, O.H. Seeck, et al., Beamline P02.1 at PETRA III for high-resolution and high-energy powder diffraction, *J. Synchrotron Radiat.* 22 (2015) 675–687, <https://doi.org/10.1107/S1600577515002222>.
- [33] A.P. Hammersley, *FT2D: An Introduction and Overview*, ESRF, Grenoble, 1997.
- [34] A.P. Hammersley, S.O. Svensson, A. Thompson, Calibration and correction of spatial distortions in 2D detector systems, *Nucl. Instrum. Meth. A* 346 (1994) 312–321, [https://doi.org/10.1016/0168-9002\(94\)90720-X](https://doi.org/10.1016/0168-9002(94)90720-X).
- [35] A.P. Hammersley, S.O. Svensson, M. Hanfland, A.N. Fitch, D. Hausermann, Two-dimensional detector software: from real detector to idealised image or two-theta scan, *High Pressure Res.* 14 (1996) 235–248, <https://doi.org/10.1080/08957959608201408>.
- [36] P. Juhás, T. Davis, C.L. Farrow, S.J.L. Billinge, PDFgetX3: a rapid and highly automatable program for processing powder diffraction data into total scattering pair distribution functions, *J. Appl. Crystallogr.* 46 (2013) 560–566, <https://doi.org/10.1107/S0021889813005190>.
- [37] K. Matoy, H. Schönherr, T. Detzel, T. Schöberl, R. Pippan, C. Motz, et al., A comparative micro-cantilever study of the mechanical behavior of silicon based passivation films, *Thin Solid Films* 518 (2009) 247–256, <https://doi.org/10.1016/j.tsf.2009.07.143>.
- [38] D. Di Maio, S.G. Roberts, Measuring fracture toughness of coatings using focused-ion-beam-machined microbeams, *J. Mater. Res.* 20 (2005) 299–302, <https://doi.org/10.1557/JMR.2005.0048>.
- [39] R. Pippan, S. Wurster, D. Kiener, Fracture mechanics of micro samples: fundamental considerations, *Mater. Des.* 159 (2018) 252–267, <https://doi.org/10.1016/j.matdes.2018.09.004>.
- [40] B.N. Jaya, C. Kirchlechner, G. Dehm, Can microscale fracture tests provide reliable fracture toughness values?: a case study in silicon, *J. Mater. Res.* 30 (2015) 686–698, <https://doi.org/10.1557/jmr.2015.2>.
- [41] S. Brinckmann, C. Kirchlechner, G. Dehm, Stress intensity factor dependence on anisotropy and geometry during micro-fracture experiments, *Scr. Mater.* 127 (2017) 76–78, <https://doi.org/10.1016/j.scriptamat.2016.08.027>.
- [42] S. Brinckmann, K. Matoy, C. Kirchlechner, G. Dehm, On the influence of microcantilever pre-crack geometries on the apparent fracture toughness of brittle materials, *Acta Mater.* 136 (2017) 281–287, <https://doi.org/10.1016/j.actamat.2017.07.014>.
- [43] G. Dehm, B.N. Jaya, R. Raghavan, C. Kirchlechner, Overview on micro- and nanomechanical testing: new insights in interface plasticity and fracture at small length scales, *Acta Mater.* 142 (2018) 248–282, <https://doi.org/10.1016/j.actamat.2017.06.019>.
- [44] S. Wurster, C. Motz, R. Pippan, Characterization of the fracture toughness of micro-sized tungsten single crystal notched specimens, *Philos. Mag.* 92 (2012) 1803–1825, <https://doi.org/10.1080/14786435.2012.658449>.
- [45] K. Thompson, D. Lawrence, D.J. Larson, J.D. Olson, T.F. Kelly, B. Gorman, In situ site-specific specimen preparation for atom probe tomography, *Ultramicroscopy* 107 (2007) 131–139, <https://doi.org/10.1016/j.ultramicro.2006.06.008>.
- [46] A. Savitzky, M.J.E. Golay, Smoothing and differentiation of data by simplified least squares procedures, *Anal. Chem.* 36 (1964) 1627–1639, <https://doi.org/10.1021/ac60214a047>.
- [47] H. Rempp, On the electronic density of states of the transition metals, *Z. Physik* 267 (1974) 181–186, <https://doi.org/10.1007/BF01669218>.
- [48] V.L. Deringer, W. Zhang, M. Lumeij, S. Maintz, M. Wuttig, R. Mazzarello, et al., Bonding nature of local structural motifs in amorphous GeTe, *Angew. Chem. Int. Ed. Eng.* 53 (2014) 10817–10820, <https://doi.org/10.1002/anie.201404223>.
- [49] P. Kontis, M. Köhler, S. Evertz, Y.-T. Chen, V. Schnabel, R. Soler, et al., Nano-laminated thin film metallic glass design for outstanding mechanical properties, *Scr. Mater.* 155 (2018) 73–77, <https://doi.org/10.1016/j.scriptamat.2018.06.015>.
- [50] M.D. Demetriou, M.E. Launey, G. Garrett, J.P. Schramm, D.C. Hofmann, W.L. Johnson, et al., A damage-tolerant glass, *Nat. Mater.* 10 (2011) 123–128, <https://doi.org/10.1038/nmat2930>.

- [51] M.D. Demetriou, G. Kaltenboeck, J.-Y. Suh, G. Garrett, M. Floyd, C. Crewdson, et al., Glassy steel optimized for glass-forming ability and toughness, *Appl. Phys. Lett.* 95 (2009), 41907, <https://doi.org/10.1063/1.3184792>.
- [52] A. Kawashima, H. Kurishita, H. Kimura, T. Zhang, A. Inoue, Fracture toughness of Zr₅₅Al₁₀Ni₅Cu₃₀ bulk metallic glass by 3-point bend testing, *Mater. Trans. JIM* 46 (2005) 1725–1732.
- [53] X.J. Gu, S.J. Poon, G.J. Shiflet, J.J. Lewandowski, Compressive plasticity and toughness of a Ti-based bulk metallic glass, *Acta Mater.* 58 (2010) 1708–1720, <https://doi.org/10.1016/j.actamat.2009.11.013>.
- [54] C.J. Gilbert, R.O. Ritchie, W.L. Johnson, Fracture toughness and fatigue-crack propagation in a Zr–Ti–Ni–Cu–Be bulk metallic glass, *Appl. Phys. Lett.* 71 (1997) 476–478, <https://doi.org/10.1063/1.119610>.
- [55] D.W. Smith, The antibonding effect, *J. Chem. Educ.* 77 (2000) 780, <https://doi.org/10.1021/ed077p780>.
- [56] A.S. Argon, Plastic deformation in metallic glasses, *Acta Metall.* 27 (1979) 47–58, [https://doi.org/10.1016/0001-6160\(79\)90055-5](https://doi.org/10.1016/0001-6160(79)90055-5).
- [57] S. Evertz, D. Music, V. Schnabel, J. Bednarcik, J.M. Schneider, Thermal expansion of Pd-based metallic glasses by ab initio methods and high energy X-ray diffraction, *Sci. Rep.* 7 (2017), 15744, <https://doi.org/10.1038/s41598-017-16117-7>.
- [58] D. Geissler, J. Freudenberger, H. Wendrock, M. Zimmermann, A. Gebert, On sample size effects in fracture toughness determination of bulk metallic glasses, *Eng. Fract. Mech.* 202 (2018) 500–507, <https://doi.org/10.1016/j.engfracmech.2018.09.020>.

Paper III

**Boron concentration induced Co-Ta-B composite formation observed in the transition
from metallic to covalent glasses**

S. Evertz, S. Prünke, L. Patterer, A. Marshal, D. M. Holzapfel, A. Schökel, M. Hans,

D. Primetzhofer and J. M. Schneider

Condensed Matter **5(1)**, 18 (2020), doi: 10.3390/condmat5010018

Article

Boron Concentration Induced Co-Ta-B Composite Formation Observed in the Transition from Metallic to Covalent Glasses

Simon Evertz ^{1,*}, Stephan Prünte ¹, Lena Patterer ¹, Amalraj Marshal ¹, Damian M. Holzapfel ¹, Alexander Schökel ², Marcus Hans ¹, Daniel Primetzhofer ³ and Jochen M. Schneider ¹

¹ Materials Chemistry, RWTH Aachen University, Kopernikusstr. 10, 52074 Aachen, Germany; prunte@mch.rwth-aachen.de (S.P.); patterer@mch.rwth-aachen.de (L.P.); amalraj@mch.rwth-aachen.de (A.M.); holzapfel@mch.rwth-aachen.de (D.M.H.); hans@mch.rwth-aachen.de (M.H.); schneider@mch.rwth-aachen.de (J.M.S.)

² Deutsches Elektronen-Synchrotron DESY, FS-PE, Notkestr. 85, 22602 Hamburg, Germany; alexander.schoekel@desy.de

³ Department of Physics and Astronomy, Uppsala University, S-75120 Uppsala, Sweden; daniel.primetzhofer@physics.uu.se

* Correspondence: evertz@mch.rwth-aachen.de

Received: 12 February 2020; Accepted: 16 March 2020; Published: 18 March 2020



Abstract: Due to their unique property combination of high strength and toughness, metallic glasses are promising materials for structural applications. As the behaviour of metallic glasses depends on the electronic structure which in turn is defined by chemical composition, we systematically investigate the influence of B concentration on glass transition, topology, magnetism, and bonding for B concentrations $x = 2$ to 92 at.% in the $(\text{Co}_{6.8 \pm 3.9}\text{Ta})_{100-x}\text{B}_x$ system. From an electronic structure and coordination point of view, the B concentration range is divided into three regions: Below 39 ± 5 at.% B, the material is a metallic glass due to the dominance of metallic bonds. Above 69 ± 6 at.%, the presence of an icosahedra-like B network is observed. As the B concentration is increased above 39 ± 5 at.%, the B network evolves while the metallic coordination of the material decreases until the B concentration of 67 ± 5 at.% is reached. Hence, a composite is formed. It is evident that, based on the B concentration, the ratio of metallic bonding to icosahedral bonding in the composite can be controlled. It is proposed that, by tuning the coordination in the composite region, glassy materials with defined plasticity and processability can be designed.

Keywords: metallic glass; composite; metalloid network; bonding

1. Introduction

Metallic glasses are promising materials for structural applications due to their unique property combination of high yield strength and fracture toughness [1–5]. While they are capable of plastic deformation at the microscale [5], the glass forming ability (GFA) poses often formidable challenges for both, processing and application [6]. Alloying with metalloids such as B can enhance the GFA in metallic glasses [3,7,8]. Co-B based metallic glasses with boron concentrations in the range of 35 at.% have been reported to exhibit yield strengths larger than 5000 MPa [9,10]. With increasing B concentrations up to 50 at.%, the fracture strength reaches values up to 11,000 MPa [11]. Simultaneously, between 28 and 50 at.% B the reduced Young's modulus increases from 280 to 345 GPa, hardness from 10 to 13 GPa, and fracture toughness from 2.5 to 6 $\text{MPa}\cdot\text{m}^{0.5}$ [11]. Based on ab initio calculations, a stiffness of 263 GPa is predicted for $\text{Co}_{33.0}\text{Ta}_{3.5}\text{B}_{63.5}$ [12]. On the other hand, amorphous borides with B concentrations >90 at.% form icosahedra-like B networks [13] and are reported to be ultra-hard [14,15], exhibit low friction due to self-lubrication [15], and show catalytic properties [16]. However, those

covalent borides exhibit brittle behaviour [13] in contrast to metallic glasses. For Co-Ta-B, the range of B concentration for which the transition from metallic glass to covalent glasses occurs has not been studied. Furthermore, the impact of B additions on the electronic structure and properties of Co-Ta-B has not been investigated systematically. Hence, to identify and to rationalise the composition induced changes in the electronic structure of metallic and covalent Co-Ta-B glasses as well as within their transition regime, we vary the B concentration of $(\text{Co}_{6.8\pm 3.9}\text{Ta})_{100-x}\text{B}_x$ supercells between $x = 2$ and 92 at.% in ab initio calculations and between $x = 22$ and 85 at.% in experimental samples. Specifically, we probe the B concentration induced changes in glass transition, topology, magnetisation, and bonding by ab initio calculations as well as high energy X-ray scattering, magnetometry, and X-ray photoelectron spectroscopy. Thereby, we reveal that the transition from a metallic to a covalent glass is associated with the formation of a composite.

2. Methods

2.1. Theoretical Methods

Density-functional-theory (DFT) [17] based ab initio molecular dynamic calculations were conducted on a supercell containing 115 atoms of composition $(\text{Co}_{6.8\pm 3.9}\text{Ta})_{100-x}\text{B}_x$ ($x = 2$ to 92 at.%). Following the modelling routine for metallic glasses developed by Hostert et al. [18], the supercell was heated up to 4000 K for 400 fs in an NVT ensemble and subsequently quenched to 0 K by geometry relaxation using the openMX code (version 3.8) [19,20]. Electronic potentials with the general gradient approximation were employed [21]. The following basis functions were applied: Co5.5-s2p1d1, Ta7.0-s2p1d1f1 and B4.5-s2p2. The first symbol designates the chemical element followed the cutoff-radius. The primitive orbitals are defined by the last set of symbols. A k-grid of $1\times 1\times 1$ and a cutoff-radius of 150 Ry were used. The temperature was controlled by scaling of velocities. After quenching to 0 K, the volume was relaxed employing the Vienna Ab initio Simulation Package (VASP) [22,23] with projector augmented-wave potentials [23,24] using the Perdew-Burke-Ernzerhof functional [21] and integration over the Brillouin zone on a $3\times 3\times 3$ Monkhorst-Pack k-grid [25]. The iteration cycle of heating-quenching-volume relaxation was repeated until the volume change was smaller than 2%. To calculate the pair distribution function $G(r)$ from the atomic positions, the relaxed structure was hold at 300 K for 200 fs. $G(r)$ was averaged over time. The crystal orbital overlap populations (COOP) [26] and crystal orbital Hamilton populations (COHP) [27] were calculated using the LOBSTER code (version 3.2.0) [28–30].

2.2. Experimental Methods

Magnetron sputtering was utilized to synthesize $(\text{Co}_{6.8\pm 3.9}\text{Ta})_{100-x}\text{B}_x$ ($x = 22$ to 85 at.%) thin films on Si, NaCl, and polyimide substrates for the characterization of chemistry, magnetic, and binding properties; glass transition; and topology, respectively. Therefore, an ultra-high vacuum combinatorial growth system [31] with a base pressure lower than 2×10^{-8} Pa and a target-to-substrate distance of 10 cm was employed. Floating substrate potential and non-intentional heating were used. For depositions on Si and polyimide substrates, the substrate was not rotated to obtain combinatorial samples. For depositions on NaCl, substrate rotation was used to obtain homogeneous films. The NaCl substrate was subsequently dissolved in deionized water. The resulting thin film flakes were cleaned in isopropanol and acetone for usage in in situ heating high energy X-ray scattering experiments. Up to three 2-inch B targets with a purity of 99.9% and one 2-inch $\text{Co}_{88}\text{Ta}_{12}$ target with 99.9% purity were used. The working gas during deposition was Ar (purity 6.0) with a pressure of 0.4 Pa. The B targets were sputtered in RF mode with up to 10.2 Wcm^{-2} , while the CoTa target was sputtered in DC mode with up to 1.5 Wcm^{-2} .

The chemical composition was determined using standard-based energy dispersive X-ray spectroscopy with a Bruker Quantax75 EDS system in a Hitachi TM4000plus scanning electron microscope. The EDX measurements were calibrated with a $\text{Co}_{71}\text{Ta}_6\text{B}_{23}$ thin film which was characterized by ion

beam analysis using time-of-flight elastic recoil detection analysis (ToF-ERDA) at the tandem accelerator laboratory of Uppsala University. Recoils were generated by $^{127}\text{I}^{8+}$ primary ions with a kinetic energy of 36 MeV. The detector telescope, consisting of thin carbon foils for the ToF [32] as well as a gas ionization detection system [33], was situated at an angle of 45° with respect to the primary ions and both the incidence as well as exit angles were 22.5° with respect to the specimen surface. Time and energy coincidence spectra were converted into a depth profile using the CONTES software package [34]. The O concentration of the $\text{Co}_{71}\text{Ta}_6\text{B}_{23}$ thin film was <1 at.%. Meanwhile, the statistical uncertainty of the concentration was with 2% relative deviation maximum for B and maximum systematic uncertainties of 10% relative deviation are assumed due to uncertainties of the specific energy loss of primary ions and recoiled species.

High energy X-ray scattering was carried out at beamline P02.1 [35] of the PETRA III electron storage ring at Deutsches Elektronen-Synchrotron (DESY), Hamburg, Germany, utilizing X-rays with a wavelength of 0.20701 \AA . To measure the topology along the CoTa-B compositional gradients, samples deposited on polyimide were measured [31]. To determine the structural changes and the glass transition temperature T_g , powder samples sealed in fused silica capillaries under Ar atmosphere were heated in situ by a Si_3N_4 heating element (Bach RC GmbH) to temperatures up to 1400 K with a heating rate of 15 K/min. Data were collected with a Perkin Elmer XRD 1621 plate detector and integrated by the FIT2D software [36–38]. The background-corrected data were used to calculate the structure factor as well as the pair distribution function $G(r)$ by a fast Fourier transformation implemented in the PDFgetX3 software package [39].

Binding energies were measured by X-ray photoelectron spectroscopy (XPS) in a Kratos Analytical Axis Supra. Al $K\alpha$ radiation (photon energy 1.4866 keV) was employed. The sample was deposited immediately prior to the XPS measurement. However, due to the contact to ambient atmosphere during sample transfer (~ 15 min), the surface has already been oxidized. To remove the oxide, the sample was etched using an Ar^+ ions with an energy of 500 eV for 120 s. The binding energy was corrected for charging by using the C 1s peak at 285 eV for calibration. CasaXPS software was utilised to analyse the acquired spectra employing Shirley backgrounds. The B 1s peak was fitted with a mixed Gauss-Lorentz peak (30/70) and the Co 2p signal was fitted according to Biesinger et al. [40]. The saturation magnetization was measured at room temperature using the Vibrating Sample Magnetometer (VSM) option at a physical property measurement system (PPMS) from Quantum Design employing a maximum magnetic field of 2 T.

3. Results and Discussion

3.1. Glass Transition

As a first indicator for differences between high and low boron concentration regimes, the glass transition temperature T_g as an integral measure for the structure of a glass is considered. Table 1 lists the glass transition temperatures obtained by measuring average atomic volume changes by high energy X-ray scattering (Supplementary Figure S1) for $(\text{Co}_{6.8\pm 3.9}\text{Ta})_{100-x}\text{B}_x$ with B concentrations between 22 and 85 at.%. The Co/Ta-ratio is constant at 6.8 ± 3.9 . T_g increases from 757 ± 1 K to 900 ± 1 K up to a B concentration of 46 at.%, then decreases to around 595 ± 1 K at 59 at.% B, and stays constant around 590 ± 14 K for higher B concentrations. These glass transition temperatures are lower than those reported in literature ($T_g = 975$ K for $\text{Co}_{55}\text{Ta}_{10}\text{B}_{35}$) [9], which may be attributed to the different synthesis routes.

As T_g is inversely proportional to the configurational entropy S_c [41], S_c is larger for high B concentrations above 59 at.% compared to lower B concentrations. The constant T_g and hence a constant S_c corresponds to a constant number of degrees of freedom for $(\text{Co}_{6.8\pm 3.9}\text{Ta})_{100-x}\text{B}_x$ with more than 59 at.% B, despite the further incorporation of B into the material. This constant number of degrees of freedom suggests the existence of a B network in the high B concentration regime.

Table 1. Glass transition temperature T_g for $(\text{Co}_{6.8\pm 3.9}\text{Ta})_{100-x}\text{B}_x$ as a function of B concentrations determined by high-energy X-ray scattering

Composition (at.%)	T_g in K
$\text{Co}_{67}\text{Ta}_{11}\text{B}_{22}$	757 ± 1
$\text{Co}_{56}\text{Ta}_{10}\text{B}_{34}$	829 ± 1
$\text{Co}_{53}\text{Ta}_9\text{B}_{38}$	899 ± 2
$\text{Co}_{46}\text{Ta}_8\text{B}_{46}$	900 ± 5
$\text{Co}_{40}\text{Ta}_8\text{B}_{52}$	773 ± 1
$\text{Co}_{37}\text{Ta}_4\text{B}_{59}$	595 ± 1
$\text{Co}_{35}\text{Ta}_4\text{B}_{61}$	600 ± 1
$\text{Co}_{33}\text{Ta}_5\text{B}_{62}$	607 ± 1
$\text{Co}_{32}\text{Ta}_3\text{B}_{65}$	-
$\text{Co}_{18}\text{Ta}_4\text{B}_{78}$	573 ± 1
$\text{Co}_{12}\text{Ta}_3\text{B}_{85}$	575 ± 1

3.2. Topology

To further investigate the structural differences with focus on the short-range order, the reduced pair distribution functions $G(r)$ of $(\text{Co}_{6.8\pm 3.9}\text{Ta})_{100-x}\text{B}_x$ as a function of B concentration are shown in Figure 1a. For low B concentrations, the metal-metal (M-M) bonds with a distance of 2.6 Å at 22 at.% dominate $G(r)$. At 3.1 Å, bonds with the second nearest neighbour are visible. The metal-boron (M-B) bonds result in a small peak at 2.1 Å for 22 at.% B, while the B-B bonds are not visible due to the low scattering power of B in X-ray scattering [42].

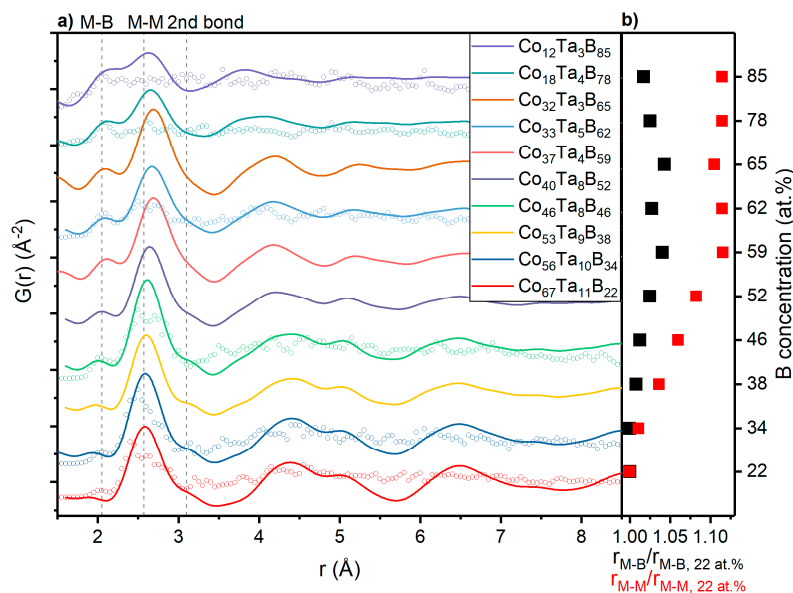


Figure 1. Short range order of $(\text{Co}_{6.8\pm 3.9}\text{Ta})_{100-x}\text{B}_x$. (a) Reduced pair distribution functions $G(r)$ for $(\text{Co}_{6.8\pm 3.9}\text{Ta})_{100-x}\text{B}_x$ shown as a function of B concentration obtained by high-energy X-ray scattering. Open circles depict the ab initio $G(r)$ (b) Shift of the first and second peak distances $r_{\text{M-B}}$, $r_{\text{M-M}}$ of $G(r)$ corresponding to the metal-boron (M-B) and metal-metal (M-M) bonds, respectively. The shift is relative to the peak position for the sample with a B concentration of 22 at.%.

With increasing B concentration, the intensity of the M-B bonds increases, while the intensity of the M-M peak decreases as it is expected for larger B concentrations and the corresponding lower metal concentrations in the sample. Hence, as the B concentration is increased, the metal atoms bond more often with B than with each other. Moreover, the bond lengths $r_{\text{M-B}}$ and $r_{\text{M-M}}$ increase with an increasing B concentration (Figure 1b). Between 34 and 59 at.% B, the bond lengths increase by 4% for M-B and by 10% for M-M bonds. Above 59 at.%, $r_{\text{M-M}}$ remains constant, while $r_{\text{M-B}}$ decreases by 2.3%. This is consistent with the evolution of a B network, surrounding the metal atoms and separating them

at a constant distance once the B network completely evolved at 59 at.% B. Simultaneously, the M-B bond length decreases upon further incorporation of B into the network, as the additional B atoms populate the B network and thereby surround the metal atoms more closely.

This B network evolution notion is supported by the calculated total and partial coordination numbers (CN). The total CN (Figure 2a) remains constant around 12 up to 40 at.% B, then decreases between 40 and 70 at.% B down to 10 and stays constant at 7 for B concentrations larger 77 at.%. The low total CN above 77 at.% B is consistent with the formation of a B network structure. Further evidence for the B network evolution is given by the B concentration induced changes in partial CNs. Focusing on the metal coordination in Figure 2b,c, a continuous decrease of metal-metal coordination is observed upon B addition. The decrease of Ta-Co coordination occurs predominantly between 40 and 70 at.% B. Above 70 at.% B, the metal-metal CN is 0, since the metal-metal bonds are no longer formed and all remaining metal atoms form metal-B bonds. The opposite is observed for the metal-B coordination that increases from 0 to 9 for Co-B and from 0 to 10 for Ta-B in the composition range of 2 to 70 at.% B, being constant at 9 (Co-B) for larger B concentrations. The Ta-B CN above 70 at.% B scatters strongly, as only 3, 2 and 1 Ta atoms are present in the simulation cells for 77, 83, and 92 at.% B, respectively. Hence, these CN may not be significant due to lack of statistics. Finally, the B concentration induced changes in the B-B CN (Figure 2d) give the strongest evidence for the formation of a B network. While the CN for B-B ranges from 0 to 1 for B concentrations lower 40 at.%, a jump of the B-B CN to 3.5 is observed at 40 at.%, which is consistent with the initiation of the B network formation proposed earlier based on the $G(r)$ data shown in Figure 1a. With further increasing B concentration, the CN increases up to 6 for 92 at.% B. The CN of 6 is close the CN of 5.6 for a perfect icosahedron in a crystalline structure [43]. As an icosahedra-like structure with imperfect icosahedra has been predicted and experimentally verified for the amorphous $Al_{0.75}Y_{0.75}B_{14}$ [13], amorphous B_4C [44], as well as for amorphous B [45,46], the partial coordination numbers obtained here give evidence for the formation of an icosahedra-like B network starting to form at 40 at.% B.

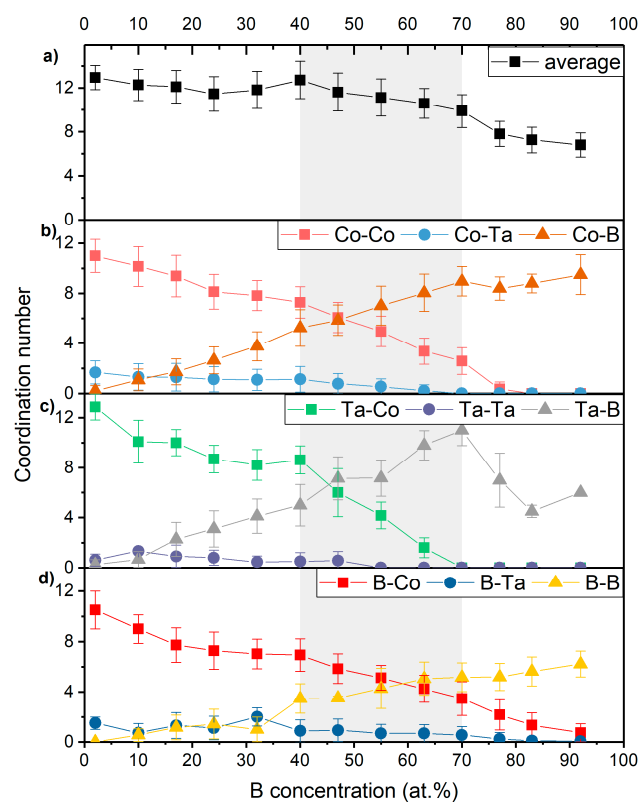


Figure 2. Ab initio coordination number (CN) as a function of B concentration. (a) Average CN taking all bonds into account. (b–d) Partial CN. Lines between the data points serve as a guide to the eye.

Based on the short-range order and topology analysis carried out above, $(\text{Co}_{6.8\pm 3.9}\text{Ta})_{100-x}\text{B}_x$ is identified as metallic glass for B concentrations lower 40 at.% as the metals are predominantly coordinated with metals, while for B concentrations larger 70 at.% a network glass is present due to the presence of an icosahedral-like B network with metal atoms surrounded by B only. Within the concentration range of B concentrations between 40 and 70 at.%, the existence of a glass composite containing metallic glass and covalent glass-like regions is proposed, as the B network evolves in this region and the metal atoms are still coordinated with metals.

To compare physical and in-silico samples, $G(r)$ of the ab initio models are depicted in Figure 1a with open symbols. As the ab initio model can only cover the first coordination shell, bond distances smaller than 3.5 Å should be considered in the ab initio $G(r)$. In the first coordination shell, however, the calculated $G(r)$ exhibits peaks at the M-B, M-M and 2nd bond peak position of the experimentally obtained $G(r)$. It is evident that the M-M peak splits into two peaks, indicating the presence of Co-Co and Co-Ta bonds. For large B concentrations, only the M-B are visible due to the low number of metal atoms in the cell. Considering the small cell size and the associated statistical limitations of the ab initio $G(r)$, the ab initio configurations are consistent with the experiment. However, in contrast to the experimental $G(r)$, also the B-B bonds at 1.71 Å for large B concentrations can be analysed. The B-B bond distances are consistent with icosahedral bonding, as reported in [13,44,46].

To examine the medium-range order (MRO), the structure factor $S(q)$ of $(\text{Co}_{6.8\pm 3.9}\text{Ta})_{100-x}\text{B}_x$ as a function of B concentration is shown in Figure 3a. The $S(q)$ shows clearly that samples are amorphous over the whole compositional range since Bragg peaks are absent. With increasing B concentration up to 62 at.% (Figure 3b), the amorphous principal peak of the structure factor at 3.1 \AA^{-1} shows a significant increase in full width at half maximum (FWHM), indicating the formation of less medium range ordered material. This observation is consistent with the higher configurational entropy notion at these B concentrations discussed in the context of the B concentration induced changes in glass transition temperature above. The vanishing double peak at 5.2 and 6.0 \AA^{-1} between 22 and 59 at.% B underlines this enhanced disorder. In addition, a shoulder to the principal peak arises at 2.3 \AA^{-1} and is clearly visible for B concentrations between 59 and 78 at.%, where the width of the principle peak increases strongly. The onset of the shoulder can already be seen in the asymmetry of the peak at 46 at.% B. This shoulder indicates that two types of medium-range order are present, being consistent with the glass composite regime proposed above.

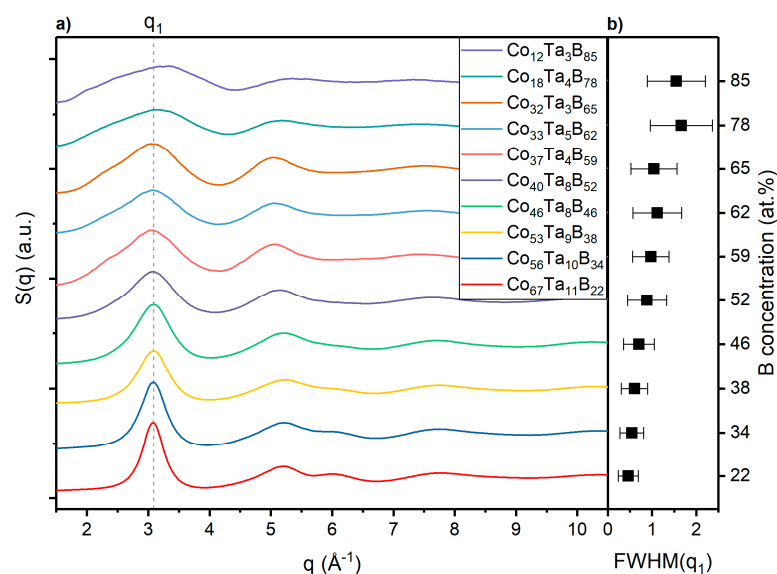


Figure 3. Medium range order of $(\text{Co}_{6.8\pm 3.9}\text{Ta})_{100-x}\text{B}_x$. (a) Structure factor $S(q)$ for $(\text{Co}_{6.8\pm 3.9}\text{Ta})_{100-x}\text{B}_x$ shown as a function of B concentration obtained by high-energy X-ray scattering. (b) Full width at half maximum (FWHM) of the principal peak q_1 of $S(q)$.

3.3. Electronic Structure

In the next step, we critically appraise the glass composite formation notion by analysis of the electronic structure. According to the free electron model of Nagel and Tauc [47], twice the Fermi vector k_f , which describes the Fermi sphere in amorphous materials, corresponds to the principal peak position of the structure factor q_p in a stable metallic glass:

$$2k_f = q_p \quad (1)$$

Hence, the Fermi level E_f can be experimentally determined from $S(q)$ by inserting Equation (1) into Equation (2) [48]

$$E_f = \frac{\hbar^2}{2m} k_f^2 \quad (2)$$

where \hbar is the Planck constant divided by 2π and m the electron mass. As a comparison of experimentally and theoretically obtained absolute values of E_f is not possible, the relative shift of E_f as a function of B concentration is compared in Figure 4. Based on ab initio data, E_f is constant up to 63 at.% B and decreases for higher B concentrations. The experimentally obtained E_f based on the free-electron model for metallic glasses [47] remains constant for less than 62 at.% B and shifts to larger values for higher B concentrations. This deviation between the free electron model and the ab initio model indicates that the free-electron model is not applicable for B concentrations larger 62 at.%. Hence, the metallic character of the material is lost. This loss of metallic bonding character for B concentrations larger than 62 at.% is consistent with the proposal of a covalent network glass for large B concentrations made above.

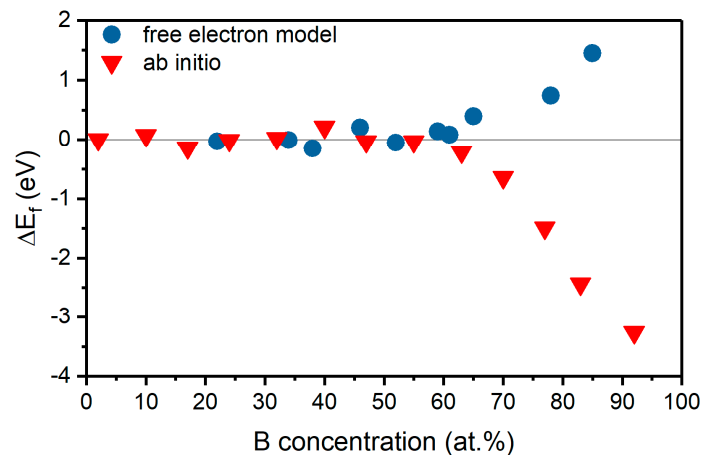


Figure 4. Shift of Fermi level E_f as a function of B concentration. Red triangles are based on the Fermi level calculated by ab initio calculations, the blue circles represent experimental data points based on the free-electron model [47].

The orbital overlap and bond strength give further insight into the change from metallic to covalent character by means of the integrated crystal orbital overlap population (ICOOP) [26] and integrated crystal orbital Hamilton population (ICOHP) [27] at E_f . The latter is a measure of bond strength [28]. Figure 5a plots the partial ICOHP at E_f for Co-B, B-B, Co-Co and Ta-B bonds. While the Co-Co contribution to the bond strength is low and constant up to 77 at.% (for higher B concentrations, Co-Co interaction cannot be found), the metal-B bond strength is between 1.5 and 2 eV, decreasing up to 32 at.% B and staying roughly constant for more than 32 at.% B. Significant changes are observed for the

B-B bond strengths: Up to 32 at.%, the bonding contribution decreases down to -2.9 eV. Subsequently, the bond strength increases further up to -4.8 eV at 77 at.% and is constant for larger B concentrations (negative values are bonding, positive values anti-bonding contributions). The orbital overlap as quantified by ICOOP at E_f (Figure 5b) is consistent with the ICOHP.

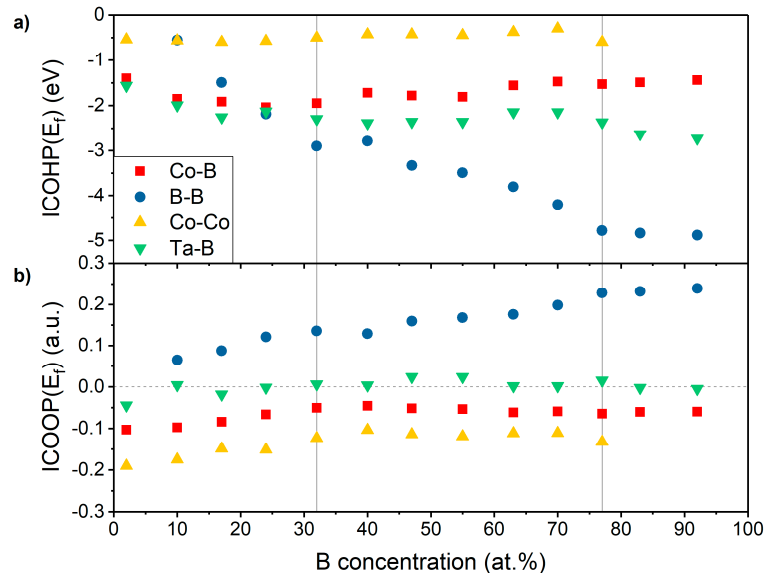


Figure 5. Ab initio bonding analysis of $(\text{Co}_{6.8\pm 3.9}\text{Ta})_{100-x}\text{B}_x$. (a) Integrated crystal orbital Hamilton population at the Fermi level ($\text{ICOHP}(E_f)$) and (b) integrated crystal orbital overlap population at the Fermi level ($\text{ICOOP}(E_f)$) as a function of B concentration.

Summarizing the ab initio bonding analysis, the change of bonding from metal-metal to metal-B and B-B interactions is driven by increasing B-B bond strength and orbital overlap. Both the measure of bond strength $\text{ICOHP}(E_f)$ and the integrated orbital overlap at E_f of B-B as a function of B concentration change slope two times at 32 at.% B and at 77 at.% B, being consistent with the metallic glass, composite, and B network glass regions defined above. The constant bond strength and overlap for B concentrations larger 77 at.% are consistent with the notion of a completely evolved B network in this composition range.

Investigating the B concentration induced changes in binding energy experimentally (Figure 6), the results obtained by XPS are more complex to interpret. For samples with 16, 47 and 65 at.% B, the B 1s binding energy (Figure 6a) exhibits a small but significant peak shift of 0.3 eV to larger binding energies consistent with the ab initio bonding analysis. The peak deconvolution indicates oxidation of the sample with 16 at.% B due to the presence of 16 at.% O in the sample. The B 1s peak, however, can neither be attributed to icosahedral nor to octahedral bonding or bonding in a solid solution, as the binding energies for the B 1s peak in the icosahedral AlMgB_{14} structure with 188.2 eV [49], in Co-B bonds with 188.3 eV [50], in Ta-B bonds with 188.7 eV [51] and alpha-B with 188.0 eV [13] are experimentally not resolvable. The B1s binding energy of icosahedrally bonded B in AlMgB_{14} is shown here as an example for B-rich solids.

The Co $2p_{3/2}$ peak (Figure 6b) for samples with 16, 47 and 65 at.% B at a binding energy of 778.3 eV shows the presence of Co-B bonds as this binding energy is in between those for Co-B bonds in CoB (778.2 eV) and Co_2B (778.6 eV) [50]. The observation of Co-B bonds is consistent with the ab initio bonding analysis. As for the B 1s peak, a small but significant peak shift of 0.2 eV towards higher binding energies between 16 and 65 at.% B is observed. A similar shift is obtained for the Ta 4f feature in the binding energy spectrum (not shown). The larger binding energy for the metals indicates an increased B coordination, consistent with the analysis of the coordination number.

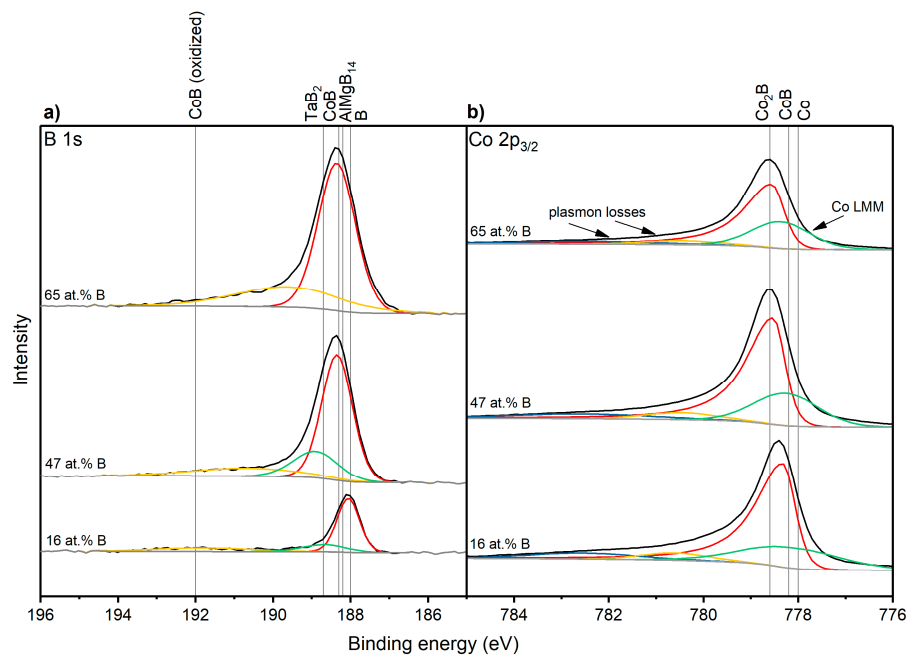


Figure 6. XPS-spectra of $(\text{Co}_{6.8\pm 3.9}\text{Ta})_{100-x}\text{B}_x$. (a) B 1s peak and (b) Co $2p_{3/2}$ peak. The intensity scale is linear. In black the measured data are shown, in colour the peak deconvolution.

3.4. Magnetization

It is well known that the soft-magnetism of Co-Ta-B is promising to reduce transformer losses [7,10]. Hence, the influence of the enhanced B concentration on the volume magnetization is shown in Figure 7. The total volume magnetization as well as the partial contributions of Co, Ta, and B based on ab initio data are compared with experimental data points of the saturation volume magnetization. The main contribution to volume magnetization comes from Co atoms, while B does not show a magnetic moment. With increasing B concentration, a decrease of magnetization is clearly visible due to the dilution of metal coupling by B. This decrease of magnetization is in agreement with literature [52]. Above 63 at.% B the volume magnetization is approximately 0 due to the lack of metal-metal interactions, explainable by a B network surrounding the metals for high B concentrations. During the decrease from 0.1 to $0 \mu_B/\text{\AA}^3$, a change in slope at 40 at.% B is observed, trending with the proposed onset of the region of the glass composite identified above.

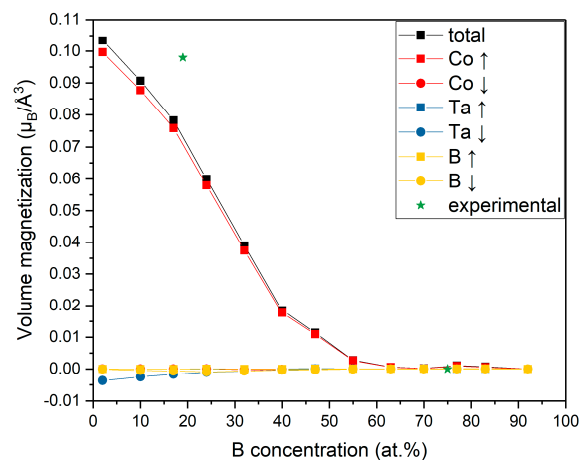


Figure 7. Volume magnetization of $(\text{Co}_{6.8\pm 3.9}\text{Ta})_{100-x}\text{B}_x$ as a function of B concentration based on ab initio calculations. The partial contributions are divided into spin-up and spin-down electrons. Green stars represent experimental values (B concentration 19 and 75 at.%).

Comparing the ab initio volume magnetization with experimental values, the measured near zero saturation magnetization for a sample with 75 at.% B agrees very well with the ab initio data. For a sample with 19 at.% B, the measured saturation volume magnetization of $0.098 \mu_B/\text{\AA}^3$ is 25 % larger than the ab initio volume magnetization. This enhanced volume magnetization may be caused by clustering of Co atoms in the physical sample in contrast to the homogenous distribution of Co atoms in the in-silico sample as well as by a different density. This clustering of Co atoms could lead to a phase separation as observed by Kontis et al. [11]. The volume magnetization measurement (Supplementary Figure S2) confirms the soft magnetism reported for the Co-Ta-B system [10].

The B concentration induced transition from a metallic glass to a covalent B network glass has been investigated. It is revealed that these two composition regions are separated by a concentration region where the formation of a glass composite is inferred based on the glass transition temperature T_g , topology, electronic structure, bonding and magnetization. Table 2 summarizes the critical B concentrations for the onset of a B network evolution as well as the beginning of a percolating B network based on each property.

Table 2. Summary of critical B concentrations for the onset and percolation of the B network.

Quantity	Onset B Network Evolution (at.% B)	Onset Percolating B-Network (at.% B)
Glass transition	46	59
Topology	40	70
Free-electron model	-	70
Bonding	32	77
Volume magnetization	40	70

Comparing the critical B concentrations in Table 2, the critical B concentrations for the onset of the B network evolution and percolation are consistent taking the large variety of quantities and methods as well as the discrete composition changes investigated into account. Hence, we can deduce from the mean concentration values in Table 2 that $(\text{Co}_{6.8\pm 3.9}\text{Ta})_{100-x}\text{B}_x$ is a metallic glass up to a B concentration of 39 ± 5 at.% B. For more than 69 ± 6 at.% B, the material is a network glass dominated by an amorphous icosahedra-like B network.

In between 39 ± 5 and 69 ± 6 at.% B, both metallic bonding and indicators for a B-network are observed. Hence, a glass composite is proposed consisting of metallically bonded regions and B network fragments. As the glass transition temperature changes in this composite regime, a material with defined processability may be designed by controlling the coordination and hence the fraction of icosahedral bonds. Additionally, this glass composite is promising in terms of mechanical properties, as it allows to combine the high strength and stiffness as well as plasticity of metallic glasses with the high stiffness and hardness of the amorphous borides. This combination of mechanical properties in the $(\text{Co}_{6.8\pm 3.9}\text{Ta})_{100-x}\text{B}_x$ system has been reported by Kontis et al. for a self-organized nanostructured material [11]. The self-organized formation of a nanostructure may be enabled by the coexistence of metallic and covalently bonded regions in this concentration range.

4. Conclusions

The B concentration in $(\text{Co}_{6.8\pm 3.9}\text{Ta})_{100-x}\text{B}_x$ was varied systematically from 2 to 92 at% to reveal the composition induced changes in electronic structure and topology in the transition regime between metallic glasses and network glasses. Based on topology and electronic structure, the critical B concentration for the onset of the B network evolution is identified as 39 ± 5 at.%. Below this B concentration the material is a metallic glass. At a B concentration of 69 ± 6 at.% the icosahedral-like B network is percolating the material, enclosing the metal atoms. Hence, the material is a covalent glass in this compositional range. Between 38 ± 5 and 69 ± 6 at.% we reveal the existence of a glass composite that contains metallic regions and B network fragments. We propose that by controlling

the coordination in this glass composite, soft-magnetic amorphous materials with defined plasticity and processability can be designed. Hence, further research should focus on the composition range of 38 ± 5 – 69 ± 6 at.% B to enable the design of mechanical properties in the range of the glass composite.

Supplementary Materials: The following are available online at <http://www.mdpi.com/2410-3896/5/1/18/s1>, Supplementary Figure S1: Shift of the principal peak of the structure factor with temperature, Supplementary Figure S2: Hysteresis curve of $\text{Co}_{67}\text{Ta}_{14}\text{B}_{19}$ and $\text{Co}_{21}\text{Ta}_4\text{B}_{75}$ measured at room temperature in a vibrating sample magnetometer

Author Contributions: Conceptualization, S.E. and J.M.S.; methodology, S.E.; formal analysis, S.E., S.P., A.M., M.H., D.P. and A.S.; investigation, S.E., M.H., S.E., D.M.H., L.P. and A.M.; writing—original draft preparation, S.E.; writing—review and editing, S.E., S.P., L.P., A.M., D.M.H., A.S., M.H., D.P., J.M.S.; visualization, S.E.; supervision, A.S. and J.M.S. All authors have read and agreed to the published version of the manuscript.

Funding: This research was funded by Deutsche Forschungsgemeinschaft within the SPP 1594 “Topological Engineering of Ultrastrong Glasses”, grant number SCHN 735/22-2). Financial support for the operation of the accelerator laboratory in Uppsala by VR-RFI (contract 821-2012-5144) and the Swedish Foundation for Strategic Research (SSF, contract RIF14-0053) is gratefully acknowledged.

Acknowledgments: Ab initio calculations were performed on the JARA-HPC partition part of the supercomputer CLAI X at RWTH Aachen University within the project JARA0131. Parts of this research were carried out at beamline P02.1 of the light source PETRA III at DESY, a member of the Helmholtz Association (HGF). Access and help to obtain the magnetization data using the PPMS-VSM at JCNS-2/PGI-4, Forschungszentrum Jülich GmbH, is gratefully acknowledged.

Conflicts of Interest: The authors declare no conflict of interest.

References

1. Ashby, M.; Greer, A.L. Metallic glasses as structural materials. *Scripta Mater.* **2006**, *54*, 321–326. [[CrossRef](#)]
2. Telford, M. The case for bulk metallic glass. *Mater. Today* **2004**, *7*, 36–43. [[CrossRef](#)]
3. Inoue, A.; Shen, B.; Takeuchi, A. Developments and Applications of Bulk Glassy Alloys in Late Transition Metal Base System. *Mater. Trans.* **2006**, *47*, 1275–1285. [[CrossRef](#)]
4. Gilman, J.J. Metallic glasses. *Science* **1980**, *208*, 856–861. [[CrossRef](#)]
5. Schuh, C.A.; Hufnagel, T.C.; Ramamurty, U. Mechanical behavior of amorphous alloys. *Acta Mater.* **2007**, *55*, 4067–4109. [[CrossRef](#)]
6. Greer, A.L. Metallic glasses ... on the threshold. *Mater. Today* **2009**, *12*, 14–22. [[CrossRef](#)]
7. Shen, T.D.; Schwarz, R.B. Bulk ferromagnetic glasses prepared by flux melting and water quenching. *Appl. Phys. Lett.* **1999**, *75*, 49–51. [[CrossRef](#)]
8. Wu, Y.; Hui, X.D.; Lu, Z.P.; Liu, Z.Y.; Liang, L.; Chen, G.L. Effects of metalloid elements on the glass-forming ability of Fe-based alloys. *J. Alloy. Compd.* **2009**, *467*, 187–190. [[CrossRef](#)]
9. Wang, J.; Li, R.; Hua, N.; Zhang, T. Co-based ternary bulk metallic glasses with ultrahigh strength and plasticity. *J. Mater. Res.* **2011**, *26*, 2072–2079. [[CrossRef](#)]
10. Inoue, A.; Shen, B.L.; Koshiba, H.; Kato, H.; Yavari, A.R. Ultra-high strength above 5000 MPa and soft magnetic properties of Co-Fe-Ta-B bulk glassy alloys. *Acta Mater.* **2004**, *52*, 1631–1637. [[CrossRef](#)]
11. Kontis, P.; Köhler, M.; Evertz, S.; Chen, Y.-T.; Schnabel, V.; Soler, R.; Bednarick, J.; Kirchlechner, C.; Dehm, G.; Raabe, D.; et al. Nano-laminated thin film metallic glass design for outstanding mechanical properties. *Scripta Mater.* **2018**, *155*, 73–77. [[CrossRef](#)]
12. Schnabel, V.; Köhler, M.; Music, D.; Bednarick, J.; Clegg, W.J.; Raabe, D.; Schneider, J.M. Ultra-stiff metallic glasses through bond energy density design. *J. Phys. Condens. Mat.* **2017**, *29*, 265502. [[CrossRef](#)]
13. Music, D.; Hensling, F.; Pazur, T.; Bednarick, J.; Hans, M.; Schnabel, V.; Hostert, C.; Schneider, J.M. Bonding and elastic properties of amorphous AlYB14. *Solid State Commun.* **2013**, *169*, 6–9. [[CrossRef](#)]
14. Stock, M.; Molian, P. Femtosecond pulsed laser deposition of amorphous, ultrahard boride thin films. *J. Vac. Sci. Technol. A* **2004**, *22*, 670. [[CrossRef](#)]
15. Tian, Y.; Bastawros, A.F.; Lo, C.C.H.; Constant, A.P.; Russell, A.M.; Cook, B.A. Superhard self-lubricating AlMgB14 films for microelectromechanical devices. *Appl. Phys. Lett.* **2003**, *83*, 2781–2783. [[CrossRef](#)]
16. Gupta, S.; Patel, N.; Miotello, A.; Kothari, D.C. Cobalt-Boride: An efficient and robust electrocatalyst for Hydrogen Evolution Reaction. *J. Power Sources* **2015**, *279*, 620–625. [[CrossRef](#)]
17. Hohenberg, P.; Kohn, W. Inhomogeneous Electron Gas. *Phys. Rev.* **1964**, *136*, B864–B871. [[CrossRef](#)]

18. Hostert, C.; Music, D.; Bednarcik, J.; Keckes, J.; Kapaklis, V.; Hjorvarsson, B.; Schneider, J.M. Ab initio molecular dynamics model for density, elastic properties and short range order of Co-Fe-Ta-B metallic glass thin films. *J. Phys. Condens. Mat.* **2011**, *23*, 475401. [[CrossRef](#)]
19. Ozaki, T.; Kino, H. Numerical atomic basis orbitals from H to Kr. *Phys. Rev. B* **2004**, *69*, 195113. [[CrossRef](#)]
20. Ozaki, T.; Kino, H. Efficient projector expansion for the ab initio LCAO method. *Phys. Rev. B* **2005**, *72*, 45121. [[CrossRef](#)]
21. Perdew, J.P.; Burke, K.; Ernzerhof, M. Generalized Gradient Approximation Made Simple. *Phys. Rev. Lett.* **1996**, *77*, 3865–3868. [[CrossRef](#)]
22. Kresse, G.; Furthmüller, J. Efficient iterative schemes for ab initio total-energy calculations using a plane-wave basis set. *Phys. Rev. B* **1996**, *54*, 11169–11186. [[CrossRef](#)]
23. Kresse, G.; Joubert, D. From ultrasoft pseudopotentials to the projector augmented-wave method. *Phys. Rev. B* **1999**, *59*, 1758–1775. [[CrossRef](#)]
24. Blöchl, P.E. Projector augmented-wave method. *Phys. Rev. B* **1994**, *50*, 17953–17979. [[CrossRef](#)]
25. Monkhorst, H.J.; Pack, J.D. Special points for Brillouin-zone integrations. *Phys. Rev. B* **1976**, *13*, 5188–5192. [[CrossRef](#)]
26. Hoffmann, R. How Chemistry and Physics Meet in the Solid State. *Angew. Chem. Int. Ed. Engl.* **1987**, *26*, 846–878. [[CrossRef](#)]
27. Dronskowski, R.; Bloechl, P.E. Crystal orbital Hamilton populations (COHP): Energy-resolved visualization of chemical bonding in solids based on density-functional calculations. *J. Phys. Chem.* **1993**, *97*, 8617–8624. [[CrossRef](#)]
28. Deringer, V.L.; Tchougréeff, A.L.; Dronskowski, R. Crystal orbital Hamilton population (COHP) analysis as projected from plane-wave basis sets. *J. Phys. Chem. A* **2011**, *115*, 5461–5466. [[CrossRef](#)]
29. Maintz, S.; Deringer, V.L.; Tchougréeff, A.L.; Dronskowski, R. Analytic projection from plane-wave and PAW wavefunctions and application to chemical-bonding analysis in solids. *J. Comput. Chem.* **2013**, *34*, 2557–2567. [[CrossRef](#)]
30. Maintz, S.; Deringer, V.L.; Tchougréeff, A.L.; Dronskowski, R. LOBSTER: A tool to extract chemical bonding from plane-wave based DFT. *J. Comput. Chem.* **2016**, *37*, 1030–1035. [[CrossRef](#)]
31. Schnabel, V.; Köhler, M.; Evertz, S.; Gamcova, J.; Bednarcik, J.; Music, D.; Raabe, D.; Schneider, J.M. Revealing the relationships between chemistry, topology and stiffness of ultrastrong Co-based metallic glass thin films: A combinatorial approach. *Acta Mater.* **2016**, *107*, 213–219. [[CrossRef](#)]
32. Zhang, Y.; Whitlow, H.J.; Winzell, T.; Bubb, I.F.; Sajavaara, T.; Arstila, K.; Keinonen, J. Detection efficiency of time-of-flight energy elastic recoil detection analysis systems. *Nucl. Instrum. Methods Phys. Res. Sect. B Beam Interact. Mater. Atoms* **1999**, *149*, 477–489. [[CrossRef](#)]
33. Ström, P.; Petersson, P.; Rubel, M.; Possnert, G. A combined segmented anode gas ionization chamber and time-of-flight detector for heavy ion elastic recoil detection analysis. *Rev. Sci. Instrum.* **2016**, *87*, 103303. [[CrossRef](#)]
34. Janson, M.S. *CONTES Instruction Manual*; Uppsala University: Uppsala, Sweden, 2004.
35. Dippel, A.-C.; Liermann, H.-P.; Delitz, J.T.; Walter, P.; Schulte-Schrepping, H.; Seeck, O.H.; Franz, H. Beamline P02.1 at PETRA III for high-resolution and high-energy powder diffraction. *J. Synchrotron. Radiat.* **2015**, *22*, 675–687. [[CrossRef](#)]
36. Hammersley, A.P. *FIT2D. An Introduction and Overview*; ESRF Internal Report ESRF97HA02T; European Synchrotron Radiation Source: Grenoble, France, 1997.
37. Hammersley, A.P.; Svensson, S.O.; Thompson, A. Calibration and correction of spatial distortions in 2D detector systems. *Nucl. Instrum. Meth. A* **1994**, *346*, 312–321. [[CrossRef](#)]
38. Hammersley, A.P.; Svensson, S.O.; Hanfland, M.; Fitch, A.N.; Hausermann, D. Two-dimensional detector software: From real detector to idealised image or two-theta scan. *High Press. Res.* **1996**, *14*, 235–248. [[CrossRef](#)]
39. Juhás, P.; Davis, T.; Farrow, C.L.; Billinge, S.J.L. PDFgetX3: A rapid and highly automatable program for processing powder diffraction data into total scattering pair distribution functions. *J. Appl. Crystallogr.* **2013**, *46*, 560–566. [[CrossRef](#)]
40. Biesinger, M.C.; Payne, B.P.; Grosvenor, A.P.; Lau, L.W.M.; Gerson, A.R.; Smart, R.S.C. Resolving surface chemical states in XPS analysis of first row transition metals, oxides and hydroxides: Cr, Mn, Fe, Co and Ni. *Appl. Surf. Sci.* **2011**, *257*, 2717–2730. [[CrossRef](#)]

41. Gupta, P.K.; Mauro, J.C. Composition dependence of glass transition temperature and fragility. I. A topological model incorporating temperature-dependent constraints. *J. Chem. Phys.* **2009**, *130*, 94503. [[CrossRef](#)]
42. Henke, B.L.; Gullikson, E.M.; Davis, J.C. X-Ray Interactions: Photoabsorption, Scattering, Transmission, and Reflection at $E = 50\text{--}30,000$ eV, $Z = 1\text{--}92$. *At. Data Nucl. Data Tables* **1993**, *54*, 181–342. [[CrossRef](#)]
43. Emin, D. Unusual properties of icosahedral boron-rich solids. *J. Solid State Chem.* **2006**, *179*, 2791–2798. [[CrossRef](#)]
44. Bao, R.; Chrisey, D.B. Short range order structure of amorphous B_4C boron carbide thin films. *J. Mater. Sci.* **2011**, *46*, 3952–3959. [[CrossRef](#)]
45. Lannin, J.S. Raman scattering in amorphous boron. *Solid State Commun.* **1978**, *25*, 363–366. [[CrossRef](#)]
46. Delaplane, R.G.; Dahlborg, U.; Howells, W.S.; Lundström, T. A neutron diffraction study of amorphous boron using a pulsed source. *J. Non-Cryst. Solids* **1988**, *106*, 66–69. [[CrossRef](#)]
47. Nagel, S.R.; Tauc, J. Nearly-Free-Electron Approach to the Theory of Metallic Glass Alloys. *Phys. Rev. Lett.* **1975**, *35*, 380–383. [[CrossRef](#)]
48. Kittel, C.; Hunklinger, S. *Einführung in die Festkörperphysik*, 15th ed.; unveränd. Aufl.; Oldenbourg: München, Germany, 2013; ISBN 978-3-486-59755-4.
49. Higdon, C.; Cook, B.; Harringa, J.; Russell, A.; Goldsmith, J.; Qu, J.; Blau, P. Friction and wear mechanisms in $AlMgB_{14}\text{-TiB}_2$ nanocoatings. *Wear* **2011**, *271*, 2111–2115. [[CrossRef](#)]
50. Mavel, G.; Escard, J.; Costa, P.; Castaing, J. ESCA surface study of metal borides. *Surf. Sci.* **1973**, *35*, 109–116. [[CrossRef](#)]
51. Wang, Y.; Fan, J.; Trenary, M. Surface chemistry of boron oxidation. 1. Reactions of oxygen and water with boron films grown on tantalum(110). *Chem. Mater.* **1993**, *5*, 192–198. [[CrossRef](#)]
52. Hasegawa, R.; Ray, R. Magnetization of glassy Co-B alloys. *J. Appl. Phys.* **1979**, *50*, 1586–1588. [[CrossRef](#)]



© 2020 by the authors. Licensee MDPI, Basel, Switzerland. This article is an open access article distributed under the terms and conditions of the Creative Commons Attribution (CC BY) license (<http://creativecommons.org/licenses/by/4.0/>).

Paper IV

Effect of the free volume on the electronic structure of Cu₇₀Zr₃₀ metallic glasses

S. Evertz and J. M. Schneider

Materials **13(21)**, 4911 (2020), doi: 10.3390/ma13214911

Article

Effect of the Free Volume on the Electronic Structure of $\text{Cu}_{70}\text{Zr}_{30}$ Metallic Glasses

Simon Evertz *  and Jochen M. Schneider

Materials Chemistry, RWTH Aachen University, Kopernikusstr 10, D-52074 Aachen, Germany; schneider@mch.rwth-aachen.de

* Correspondence: evertz@mch.rwth-aachen.de

Received: 28 September 2020; Accepted: 29 October 2020; Published: 31 October 2020



Abstract: While it is accepted that the plastic behavior of metallic glasses is affected by their free volume content, the effect on chemical bonding has not been investigated systematically. According to electronic structure analysis, the overall bond strength is not significantly affected by the free volume content. However, with an increasing free volume content, the average coordination number decreases. Furthermore, the volume fraction of regions containing atoms with a lower coordination number increases. As the local bonding character changes from bonding to anti-bonding with a decreasing coordination number, bonding is weakened in the volume fraction of a lower coordination number. During deformation, the number of strong, short-distance bonds decreases more for free volume-containing samples than for samples without free volume, resulting in additional bond weakening. Therefore, we show that the introduction of free volume causes the formation of volume fractions of a lower coordination number, resulting in weaker bonding, and propose that this is the electronic structure origin of the enhanced plastic behavior reported for glasses containing free volume.

Keywords: metallic glass; free volume; electronic structure; ab initio

1. Introduction

Plastic deformability is crucial for structural applications of metallic glasses [1]. Increasing the free volume content has been proposed to enhance the plastic deformation of metallic glasses and is often referred to as “structural rejuvenation” [2]. Recently, an enhanced free volume content was reported to induce work hardening and hence enable stable plastic deformation [3].

Free volume is inherent to the glassy state, as its density varies depending on the synthesis conditions [2], and consists of volume fractions containing atoms with a lower coordination number [4], allowing the atoms to move within their nearest neighbor cage without energy change [5]. Therefore, the atomic mobility is enhanced [4,6] as the free volume lowers the energy barrier for shear transformations in metallic glasses [4,6], promoting plastic deformability [7]. While the literature often focusses on free volume-induced changes in internal energy [2,7–10] and topology [3,11–13], the effect of free volume on the electronic structure has been overlooked thus far. $\text{Cu}_{70}\text{Zr}_{30}$ metallic glasses have previously been predicted to be brittle based on ab initio methods [14,15]. Therefore, the goal of this study is to understand the effect of free volume on the electronic structure and hence chemical bonding based on ab initio calculations by systematically increasing the free volume content of $\text{Cu}_{70}\text{Zr}_{30}$.

2. Methods

Density-functional-theory (DFT)-based [16] ab initio molecular dynamics calculations were carried out in this work. To create glassy structural models, the modeling routine introduced by Hostert et al. [17] was employed. The initial supercell contained 115 atoms, which were initially

randomly distributed on a bcc-lattice (115 atoms and 13 vacancies) [17]. This supercell was heated up with a timestep of 1 fs to 4000 K for 400 fs in a canonical ensemble by the scaling of velocities and subsequently quenched to 0 K by geometry relaxation employing the openMX 3.9.2 code [18,19]. Electronic potentials with the general gradient approximation [20] and the basic functions Cu6.0S-s3p3d3 and Zr7.0-s3p3d3f1 were applied, where the first symbol designated the chemical element and cutoff-radius and the last set of symbols defined the primitive orbitals. A $1 \times 1 \times 1$ k-grid and an energy cutoff-radius of 150 Ry were used. After quenching to 0 K, the volume was relaxed by employing the Vienna Ab initio Simulation Package (VASP) [21,22] with projector-augmented wave potentials [22,23] using the Perdew–Burke–Ernzerhof functional [20]. Integration over the Brillouin zone was conducted on a $3 \times 3 \times 3$ Monkhorst–Pack k-grid [24]. This heating–quenching–relaxation cycle described above was repeated until the volume change between two subsequent cycles was smaller than 2%.

To create different free volume contents, up to five atoms were removed from the amorphous structural model while keeping the composition approximately constant. To avoid a vacancy-like atomic configuration around the position of the removed atom, the supercell was heated to 4000 K for 400 fs by velocity scaling in a canonical ensemble and subsequently quenched to 0 K by geometry relaxation. This allowed the free volume to distribute within the supercell. To probe the significance and reproducibility of the observed results, four independent structural models were developed from the initial crystalline supercell up to the free volume-containing supercells.

The bulk modulus was calculated from the ground state by fitting the energy–volume data with the Birch–Munaghan equation of state [25], and the shear modulus was calculated using volume-conserving distortions [26]. To calculate pair distribution functions, taking the atomic scattering factors into account [17], the supercell was heated to 300 K for 300 fs. The pair distribution functions were averaged over the last 200 fs. For bonding analysis, the crystal orbital Hamilton populations (COHPs) [27] were obtained from the LOBSTER code (version 3.2.0) [28–30].

3. Results and Discussion

Before the electronic structure and topology are analysed, the changes of total energy and elastic moduli as a function of increasing free volume content are investigated and are shown in Figure 1. The variability range indicated does not represent the numerical error of the calculation, but the variability of plus and minus one standard deviation of the average of the properties listed in Table 1, which were obtained for the different structural models investigated in the study.

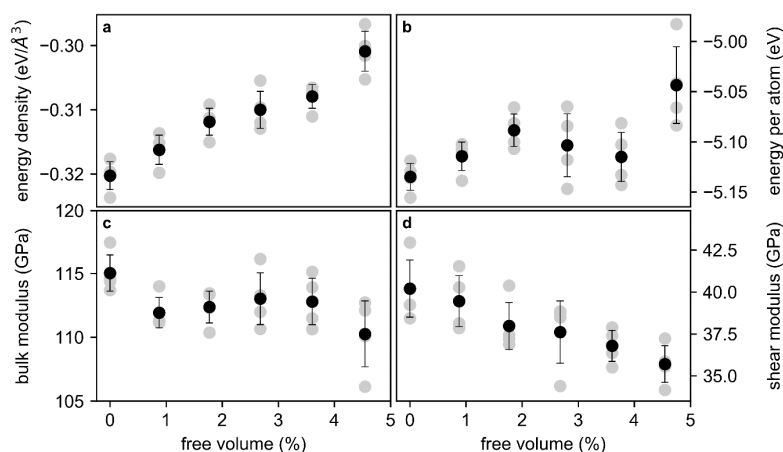


Figure 1. Ab initio total energy density (a), energy per atom (b), bulk modulus (c), and shear modulus (d) of Cu₇₀Zr₃₀. Gray symbols mark the result of a single calculation and black symbols mark the average of the data points per free volume content, while the variability bars represent plus and minus one standard deviation of the average value of the properties listed in Table 1, which were obtained for the different structural models investigated in the study.

Table 1. Free volume, total energy, energy per atom, supercell volume, energy density, and bulk and shear modulus of the four structural models developed in this study.

Free Volume (%)	Total Energy (eV)	Energy per Atom (eV/Atom)	Supercell Volume (Å ³)	Energy Density (eV/Å ³)	Bulk Modulus (GPa)	Shear Modulus (GPa)
Structural model 1						
0.0	−590.6	−5.12	1847.5	−0.320	114.4	39.2
0.9	−582.2	−5.11	1847.5	−0.315	111.3	37.9
1.8	−576.3	−5.10	1847.5	−0.312	113.4	37.2
2.7	−576.4	−5.14	1847.5	−0.312	116.1	38.7
3.6	−566.4	−5.10	1847.5	−0.307	111.5	35.5
4.5	−548.1	−4.98	1847.5	−0.297	106.1	35.9
Structural model 2						
0.0	−589.9	−5.13	1857.0	−0.317	113.7	40.2
0.9	−582.5	−5.11	1857.0	−0.314	111.3	38.1
1.8	−574.2	−5.08	1857.0	−0.309	112.3	36.9
2.7	−567.3	−5.06	1857.0	−0.305	112.0	34.4
3.6	−570.9	−5.14	1857.0	−0.307	115.1	37.4
4.5	−557.3	−5.06	1857.0	−0.300	112.1	34.2
Structural model 3						
0.0	−592.9	−5.16	1831.8	−0.324	114.9	43.0
0.9	−585.8	−5.14	1831.8	−0.320	111.1	41.5
1.8	−577.1	−5.11	1831.8	−0.315	108.3	40.4
2.7	−573.2	−5.12	1831.8	−0.313	103.7	38.5
3.6	−569.8	−5.13	1831.8	−0.311	102.3	37.9
4.5	−559.2	−5.08	1831.8	−0.305	96.5	35.6
Structural model 4						
0.0	−588.7	−5.12	1839.0	−0.320	114.6	38.4
0.9	−581.7	−5.10	1839.0	−0.316	111.2	40.3
1.8	−572.4	−5.07	1839.0	−0.311	110.4	37.4
2.7	−569.4	−5.08	1839.0	−0.309	110.7	38.8
3.6	−564.0	−5.08	1839.0	−0.307	110.6	36.4
4.5	−554.6	−5.04	1839.0	−0.302	110.1	37.2

The free volume is the excess mean atomic volume compared to the reference structural model that is based on a supercell containing 115 atoms, which has a free volume content of 0% per definition. The internal energy of the glass is represented here as the energy density and energy per atom (Figure 1a,b). The energy density is used to normalize the total energy of the structural models with the same free volume content, as the absolute volumes of the structural models are not identical. With the free volume content increasing by 4.6%, the energy density increased by 6.4% and the energy per atom by 1.8%. This increase of energy is larger than the variability between the structural models and is consistent with the literature [2,31]. However, the internal energy at free volume contents of 2.7 and 3.6% deviates to lower energies from the increasing internal energy observed before.

The bulk modulus (Figure 1c) varies from 110 to 115 GPa and hence by 4.3%. This small change of the bulk modulus with an increasing free volume content reflects bond weakening. The shear modulus (Figure 1d) decreases linearly by 10% with an increasing free volume content. Therefore, the energy barrier for shear transformations decreases [32], which is consistent with the increased internal energy [8]. The effect of the free volume on the resistance to hydrostatic deformation is small but significant.

To reveal the effect of an increasing free volume on the electronic structure, partitioning of the bond energy is analysed: The COHPs of the three structural models, which are based on different initial configurations, are similar (Figure 2a–c), showing bonding contributions below approx. −2.5 eV and anti-bonding contributions close to the Fermi level. However, it is evident that with an increasing free volume content, the COHPs are shifting towards the Fermi level, which is indicated by the arrows in Figure 2a–c and is further visualized by the free volume-induced changes of the center of gravity (CoG) of the COHP and the electronic density of states (DOS, Figure S1) depicted in Figure 2d,e, as calculated by Equation (1).

$$\text{CoG}_X = \frac{\int (X \cdot E) dE}{\int X dE} \quad (1)$$

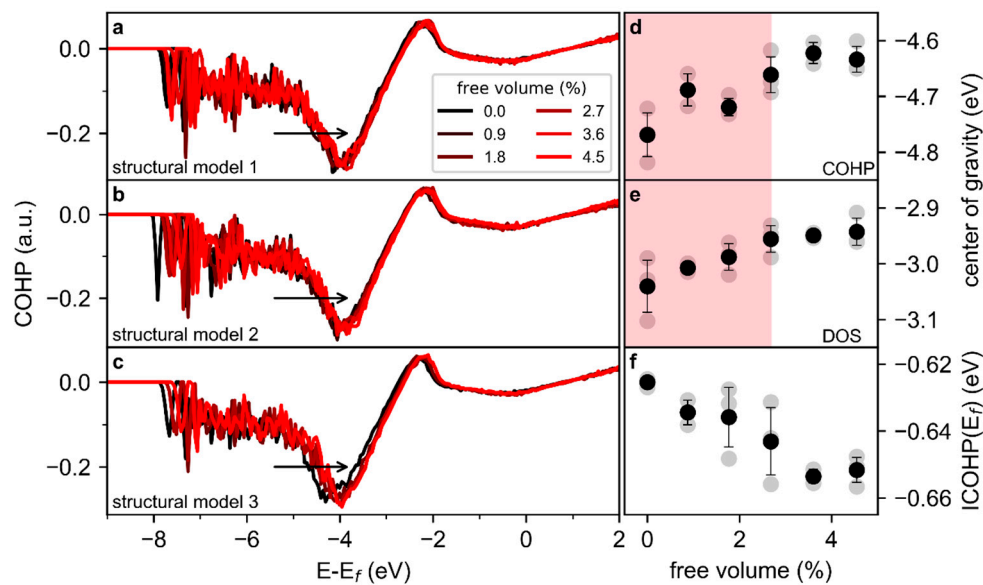


Figure 2. Global bonding analysis of free volume-containing $\text{Cu}_{70}\text{Zr}_{30}$. Crystal orbital Hamilton population (COHP) of three $\text{Cu}_{70}\text{Zr}_{30}$ metallic glass structural models (a–c). Free volume-induced changes in the integrated COHP up to the Fermi level, in the center of gravity of the COHP, and in the density of states are depicted in (d–f), respectively. In (d–f), black symbols indicate the average of the quantities based on all structural models, and gray symbols indicate the values of the individual calculations. The variability bars indicate the range of plus and minus one standard deviation from the average value obtained for the different structural models investigated in this study.

Here, X is the COHP or DOS, respectively, and E is the energy of the electronic states. For free volume contents up to 2.7%, the CoG shift towards the Fermi level is larger than the variation of data at a constant free volume (red shaded area in Figure 2d,e). However, for free volume contents larger than 2.7%, the shift of the CoG is smaller than the variation at a constant free volume and hence, the CoG remains constant with respect to the Fermi level. This is in line with the critical free volume content for yielding of metallic glasses proposed by Wang et al. [33].

The integrated COHP (ICOHP) at the Fermi level, which is a measure of the bond strength [29], exhibits a subtle decreasing trend and strongly dispersed data (Figure 2f). The difference in ICOHP between the minimum and maximum free volume contents (0.0 and 4.6%) is -0.3 meV/atom. Due to the numerical precision of *ab initio* calculations [34] and the orthogonal projection of the electrons [29], this difference is appraised as not significant, while the scattering within the set of calculations analysed here indicates a slightly decreasing ICOHP with an increasing free volume content. Therefore, while the electrons occupy higher energetic electronic states with an increased free volume content, the analysis of the total COHP confirms that the effect of the free volume on the overall bond strength is small but significant.

To investigate the influence of the free volume on directional and non-directional bonds spatially resolved, the COHPs are separated into the contributions of the electronic bands of the $\text{Cu}_{70}\text{Zr}_{30}$ samples with free volume contents of 4.6% (Figure 3a–c) and 0.0% (Figure 3d–f). As the total COHPs of the structural models are consistent (Figure 2a–c) and due to computational constraints, the band-resolved analysis has been conducted only for structural model 1. Based on the electronic band contributions (Figure 3a,b,d,e), the interactions between the s -bands (s - s), the s - and d -bands (s - d), and the d -bands (d - d) are dominating the bonding in $\text{Cu}_{70}\text{Zr}_{30}$. As observed for the total COHPs (Figure 2a–c), only minor differences exist between the COHPs for the same structural model but different free volume contents. Therefore, both directional (s - d and d - d bonds) and non-directional bonding (s - s [35]) is affected in a similar way by the free volume. However, the COHPs for low coordination numbers exhibit less bonding states below -2.5 eV, as well as an enhanced number of anti-bonding states

between -1.5 eV and the Fermi level (Figure 3c,f). As this analysis indicates that the local atomic structure predominantly affects the bonding, the effect of the free volume on the local bonding is probed next.

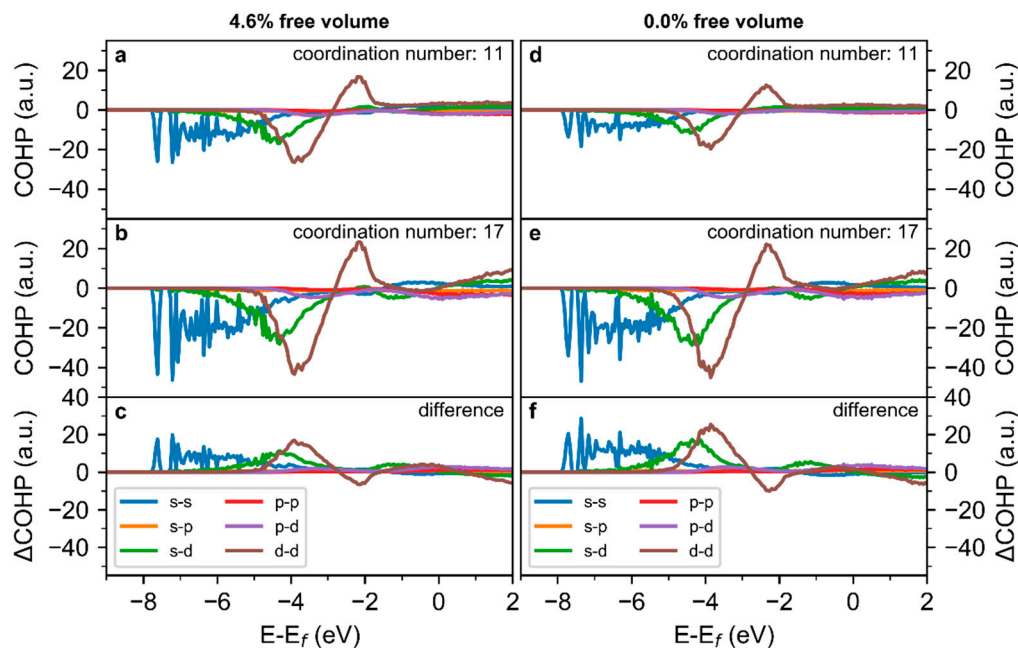


Figure 3. Band-resolved COHP of $\text{Cu}_{70}\text{Zr}_{30}$ metallic glass with a (a–c) 4.6% and (d–f) 0.0% free volume content. (a,d) show the COHP for atoms with a coordination number of 11, (b,e) for a coordination number of 17, and (c,f) the difference between a low and high coordination number.

To this end, the distribution of coordination numbers, i.e., the number of neighbors of an atom within the first coordination shell, which is discussed later in Figure 6, is analysed by comparing the simulation cell containing no free volume with the one containing a 4.6% free volume, as presented in Figure 4a. The range of coordination numbers observed is consistent with the literature [36]. The average coordination number decreases from 14.2 to 13.5 as free volume is introduced. To visualize the impact of the free volume on the spatial distribution of coordination numbers, iso-coordination surfaces that enclose volume sections containing atoms with a coordination number ≤ 12 are shown in the simulation cell in Figure 4b,c. In the configuration without free volume (Figure 4b), these iso-coordination sections are partly interconnected and populate 11.3% of the volume of the supercell. With an increased free volume content of 4.6% (Figure 4c), the volume fraction of the iso-coordination sections increases by 11.8%. Therefore, the introduction of a 4.6% free volume causes the volume fraction containing atoms with coordination numbers ≤ 12 to increase to 23.1%.

The analysis of the $\text{ICOHP}(E_f)$ of individual atoms as a function of the coordination number (Figure 5) emphasizes the bond weakening in regions of a low coordination number: Atoms with a coordination number ≤ 14 exhibit a positive $\text{ICOHP}(E_f)$ and hence overall anti-bonding interactions. Therefore, the bonding in the volume fraction with a coordination number ≤ 14 is weakened. For more densely packed atoms with a coordination number > 14 and larger, the $\text{ICOHP}(E_f)$ is negative. Hence, interactions with the nearest neighbors for atoms with a coordination number > 14 are bonding strongly. The magnitude of the bond energy range for coordination numbers between 14 and 17 may originate from the inherent structural heterogeneities of metallic glasses [6]. From Figure 5, it is clearly visible that the $\text{ICOHP}(E_f)$ as a function of the coordination number is independent on the overall free volume content in the sample. However, it is also evident that the number of weakened bonds clearly increases due to the shift of the coordination number distribution to lower values and the increasing volume fraction of regions containing atoms with a lower coordination number. This is consistent

with the reduced shear modulus (Figure 1), and the reported lowered activation energy for shear transformations [4,6].

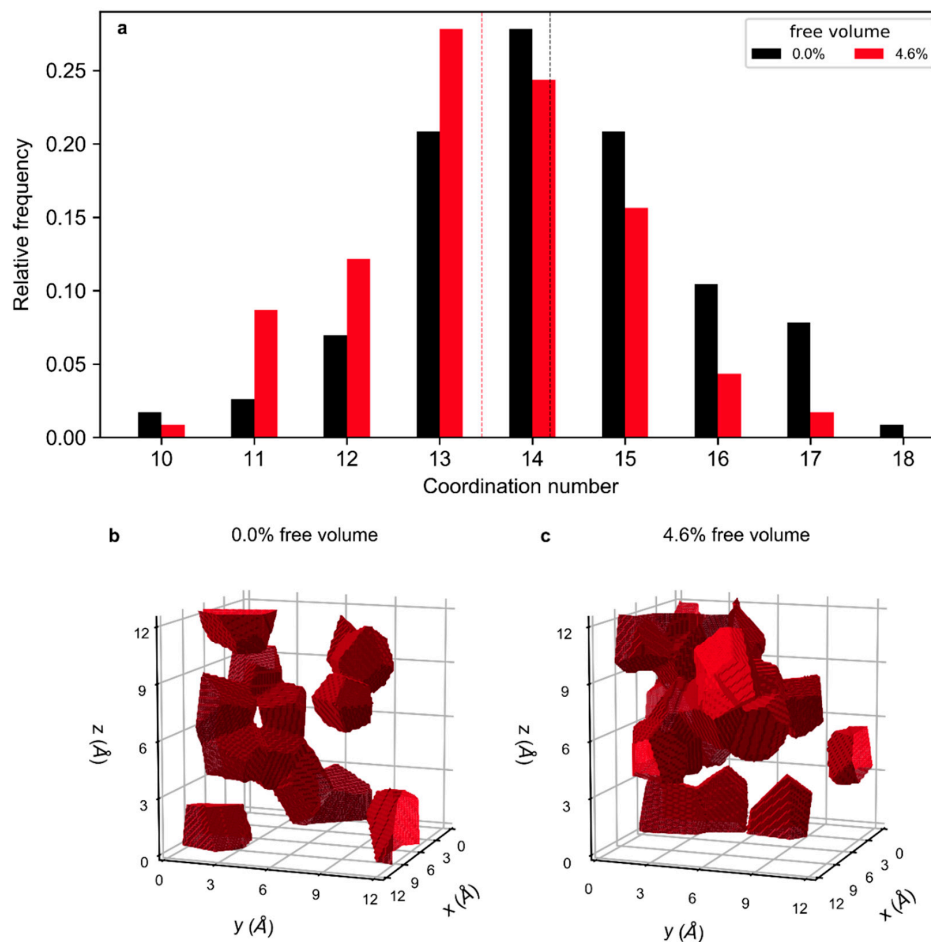


Figure 4. Global and spatially resolved coordination number analysis. (a) Relative frequency of occurrence of a coordination number in the sample. Black bars represent the coordination number of a sample with a 0.0% free volume content, and red bars of a sample with a 4.6% free volume content. Dashed lines mark the respective average coordination number. Iso-configuration surfaces enclosing regions with a coordination number of 12 and lower in the simulation cell for a glass with a 0.0% and 4.6% free volume are shown in (b,c), respectively.

To analyse the effect of the free volume on the short-range order, the pair distribution function (PDF) of an undeformed, a 2% sheared, and a 2% hydrostatically expanded glass with a 4.6% free volume content (Figure 6a) and 0% free volume (Figure 6b) are compared by showing the difference in the PDF in Figure 6c. To enlarge the overall sample size, the average of three independently calculated configurations is shown in Figure 6. The complete pair distribution functions presented in Figure S2 clearly show the lack of long-range order in the samples. The bond distances of 2.5, 2.75, and 3.2 Å for Cu-Cu, Cu-Zr, and Zr-Zr, respectively, are consistent with the literature [36,37] within 0.15 Å, which has been reported for ab initio structural models of metallic glasses before [38]. However, as the deviation from the literature is consistent throughout the structural models investigated and this analysis is based on a comparison with the structural model without free volume as a reference, the conclusions from this study are considered valid. While the bond distribution is similar for deformed and undeformed, free-volume-containing and free-volume-free samples, small changes can be observed in the difference curve (Figure 6c): With an increased free volume content, the number of bonds is reduced for the sheared and hydrostatically deformed cells. While this effect is small, the variability bands of the PDF of the sheared and hydrostatically deformed samples do not overlap completely with the variability

band of the reference PDF, indicating a decreased number of bonds. Therefore, the effect of the free volume content on the number of bonds is small but significant.

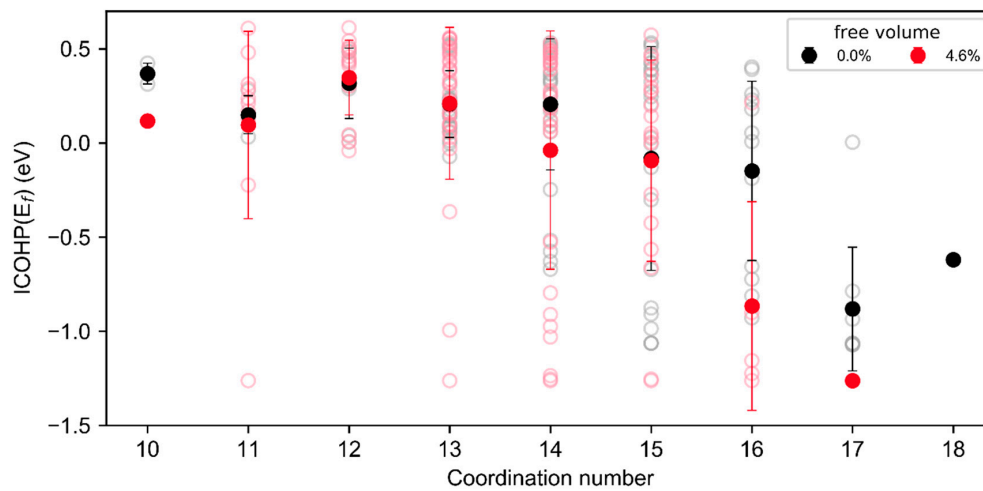


Figure 5. Integrated COHP (ICOHP)(E_f) as a function of the atomic coordination number. Full points mark the mean ICOHP at each coordination number and variability bars indicate plus and minus one standard deviation from the average of all bonds with the respective coordination number. Open symbols mark the ICOHP(E_f) of the individual atoms considered.

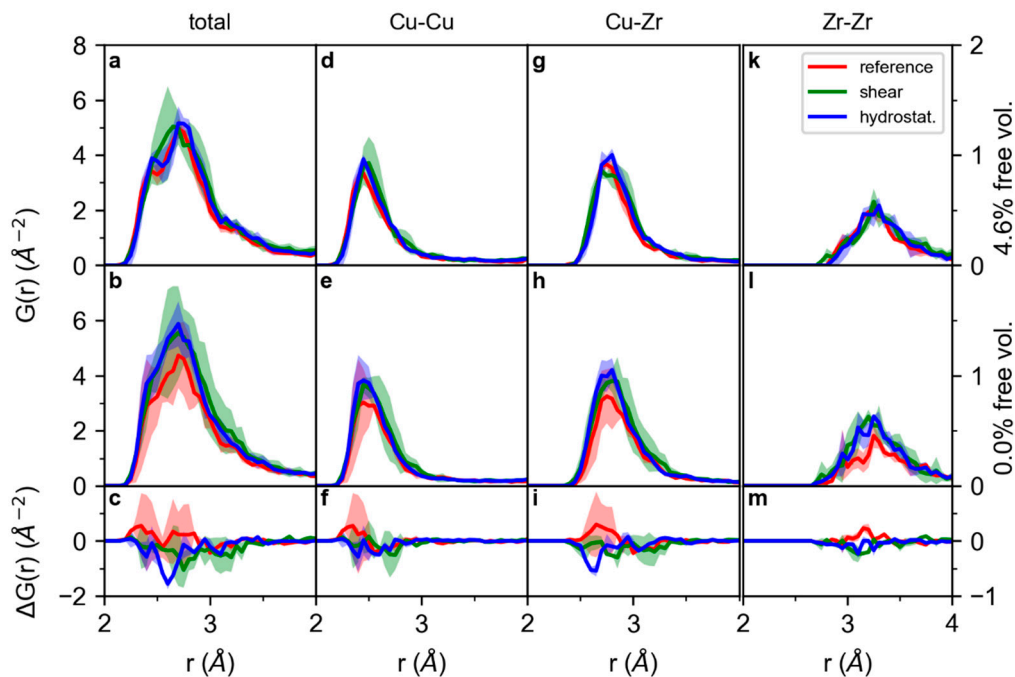


Figure 6. Total pair distribution functions of $\text{Cu}_{70}\text{Zr}_{30}$ of the undeformed, 2% sheared, and 2% hydrostatically enlarged cells for a sample containing a 4.6% free volume (a) and 0.0% free volume (b) and the difference in the pair distribution functions with a 4.6% and 0.0% free volume (c). (d–f) present the corresponding partial pair distribution functions for Cu–Cu, (g–i) Cu–Zr, and (k–m) Zr–Zr bonds. The pair distribution functions (PDFs) shown are the average of three independently calculated samples to enlarge the overall sample size. Shaded areas represent the variability obtained for the different structural models investigated in this study.

By not only comparing the total PDFs, but also focusing on the partial Cu-Cu PDFs (Figure 6d–f), Cu-Zr PDFs, (Figure 6g–i) and Zr-Zr PDFs (Figure 6k–m), the bond depletion discussed for the total PDF can be observed in the partial Cu-Cu and Cu-Zr PDFs, which are the main contributors to the total PDF: While the deformation-induced bond depletion with an increased free volume content is not significant for Cu-Cu bonds (Figure 6f), the number of Cu-Zr bonds in the hydrostatically deformed samples is reduced on the short bond-distance side of the first peak of the PDF for the free volume-containing glass compared to the glass without free volume. However, for the undeformed cell, a larger peak, i.e., a larger number of bonds, is observed for Cu-Cu and Cu-Zr in the free volume-containing cell (Figure 6f,i), while during deformation, these additional bonds are no longer present. For the Zr-Zr bonds (Figure 6k–m), a small increase in the number of bonds with free volume content in the undeformed cell is observed, while the effect of deformation on the number of bonds for the free volume-containing system compared to the system without free volume is minor.

Hence, small topological differences between 0.0 and 4.6% free volume-containing samples are observed: The number of bonds in the short-range order increases with the free volume content for undeformed systems, while for shear and hydrostatic deformation, the number of short-distance and hence strong bonds in the short-range order is reduced more for free volume-containing systems than for systems without free volume. This originates from a deformation-induced depletion in the number of Cu-Zr bonds. The observed changes in topology are consistent with the weaker bonding under shear deformation proposed based on the electronic structure analysis and the reported decreased barrier for shear transformations [4,5].

4. Conclusions

A systematic, ab initio calculation-based comparison of Cu₇₀Zr₃₀ metallic glasses with free volume contents varying from 0.0% to 4.6% revealed that the overall bond strength based on the integrated COHP changes marginally with an increasing free volume content, while the populated electronic states and bond energy contributions shift by 0.1 eV to higher energies. However, the average coordination number decreases from 14.2 to 13.5 with an increasing free volume content from 0.0 to 4.6%, since the volume fraction of regions containing atoms with a coordination number ≤ 12 increases significantly: For samples without free volume, the volume fraction of regions containing atoms with a coordination number ≤ 12 occupies 11.3% of the simulation cell volume, while this volume fraction increases to 23.1% for glasses with a 4.6% free volume content. Due to an increasing number of anti-bonding contributions to the local bonding with a decreasing coordination number, the ICOHP(E_f) exhibits positive bonds of atoms with coordination numbers ≤ 14 , indicating the dominance of anti-bonding contributions. Therefore, the bonding is weakened locally in the volume fraction of lower coordination. Topology-wise, under shear and hydrostatic deformation, free volume-containing samples show a larger decrease in strong, short-distance bonds with an increased free volume than samples without free volume, indicating additional bond weakening. Therefore, the introduction of free volume causes the formation of volume fractions of lower coordination. Due to a local rise of anti-bonding states in these volume fractions of lower coordination, bonding is weakened. We propose that this local bond weakening is the electronic structure origin of the enhanced plastic behavior reported for free volume-containing metallic glasses.

Supplementary Materials: The following are available online at <http://www.mdpi.com/1996-1944/13/21/4911/s1>: Figure S1: Density of states of Cu₇₀Zr₃₀ metallic glasses with different free volume contents. Figure S2: Pair distribution functions of Cu₇₀Zr₃₀ structural models containing different amounts of free volume.

Author Contributions: Conceptualization, S.E. and J.M.S.; formal analysis, S.E.; investigation, S.E.; writing—original draft preparation, S.E.; writing—review and editing, J.M.S.; visualization, S.E.; supervision, J.M.S.; funding acquisition, J.M.S. All authors have read and agreed to the published version of the manuscript.

Funding: This research was funded by the German Research Foundation, grant number SCHN 735/22-2, within the SPP 1594 “Topological engineering of Ultrastrong Glasses”.

Acknowledgments: Ab initio calculations were performed in the JARA-HPC partition part of the supercomputer CLAIX at RWTH Aachen University within the project JARA0131. We thank D. Bogdanovski for fruitful discussions on the bonding analysis using COHP.

Conflicts of Interest: The authors declare no conflict of interest.

References

1. Ashby, M.; Greer, A.L. Metallic glasses as structural materials. *Scr. Mater.* **2006**, *54*, 321–326. [[CrossRef](#)]
2. Sun, Y.; Concustell, A.; Greer, A.L. Thermomechanical processing of metallic glasses: Extending the range of the glassy state. *Nat. Rev. Mater.* **2016**, *1*, 16039. [[CrossRef](#)]
3. Pan, J.; Ivanov, Y.P.; Zhou, W.H.; Li, Y.; Greer, A.L. Strain-hardening and suppression of shear-banding in rejuvenated bulk metallic glass. *Nature* **2020**, *578*, 559–562. [[CrossRef](#)] [[PubMed](#)]
4. Argon, A.S. Plastic deformation in metallic glasses. *Acta Metall.* **1979**, *27*, 47–58. [[CrossRef](#)]
5. Spaepen, F. A microscopic mechanism for steady state inhomogeneous flow in metallic glasses. *Acta Metall.* **1977**, *25*, 407–415. [[CrossRef](#)]
6. Egami, T.; Iwashita, T.; Dmowski, W. Mechanical Properties of Metallic Glasses. *Metals* **2013**, *3*, 77–113. [[CrossRef](#)]
7. Li, N.; Liu, L.; Chen, Q.; Pan, J.; Chan, K.C. The effect of free volume on the deformation behaviour of a Zr-based metallic glass under nanoindentation. *J. Phys. D Appl. Phys.* **2007**, *40*, 6055–6059. [[CrossRef](#)]
8. Slipenyuk, A.; Eckert, J. Correlation between enthalpy change and free volume reduction during structural relaxation of Zr₅₅Cu₃₀Al₁₀Ni₅ metallic glass. *Scr. Mater.* **2004**, *50*, 39–44. [[CrossRef](#)]
9. Haruyama, O.; Nakayama, Y.; Wada, R.; Tokunaga, H.; Okada, J.; Ishikawa, T.; Yokoyama, Y. Volume and enthalpy relaxation in Zr₅₅Cu₃₀Ni₅Al₁₀ bulk metallic glass. *Acta Mater.* **2010**, *58*, 1829–1836. [[CrossRef](#)]
10. Evenson, Z.; Busch, R. Equilibrium viscosity, enthalpy recovery and free volume relaxation in a Zr₄₄Ti₁₁Ni₁₀Cu₁₀Be₂₅ bulk metallic glass. *Acta Mater.* **2011**, *59*, 4404–4415. [[CrossRef](#)]
11. Yavari, A.R.; Le Moulec, A.; Inoue, A.; Nishiyama, N.; Lupu, N.; Matsubara, E.; Botta, W.J.; Vaughan, G.; Di Michiel, M.; Kvick, Å. Excess free volume in metallic glasses measured by X-ray diffraction. *Acta Mater.* **2005**, *53*, 1611–1619. [[CrossRef](#)]
12. Fan, C.; Liu, C.T.; Chen, G.; Liaw, P.K. Quantitatively defining free-volume, interconnecting-zone and cluster in metallic glasses. *Intermetallics* **2015**, *57*, 98–100. [[CrossRef](#)]
13. Ye, J.C.; Lu, J.; Liu, C.T.; Wang, Q.; Yang, Y. Atomistic free-volume zones and inelastic deformation of metallic glasses. *Nat. Mater.* **2010**, *9*, 619–623. [[CrossRef](#)]
14. Schnabel, V.; Jaya, B.N.; Köhler, M.; Music, D.; Kirchlechner, C.; Dehm, G.; Raabe, D.; Schneider, J.M. Electronic hybridisation implications for the damage-tolerance of thin film metallic glasses. *Sci. Rep.* **2016**, *6*, 36556. [[CrossRef](#)] [[PubMed](#)]
15. Evertz, S.; Kirchlechner, I.; Soler, R.; Kirchlechner, C.; Kontis, P.; Bednarcik, J.; Gault, B.; Dehm, G.; Raabe, D.; Schneider, J.M. Electronic structure based design of thin film metallic glasses with superior fracture toughness. *Mater. Design* **2020**, *186*, 108327. [[CrossRef](#)]
16. Hohenberg, P.; Kohn, W. Inhomogeneous Electron Gas. *Phys. Rev.* **1964**, *136*, B864–B871. [[CrossRef](#)]
17. Hostert, C.; Music, D.; Bednarcik, J.; Keckes, J.; Kapaklis, V.; Hjorvarsson, B.; Schneider, J.M. Ab initio molecular dynamics model for density, elastic properties and short range order of Co-Fe-Ta-B metallic glass thin films. *J. Phys. Condens. Mat.* **2011**, *23*, 475401. [[CrossRef](#)]
18. Ozaki, T.; Kino, H. Numerical atomic basis orbitals from H to Kr. *Phys. Rev. B* **2004**, *69*, 195113. [[CrossRef](#)]
19. Ozaki, T.; Kino, H. Efficient projector expansion for the ab initio LCAO method. *Phys. Rev. B* **2005**, *72*, 45121. [[CrossRef](#)]
20. Perdew, J.P.; Burke, K.; Ernzerhof, M. Generalized Gradient Approximation Made Simple. *Phys. Rev. Lett.* **1996**, *77*, 3865–3868. [[CrossRef](#)]
21. Kresse, G.; Furthmüller, J. Efficient iterative schemes for ab initio total-energy calculations using a plane-wave basis set. *Phys. Rev. B* **1996**, *54*, 11169–11186. [[CrossRef](#)] [[PubMed](#)]
22. Kresse, G.; Joubert, D. From ultrasoft pseudopotentials to the projector augmented-wave method. *Phys. Rev. B* **1999**, *59*, 1758–1775. [[CrossRef](#)]
23. Blöchl, P.E. Projector augmented-wave method. *Phys. Rev. B* **1994**, *50*, 17953–17979. [[CrossRef](#)] [[PubMed](#)]

24. Monkhorst, H.J.; Pack, J.D. Special points for Brillouin-zone integrations. *Phys. Rev. B* **1976**, *13*, 5188–5192. [[CrossRef](#)]
25. Birch, F. Finite strain isotherm and velocities for single-crystal and polycrystalline NaCl at high pressures and 300° K. *J. Geophys. Res.* **1978**, *83*, 1257. [[CrossRef](#)]
26. Music, D.; Takahashi, T.; Vitos, L.; Asker, C.; Abrikosov, I.A.; Schneider, J.M. Elastic properties of Fe–Mn random alloys studied by ab initio calculations. *Appl. Phys. Lett.* **2007**, *91*, 191904. [[CrossRef](#)]
27. Dronskowski, R.; Bloechl, P.E. Crystal orbital Hamilton populations (COHP): Energy-resolved visualization of chemical bonding in solids based on density-functional calculations. *J. Phys. Chem.* **1993**, *97*, 8617–8624. [[CrossRef](#)]
28. Deringer, V.L.; Tchougréeff, A.L.; Dronskowski, R. Crystal orbital Hamilton population (COHP) analysis as projected from plane-wave basis sets. *J. Phys. Chem. A* **2011**, *115*, 5461–5466. [[CrossRef](#)]
29. Maintz, S.; Deringer, V.L.; Tchougréeff, A.L.; Dronskowski, R. Analytic projection from plane-wave and PAW wavefunctions and application to chemical-bonding analysis in solids. *J. Comput. Chem.* **2013**, *34*, 2557–2567. [[CrossRef](#)]
30. Maintz, S.; Deringer, V.L.; Tchougréeff, A.L.; Dronskowski, R. LOBSTER: A tool to extract chemical bonding from plane-wave based DFT. *J. Comput. Chem.* **2016**, *37*, 1030–1035. [[CrossRef](#)]
31. Spaepen, F. Homogeneous flow of metallic glasses: A free volume perspective. *Scr. Mater.* **2006**, *54*, 363–367. [[CrossRef](#)]
32. Dyre, J.C.; Wang, W.H. The instantaneous shear modulus in the shoving model. *J. Chem. Phys.* **2012**, *136*, 224108. [[CrossRef](#)] [[PubMed](#)]
33. Wang, J.G.; Zhao, D.Q.; Pan, M.X.; Wang, W.H.; Song, S.X.; Nieh, T.G. Correlation between onset of yielding and free volume in metallic glasses. *Scr. Mater.* **2010**, *62*, 477–480. [[CrossRef](#)]
34. Lejaeghere, K.; van Speybroeck, V.; van Oost, G.; Cottenier, S. Error Estimates for Solid-State Density-Functional Theory Predictions: An Overview by Means of the Ground-State Elemental Crystals. *Crit. Rev. Solid State Mater. Sci.* **2014**, *39*, 1–24. [[CrossRef](#)]
35. Carter, F.L. On Deriving Density of States Information from Chemical Bond Considerations. In *Electronic Density of States Based on Invited and Contributed Papers and Discussion, 3rd Materials Research Symposium*; Bennet, L.H., Ed.; NBS Special Publication: Washington, DC, USA, 1971; pp. 385–405.
36. Li, F.; Liu, X.J.; Lu, Z.P. Atomic structural evolution during glass formation of a Cu–Zr binary metallic glass. *Comp. Mater. Sci.* **2014**, *85*, 147–153. [[CrossRef](#)]
37. Babanov, Y.A.; Schvetsov, V.R.; Sidorenko, A.F. Atomic structure of binary amorphous alloys by combined EXAFS and X-ray scattering. *Phys. B Condens. Mat.* **1995**, *208–209*, 375–376. [[CrossRef](#)]
38. Evertz, S.; Music, D.; Schnabel, V.; Bednarcik, J.; Schneider, J.M. Thermal expansion of Pd-based metallic glasses by ab initio methods and high energy X-ray diffraction. *Sci. Rep.* **2017**, *7*, 15744. [[CrossRef](#)]

Publisher’s Note: MDPI stays neutral with regard to jurisdictional claims in published maps and institutional affiliations.



© 2020 by the authors. Licensee MDPI, Basel, Switzerland. This article is an open access article distributed under the terms and conditions of the Creative Commons Attribution (CC BY) license (<http://creativecommons.org/licenses/by/4.0/>).